

AFRL-ML-WP-TR-2005-4120

**LIFE PREDICTION
METHODOLOGIES FOR AEROSPACE
MATERIALS**



**N.E. Ashbaugh, R.A. Brockman, D.J. Buchanan, G.A. Hartman,
A.L. Hutson, K. Li, and W.J. Porter**

**University of Dayton Research Institute
Structural Integrity Division
300 College Park
Dayton, OH 45469-0128**

JUNE 2004

Final Report for 25 May 1998 – 24 May 2004

Approved for public release; distribution is unlimited.

STINFO FINAL REPORT

The appendix contains a number of articles and conference papers resulting from Department of Air Force contract number F33615-98-C-5214. Copyright is either asserted or may be asserted by the publishers. In all cases, the United States has for itself and others acting on its behalf an unlimited, nonexclusive irrevocable, paid-up royalty-free worldwide license to use, modify, reproduce, release, perform, display or disclose the work by or on behalf of the Government. Any other form of use is subject to copyright restrictions.

**MATERIALS AND MANUFACTURING DIRECTORATE
AIR FORCE RESEARCH LABORATORY
AIR FORCE MATERIEL COMMAND
WRIGHT-PATTERSON AIR FORCE BASE, OH 45433-7750**

NOTICE

Using Government drawings, specifications, or other data included in this document for any purpose other than Government procurement does not in any way obligate the U.S. Government. The fact that the Government formulated or supplied the drawings, specifications, or other data does not license the holder or any other person or corporation; or convey any rights or permission to manufacture, use, or sell any patented invention that may relate to them.

This report was cleared for public release by the Air Force Research Laboratory Wright Site (AFRL/WS) Public Affairs Office (PAO) and is releasable to the National Technical Information Service (NTIS). It will be available to the general public, including foreign nationals.

PAO Case Number: AFRL/WS-04-1431, 13 Dec 2004.

THIS TECHNICAL REPORT IS APPROVED FOR PUBLICATION.

/s/

JAY R. JIRA, Project Engineer
Metals Branch
Metals, Ceramics & NDE Division

/s/

CHARLES H. WARD, Lt Col, USAF
Acting Chief, Metals Branch
Metals, Ceramics & NDE Division

/s/

GERALD J. PETRAK, Asst Chief
Metals, Ceramics & NDE Division
Materials & Manufacturing Directorate

This report is published in the interest of scientific and technical information exchange and its publication does not constitute the Government's approval or disapproval of its ideas or findings.

REPORT DOCUMENTATION PAGE				<i>Form Approved</i> OMB No. 0704-0188	
<p>The public reporting burden for this collection of information is estimated to average 1 hour per response, including the time for reviewing instructions, searching existing data sources, gathering and maintaining the data needed, and completing and reviewing the collection of information. Send comments regarding this burden estimate or any other aspect of this collection of information, including suggestions for reducing this burden, to Department of Defense, Washington Headquarters Services, Directorate for Information Operations and Reports (0704-0188), 1215 Jefferson Davis Highway, Suite 1204, Arlington, VA 22202-4302. Respondents should be aware that notwithstanding any other provision of law, no person shall be subject to any penalty for failing to comply with a collection of information if it does not display a currently valid OMB control number. PLEASE DO NOT RETURN YOUR FORM TO THE ABOVE ADDRESS.</p>					
1. REPORT DATE (DD-MM-YY) June 2004		2. REPORT TYPE Final		3. DATES COVERED (From - To) 05/25/1998 – 05/24/2004	
4. TITLE AND SUBTITLE LIFE PREDICTION METHODOLOGIES FOR AEROSPACE MATERIALS				5a. CONTRACT NUMBER F33615-98-C-5214	
				5b. GRANT NUMBER	
				5c. PROGRAM ELEMENT NUMBER 62102F	
6. AUTHOR(S) N.E. Ashbaugh, R.A. Brockman, D.J. Buchanan, G.A. Hartman, A.L. Hutson, K. Li, and W.J. Porter				5d. PROJECT NUMBER 4347	
				5e. TASK NUMBER 52	
				5f. WORK UNIT NUMBER 01	
7. PERFORMING ORGANIZATION NAME(S) AND ADDRESS(ES) University of Dayton Research Institute Structural Integrity Division 300 College Park Dayton, OH 45469-0128				8. PERFORMING ORGANIZATION REPORT NUMBER	
9. SPONSORING/MONITORING AGENCY NAME(S) AND ADDRESS(ES) Materials and Manufacturing Directorate Air Force Research Laboratory Air Force Materiel Command Wright-Patterson AFB, OH 45433-7750				10. SPONSORING/MONITORING AGENCY ACRONYM(S) AFRL/MLLMN	
				11. SPONSORING/MONITORING AGENCY REPORT NUMBER(S) AFRL-ML-WP-TR-2005-4120	
12. DISTRIBUTION/AVAILABILITY STATEMENT Approved for public release; distribution is unlimited.					
13. SUPPLEMENTARY NOTES Report contains color. The appendix contains a number of articles and conference papers resulting from Department of Air Force contract number F33615-98-C-5214. Copyright is either asserted or may be asserted by the publishers. In all cases, the United States has for itself and others acting on its behalf an unlimited, nonexclusive irrevocable, paid-up royalty-free worldwide license to use, modify, reproduce, release, perform, display or disclose the work by or on behalf of the Government. Any other form of use is subject to copyright restrictions.					
14. ABSTRACT (Maximum 200 words) Superalloys IN-100, René 88DT, Waspaloy, and titanium alloys were investigated. For life-limiting responses in superalloys, highly localized stress-deformation behaviors associated with both typical and unusual defects were developed. Characterizing the relaxation of residual stresses in a component due to temperature, exposure time, and mechanical loading is essential to development of a physics-based life prediction model. Current life management concepts based on damage tolerance have not incorporated the effects of surface and bulk residual stresses to retard crack initiation and crack growth. Finite element models (FEMs) of the feature specimens have been developed and results analyzed. Characterization of fretting fatigue samples revealed that fretting wear and multiaxial fatigue occur simultaneously and that multiple mechanisms contribute to the onset and propagation of cracking. No significant improvement was observed for a soft coating system. Only shear wave ultrasonics was capable of producing a signal from which a crack could be identified. A crystal-plasticity model was developed for γ -titanium aluminide and data from tensile tests of specimens were useful for determining slip strengths and colony and grain boundary influences on material yielding. The results of elevated temperature tensile and creep tests show that off-axis tensile and creep strengths of an oxide/oxide $\pm 45^\circ$ Nextel™720/AS were significantly lower than the strengths in the reinforcing fiber direction.					
15. SUBJECT TERMS Titanium aluminides, ceramic matrix composites, nickel-base superalloys, turbine blade materials, high-cycle fatigue, fatigue crack growth, elevated temperatures, creep, thermal fatigue, thermomechanical fatigue, fretting fatigue, load interactions, mixed-mode, stress intensity factors, finite element analysis, nondestructive evaluation					
16. SECURITY CLASSIFICATION OF:			17. LIMITATION OF ABSTRACT: SAR	18. NUMBER OF PAGES 112	19a. NAME OF RESPONSIBLE PERSON (Monitor) Jay Jira 19b. TELEPHONE NUMBER (Include Area Code) (937) 255-1358
a. REPORT Unclassified	b. ABSTRACT Unclassified	c. THIS PAGE Unclassified			

TABLE OF CONTENTS

SECTION	PAGE
List of Tables	v
Foreword	vi
1.0 EXECUTIVE SUMMARY	1
1.1 COMPONENT DAMAGE ASSESSMENT PREDICTION.....	1
1.2 LIFE PREDICTION WITH RESIDUAL STRESS	1
1.3 PHYSICALLY BASED CONSTITUTIVE MODELING.....	2
1.4 INTEGRATION OF EXPERIMENTAL PROCEDURES AND ANALYSES	3
1.5 HIGH CYCLE FATIGUE (HCF) AND FRETTING.....	3
1.6 γ -TiAl-BASE ALUMINIDES.....	4
1.7 CERAMIC MATRIX COMPOSITES (CMCs)	4
2.0 INTRODUCTION	6
2.1 BACKGROUND	6
2.2 PROGRAM OBJECTIVES.....	6
2.3 REPORT ORGANIZATION	7
3.0 COMPONENT DAMAGE ASSESSMENT PREDICTION	8
3.1 MATERIAL STUDIES OF NICKEL-BASE SUPERALLOYS.....	8
3.1.1 Waspaloy.....	8
3.1.2 René 88DT	8
3.1.3 IN-100.....	9
3.2 CRACK PROPAGATION SIMULATION (GEAE F-404 1st Stage Turbine Disk.....)	10
3.3 CRACK PROPAGATION SIMULATION (F100 Compressor Disk)	11
3.4 NONLINEAR ACOUSTICS.....	11
4.0 LIFE PREDICTION WITH RESIDUAL STRESSES	12
4.1 THERMAL RESIDUAL STRESS RELAXATION	12
4.1.1 Thermal Residual Stress Relaxation in PM IN100 Superalloy [C1].....	12
4.1.2 Residual Stress Relaxation Modeling.....	12
4.2 CRACK INITIATION AND GROWTH IN FEATURE SPECIMENS	13
4.2.1 Characterization of Corner Crack Growth in Subelement Geometries	13
4.2.2 FEA of Corner Crack Growth Analysis under Spectrum Loading Conditions	14
4.3 BULK RESIDUAL STRESSES IN ROTORS	14
4.3.1 Characterization of Residual Stress and Strain Fields in Waspaloy Compressor Disks.....	14
4.3.2 Elasticity (Closed Form) Solution for Bulk Residual Stresses.....	15
4.3.3 FE Solution for Bulk Residual Stresses Using Displacement Boundary Conditions	16
4.3.4 FE Solution for Bulk Residual Stresses Using Imposed Temperature Fields	17
5.0 PHYSICALLY BASED CONSTITUTIVE MODELING	19
5.1 MODELING OF DEFECTS IN Ni-BASED SUPERALLOYS.....	19
5.2 PROBABILISTIC MODELING	19
6.0 INTEGRATION OF EXPERIMENTAL PROCEDURES AND ANALYSES	21
6.1 HYSTERESIS LOOP DATA ACQUISITION CAPABILITY	21
6.2 GENERAL MONOTONIC TESTING CONTROL MODE.....	21
6.3 INFRARED (IR) DAMAGE DETECTION SYSTEM ENHANCEMENTS	21

TABLE OF CONTENTS (concluded)

SECTION	PAGE
6.4 HCF TEST CONTROL MODULE.....	22
7.0 HCF AND FRETTING.....	23
7.1 FRETTING FATIGUE CRACK PROGRESSION STUDY.....	23
7.2 EFFECT OF CONTACT MATERIAL ON FRETTING FATIGUE BEHAVIOR OF Ti-6Al-4V [C2].....	24
7.3 FRETTING FATIGUE DAMAGE CHARACTERIZATION [C3].....	24
7.4 HCFF TECHNICAL SUPPORT	26
7.5 A FRETTING FATIGUE CRACK NUCLEATION DETECTION FEASIBILITY STUDY USING SHEAR WAVE NDI [C4]	26
7.6 CHARACTERIZATION OF FRETTING FATIGUE WITH DIAMOND-LIKE CARBON (DLC) COATING	27
7.7 CHARACTERISTICS AND EFFECTS OF PAD ALLOYS AND Cu-Ni COATING ON FRETTING FATIGUE BEHAVIOR OF Ti-6Al-4V	28
8.0 DAMAGE TOLERANCE STUDIES OF γ-TiAl-BASED Ti ALUMINIDES	29
8.1 MODELING EFFORTS OF STRESS STATES LEADING TO CRACK INITIATION	29
8.1.1 Elastic-Plastic Models of Lamellar Grain Structures.....	29
8.1.2 Experimental and Analytical Evaluation of Room Temperature Tensile Behavior of a Gamma Ti Aluminide Alloy	30
8.2 MICROSPECIMEN TESTING	30
9.0 DAMAGE ACCUMULATION AND FAILURE OF CMCs.....	32
9.1 CHARACTERIZATION OF OXIDE/OXIDE, SiC/SiC AND C/SiC CMC	32
9.1.1 Creep Rupture Behavior of $\pm 45^\circ$ Oxide/Oxide Nextel™720/AS Composite [C5]	32
9.1.2 Interrupted Fatigue Testing of MI and CVI C/SiC CMC	32
9.2 HCF OF CVI C/SiC COMPOSITE	33
10.0 ANCILLARY TEST FACILITY ACTIVITIES	34
10.1 MATERIAL BEHAVIOR	34
10.1.1 Tensile and Fatigue Testing of Gamma TiAl	34
10.1.2 Uniaxial and Torsion Fatigue Tests of Turbine Blade Material (Ti-6Al-4V), with Quantified Impact Damage	34
10.1.3 Tensile and Fatigue Testing of Waspaloy Billet Material.....	35
10.1.4 Fatigue Testing of Aluminum 7XXX Material	35
10.2 LABORATORY ENHANCEMENTS	36
10.2.1 Upgrade Of Laboratory Test Automation Hardware and Instrumentation....	36
10.2.2 Improvement in Load Frame Alignment Equipment and Procedures	36
10.2.3 Improvements to the Laboratory Water Cooling System	36
10.3 DATA ARCHIVAL SYSTEM	36
11.0 REFERENCES.....	38
12.0 List of Previous Manuscripts.....	40
Appendix: Compilation of Manuscripts	45
List of Symbols, Abbreviations, and Acronyms	39

List of Tables

TABLE		PAGE
1.	Material Characteristics and Test Conditions	24
2.	Test Conditions	25

FOREWORD

The work described in this report was performed at the Behavior/Life Prediction Section of the Metals Branch in the Metals, Ceramics & Nondestructive Evaluation Division of the Materials & Manufacturing Directorate, Air Force Research Laboratory (AFRL/MLLMN) under Contract No. F33615-98-C-5214, "Life Prediction Methodologies for Aerospace Materials." Mr. Jay Jira of AFRL administered the contract. The Structural Integrity Division, University of Dayton Research Institute (UDRI), Dayton, Ohio conducts the program with Dr. Noel E. Ashbaugh and Mr. Robert J. Andrews acting as the principal investigator and program manager, respectively. This final report describes the progress of the 6-year contractual effort.

In the sixth year of the contract, the investigations were developed and directed by Dr. Robert Brockman, Dr. Geoffrey Frank, Dr. Kezhong Li, Phil Blosser, Dennis Buchanan, George Hartman, Marc Huelsman, Alisha Hutson, W. John Porter III, and Herbert Stumph. Jacqui Hawkins coordinated input and typing the document. This final report primarily covers the work performed during the period of 25 May 1998 to 24 May 2004 and by reference to previous interim reports, the work reported for 24 May 1998 to 24 May 2004. The previous interim reports are as follows:

- AFRL-ML-WP-TR-2004-4283 15 May 2002 to 24 May 2003 (AD number ADA429753)
- AFRL-ML-WP-TR-2004-4026 25 May 2001 to 24 May 2002 (AD number ADA421560)
- AFRL-ML-WP-TR-2001-4153 25 May 2000 to 24 May 2001 (AD number ADA413469)
- AFRL-ML-WP-TR-2001-4020 25 May 1999 to 24 May 2000 (AD number ADA391400)
- AFRL-ML-WP-TR-2001-4007 25 May 1998 to 24 May 1999 (AD number ADA388507)

1.0 EXECUTIVE SUMMARY

1.1 COMPONENT DAMAGE ASSESSMENT PREDICTION

Microstructural characterization of common turbine engine alloys was the primary focus of the efforts during this reporting period. All of this work was done in support of the DARPA-sponsored Materials Prognosis program. The metals investigated were the superalloys IN-100, René 88DT, and Waspaloy and a single titanium (Ti) alloy, Ti-6-2-4-6. The sources of the material were either retired turbine disks (IN-100, René 88DT, Waspaloy) or forgings with reportedly the same processing history as the components made from the same alloys (IN-100, Waspaloy, Ti-6-2-4-6). The overriding goal of this program was to aid in the formation of microstructurally based life prediction models by identifying and quantifying the characteristics of each microstructure as input to the modeling. The microstructures and their various features serve as the frame for mesh of the models while the material properties define the response of the model to various loading and environmental inputs.

Tools used in the microstructural characterization efforts included optical microscopy, scanning electron microscopy (SEM), and orientation imaging microscopy. Additionally, the use of transmission electron microscopy (TEM) commenced to allow for the quantification of such features as tertiary gamma prime size and distribution, and dislocation development during service.

Finally, development of a nondestructive evaluation (NDE) technique based on nonlinear acoustics and the associated beta parameter continued. This test program involved testing fatigue specimens to a prescribed percentage of their predicted life and then monitoring for changes in nonlinear acoustic response. Trends indicating differences in the beta parameter as a function of accumulated cycles have been observed, and efforts to understand the causes for these changes and in enhancing the data collection process continue.

1.2 LIFE PREDICTION WITH RESIDUAL STRESS

A life prediction methodology that incorporates residual stresses is critical to safely extending the useful life of shot peened components such as turbine engine disks. Current life management concepts based on damage tolerance do not incorporate the beneficial effects of compressive surface residual stresses to retard crack initiation and crack growth. Characterizing the relaxation of residual stresses due to temperature, exposure time, and mechanical loading is essential to development of a physics-based life prediction model. Shot peening is the standard surface enhancement process used to impart a thin surface layer of compressive residual stresses in turbine disks at fracture critical locations. Shot peening typically imparts a compressive residual stress to a depth of approximately 100 to 150 μm . Therefore, fatigue crack initiation and short fatigue crack growth behavior will be strongly influenced by the presence of these compressive residual stresses. Hence, characterizing and modeling the stress relaxation or retention of shot peened induced residual stresses is a critical element of any life prediction methodology.

Characterizing crack growth behavior of corner cracks in subelement geometries under engine operating spectrums will provide data to support the extension of life-limiting components and provide benchmarks to quantify the capability of life prediction models. Subelement geometries, i.e., feature specimens, have been extracted from retired engine components and tested under engine operating conditions. Crack growth behavior from corner cracks have been characterized for two feature geometries. Finite element models (FEMs) of the feature specimens have been developed and results analyzed. Finite element (FE) predictions of corner crack growth behavior match favorably with the experimental crack growth measurements.

Bulk residual stresses are also present in turbine engine disks. Bulk residual stresses often have tensile and compressive residual stresses of approximately equal magnitude in contrast to shot peened residual

stresses that have large compressive and small tensile residual stresses. Bulk stresses develop from nonuniform cooling rates during oil quenching of the disk after a solution heat treatment cycle. These bulk stresses can be a large fraction of the material yield strength. Determination of bulk residual stresses and strains was achieved with measured angular displacements of split disks and a number of analytical models to describe the deformation. The angular displacements imposed boundary conditions for the elasticity (closed form) and FEMs. The predicted bulk strains from the models were in excellent agreement with measured strain gage and moiré data.

1.3 PHYSICALLY BASED CONSTITUTIVE MODELING

A common thread in much of the analytical work performed under this program is the development and application of physically based models of material behavior. Our models of intermetallics have been aimed primarily at understanding the monotonic loading behavior of such materials, although the ultimate goal is to understand and predict life under fatigue loading. In support of ERLE and the DARPA prognosis programs, several areas of investigation are relevant. For superalloys, the life-limiting responses seem to be tied to defects, including voids, void stringers, and inclusions. Therefore, in addition to monotonic and cyclic plasticity models, we are investigating highly localized stress-deformation behaviors associated with both typical and unusual defects. Even under simple loading conditions, the stress distribution surrounding a void or nonmetallic inclusion is complex and includes areas of extreme stress concentration. The key idea is that real material samples (including test specimens) subjected to fatigue loading actually experience broadly variable stress conditions that not only cause very early crack initiation, but also are directly responsible for the significant scatter in fatigue behavior. If we can understand and quantify the conditions responsible for this behavior, we can significantly improve the precision of our fatigue data and fatigue life predictions. In the long term, we hope to integrate our understanding and quantitative representation of this microstructural variability into the constitutive models that we use for design and for forensic investigation.

1.4 INTEGRATION OF EXPERIMENTAL PROCEDURES AND ANALYSIS

The UDRI contribution to the integration of experiments and analysis during this reporting period was focused on enhancements to laboratory test automation software and hardware. Several tasks directed at adding capability to the WinMATE test automation code have been initiated and are either complete or in progress. These enhancements are directed at near-term needs in the AFRL/MLLMN laboratory.

1.5 HIGH CYCLE FATIGUE (HCF) INVESTIGATIONS

Investigation of the fretting fatigue phenomenon as it applies to turbine engine applications has continued to be the focus of the HCF work performed during the past year. As with past work, Ti alloys have been the subject material, and the goal has been to improve damage-tolerant design and reduce the maintenance costs of military aircraft. Considerable effort has been expended in cooperative efforts with researchers outside of MLLMN in the investigation of nondestructive inspection (NDI) techniques for fretting fatigue, and in the evaluation of fretting fatigue amelioration methods related to dissimilar contact materials and coatings.

Efforts to evaluate precrack fretting fatigue damage have resulted in a better qualitative understanding of how fretting fatigue damage begins and propagates. Characterization of fretting fatigue samples from different test systems revealed that fretting wear and multiaxial fatigue occur simultaneously to produce observed fretting fatigue damage, and that multiple mechanisms contribute to the onset and propagation of cracking, which has been identified as the primary damage metric in prior work. These characterization results also provided evidence to support earlier FE stress analyses that have been used in

evaluating a fracture mechanics approach for determining propagation or nonpropagation of fretting fatigue nucleated cracks.

Extension of the fracture mechanics study provides additional confirmation that this approach is better than a stress analysis approach due to the poor understanding of crack initiation criteria in a gradient stress field. The coefficient of friction, μ , has previously been shown to have a profound influence on the calculated stress field used in the K-analysis, and is different for different material pairs. However, fretting fatigue strength was determined to be insensitive to contact material composition, except under limited contact stress conditions. This trend was observed in data obtained from different test fixtures using different contact geometries. Other common trends between different fretting fatigue geometries included observed levels of wear as a function of applied contact stress, measured values of μ for Ti-on-Ti, Ni-on-Ti and Al-on-Ti contacts and modes of material transfer, which were from the softer to the harder metal until wear induced oxidation produced abrasive particles at the component interface.

Fretting fatigue behavior of Ti specimens in the presence of various coating systems is currently under investigation. No significant improvement in fretting fatigue behavior was observed for a soft coating system, such as those currently used to minimize fretting in blade attachments, although μ values and local peak stresses would be expected to change beneficially. Results to date on an experimental hard coating system are inconclusive, but suggest a potential benefit for fretting fatigue, due to dramatically lower μ values. These observations of coating behavior were made for fretting fatigue exclusively under partial slip conditions.

Several NDI methods were evaluated for use in detecting fretting fatigue damage, primarily in the form of cracks: shear wave ultrasonics, residual stress measurement via surface x-ray diffraction, thermography and visual evaluation via SEM. Most common NDI methods cannot distinguish between surface wear and true fretting fatigue crack damage. Thermography and SEM were similarly limited due to the presence of wear debris covering or interfering with the fretting fatigue nucleated cracks. X-ray diffraction (XRD) did not provide sufficient spatial resolution. Only shear wave ultrasonics were capable of producing a signal from which a crack could be identified.

1.6 DAMAGE TOLERANCE STUDIES OF γ -TiAl-BASE TI ALUMINIDES

Work continued on efforts to provide accurate material behavior parameters to aid in the development and refinement of a crystal plasticity model for predicting behavior in γ -TiAl alloys. Experimental information was collected from specimens with geometries representing two distinct size scales. Tensile tests of specimens with colony sizes ranging from 1 to 10 mm were performed in concert with an optically based deformation mapping technique and represent, in this case, a macroscale experimental approach. From the microscale perspective, specimens with diameters ranging from 20 to 100 microns, machined using focused ion beam (FIB) techniques from well within the confines of a single colony, were compression tested using nanoindentation equipment. Load-displacement-time data were collected during the microspecimen testing. Data from both experimental approaches were useful for determining slip strengths and colony and grain boundary influences on material yielding. This information was used to calibrate the crystal-plasticity model that is the focal point of this task.

1.7 CMCs

Damage-tolerant CMCs that exhibit relatively little degradation in mechanical properties under long-term elevated temperature conditions are being evaluated for high-temperature aerospace applications. Many engine components that are axisymmetric in shape and subjected to axisymmetric thermal and mechanical loadings are candidates. In addition, these complex components have fillets, corners, holes and other structural features that develop multiaxial stress states under thermal and mechanical loading. Elevated

temperature tensile and creep tests were performed on oxide/oxide $\pm 45^\circ$ Nextel™720/AS to characterize the off-axis material behavior. The results of the study show that off-axis tensile and creep strengths are significantly lower than the strengths in the reinforcing fiber direction. A NASA program to develop a nondestructive assessment method for damage in CMC was supported by completing several interrupted fatigue tests on melt infiltration (MI) and chemical vapor infiltration (CVI) C/SiC CMC. The fatigue tests were interrupted at different fractions of total life to measure the state of damage in the CMC. HCF tests at room and elevated temperature were also performed on CVI and MI SiC/SiC CMC in support of the NASA program. In addition, continuous improvements have been made to software and hardware for data acquisition and control of mechanical testing.

Several of the experimental programs have provided mechanical behavior data to support analytic modeling efforts on oxide/oxide CMC. A creep and damage accumulation model has been developed that accounts for the anisotropy of the creep response in off-axis orientations. This model improves the prediction of stresses and deformations at holes and notches that are essential for advancements in design of components subjected to multiaxial thermal and mechanical loading conditions.

2.0 INTRODUCTION

2.1 BACKGROUND

The U.S. Air Force (USAF) has various programs in place directed toward the advancement of new gas turbine engines and aerospace vehicle technology and the support of current gas turbine engines. These programs include Integrated High-Performance Turbine Engine Technology (IHPTET), National Turbine Engine Durability (NTED), and Engine Rotor Life Extension (ERLE). The primary goals are 1) extend safely the life of current/legacy rotors, 2) improve performance, i.e., maintain properties at higher service temperatures, and 3) reduction in weight, i.e., use of lightweight materials with high-temperature capability. The need to extend and assess the life of a wide range of current aerospace components has resulted in programs such as ERLE, HCF initiative, Aging Aircraft, Propulsion Life, and DARPA Prognosis. These programs are directed toward conventional materials, such as Ni-base superalloys, Ti alloys (near α and $\alpha+\beta$), and aluminum alloys. To apply the advanced materials effectively or to consider further applications of conventional materials that have experienced service conditions, a thorough understanding of the material behavior must be obtained and a methodology of life prediction for these materials must be developed or refined. Advanced materials such as gamma Ti aluminide (γ -TiAl) alloys, high-temperature intermetallics, and CMC are leading candidates to satisfy these needs for various engine components.

2.2 PROGRAM OBJECTIVES

The primary objectives of this program are to

- 1) evaluate the performance of advanced and conventional materials under simulated service conditions
- 2) develop and/or adapt experimental techniques for characterization of deformation, damage evolution, and failure of advanced and conventional materials under typical service conditions
- 3) develop an understanding of the mechanisms leading to deformation, damage accumulation, and failure of advanced and conventional materials under a variety of test conditions, including simulated mission cycles
- 4) develop physically based deformation and life prediction models necessary to ensure in-service reliability and maintainability of advanced and conventional materials subjected to aerospace usage loading conditions
- 5) transition the new technology to USAF suppliers and customers
- 6) use and update the data for various aerospace materials in the current archival system and enhance the materials data archival procedure.

2.3 REPORT ORGANIZATION

This final report presents the research conducted on the material behavior and modeling of aerospace materials within MLLMN at Wright-Patterson Air Force Base (WPAFB), OH. This effort was conducted over the period from 25 May 1998 to 24 May 2004. The investigations that have been performed during the sixth and final year of the contract will be discussed in this report. Discussions of investigations of previous years can be found in the following interim annual reports: [Ashbaugh et al.; 2000, 2001(2), 200x, and 200x].

The investigations for component damage assessment prediction, life prediction with residual stresses, physically based constitutive modeling, integration of experimental procedures and analysis, HCF and fretting, damage tolerance studies of γ -TiAl-based Ti aluminides, and damage accumulation and failure of CMCs are discussed in Sections 3, 4, 5, 6, 7, 8, and 9, respectively. The first four investigations are

associated with ERLE and DARPA Prognosis Programs. Ancillary laboratory activities are presented in Section 10. Extended discussions of the work in progress are presented to provide as much information as possible about the current investigations. Copies of the manuscripts, which have been written on the completed efforts, are provided in an appendix, Compilation of Manuscripts, for the convenience of readers who wish to have more detailed information of the investigations readily available.

3.0 Component Damage Assessment Prediction

3.1 MATERIAL STUDIES OF NICKEL-BASE SUPERALLOYS

3.1.1 Waspaloy

Waspaloy continued as a material of interest for much of this reporting period. Particular attention was paid to understanding the influence of microstructure and crystallographic texture on fatigue crack propagation. Prior microstructural investigations of the Waspaloy compressor disks of reportedly the same pedigree determined that two of the three disks contained a fine, equiaxed microstructure throughout the component. A third disk, however, was shown to have large regions with a distinctly duplex grain structure. The duplex areas generally contained 3- to 5-micron equiaxed grains surrounded by large grains on the order of 50 to 80 microns with aspect ratios of roughly 2-4:1. Orientation imaging microscopy (OIM) of material from each of these disks revealed a random crystallographic texture in the fine-grained material while the 50- to 80-micron grains in the duplex structure retained a distinct texture with respect to the forging direction, indicative of an absence of recrystallization during the forging and subsequent heat treatment processes.

While fatigue crack growth tests of specimens from various locations in all three disks revealed only minor differences and no significant trends under similar testing conditions, fractography of the same specimens revealed clues to understanding some of the subtle difference in fatigue crack growth rates due to microstructure. In specimens with the duplex microstructure, the large grains retained from forging tended to promote a transgranular fracture mode while the equiaxed material promoted a strongly intergranular crack growth mode. Accordingly, as the crack passes through the duplex material, crack advance is retarded when the large grains are encountered, resulting in a slight lowering of the overall fatigue crack growth rate. In the equiaxed regions of each microstructure investigated, fractography also revealed that as the grain boundary carbides, common in Waspaloy, were stressed during elevated temperature testing they tend to promote intergranular crack formation.

3.1.2 René 88DT

The focus of our efforts on René 88DT dealt with quantification of grain and gamma prime sizes as well as new efforts to determine local crystallographic texture and gamma prime distribution. The application of using OIM to determine both grain size and crystallographic texture was aggressively pursued. Additionally, the use of the Struers Electro-Pol spot polisher allowed for shorter specimen times and often improved electropolished surfaces for OIM analysis. Specimens were investigated from rim, web, and bore locations and were found to be devoid of any strong crystallographic texture. This finding was not surprising due to the powder metal (PM) processing history of this material. The grain size information collected via OIM coincided with our optically determined findings, that is, an average grain size of approximately 20 microns with subtle coarsening from the rim to the bore. TEM samples to determine secondary and tertiary gamma prime sizes and distribution were recently received and analysis is forthcoming.

3.1.3 IN-100

Investigation of the microstructures of sub-solvus and super-solvus heat-treated IN-100 continued over the last year. The super-solvus microstructure is found in compressor and turbine disks, while the sub-solvus microstructure is found primarily in disks of the lower temperature compressor sections. Both microstructure types were investigated through the use of OIM to aid in grain size determination and crystallographic texture.

The sub-solvus microstructure, noted for its inherent high strength and moderate fracture toughness, is composed of primary gamma prime particles in a matrix of gamma grains. Both the primary gamma prime particles and the gamma grains are approximately 5 microns in diameter. The gamma grains are

interspersed with fine gamma prime particles. No strong crystallographic texture was noted in the sub-solvus material and the microstructure was found to be uniform throughout the disk cross section.

The super-solvus microstructure is composed of gamma grains with an average grain size of approximately 20 microns. The super-solvus is noted for its moderate strength and superior creep and fracture toughness compared to the sub-solvus material. As in the sub-solvus material, OIM revealed no strong crystallographic texture regardless of location inspected. Plans are underway to interrogate the finer features of the IN-100 microstructures using TEM.

Additional work on the IN-100 super-solvus microstructure included FIB sectioning and subsequent OIM of an initiation site from a specimen tested under low cycle fatigue (LCF) conditions. The goal of this work was to determine how the local microstructure contributed to fatigue crack initiation. At the time of this writing, the results of this investigation were inconclusive.

The crystallographic plane of IN100 at the initiation region of fracture surfaces under LCF conditions at room and elevated temperature was identified. At room temperature, fatigue cracks initiated on the {111} plane and at elevated temperature on the {001} plane. The initiation plane index was initially determined by investigating the γ' shape in the γ matrix of fracture surfaces around crack initiation sites and finally verified by OIM. An OIM scan on a sample of original material indicated that local texture might promote a fatigue crack to reach a critical crack size.

3.2 CRACK PROPAGATION SIMULATION (GEAE F-404 1st Stage Turbine Disk)

UDRI has performed crack propagation simulations of the General Electric Aircraft Engines' GEAE F-404 René 88DT first-stage turbine disk, under rotational and temperature conditions corresponding to the recent spin pit testing performed at Pax River. Additional static analyses have been performed to investigate the feasibility of detecting and monitoring crack growth using data collected from blade-tip displacement sensors.

Geometric data for the GEAE turbine disk was unavailable, so a solid geometry computer-aided design (CAD) model of the disk was created using CATIA, starting from printed copies of the part drawings. A FEM of a 5.625-degree symmetric sector of the disk was analyzed using an elastic-plastic material model for René 88DT. The disk rotation was cycled from 1,500 to 18,000 RPM at a temperature of 1,100 °F to account for the effects of plasticity. An ABAQUS submodel, driven by the results of the sector model, was used to model a semi-elliptical crack in the bore. Residual stresses, found from the elastic-plastic solution, were applied using an ABAQUS user-defined DLOAD subroutine. The crack growth simulation was performed using Zencrack 7.0. A crack having an initial depth of 0.048 inch and length of 0.1 inch was grown to a depth of 0.249 inch and a length of 0.535 inch in 1,263 cycles.

ABAQUS substructures were built to predict the effects of cracks on blade tip displacement patterns. Three different 5.625-degree substructure elements were created. One substructure had no crack, one substructure had a simulated bore crack, and one substructure had a simulated slot bottom crack. The substructures were assembled to form a complete disk for three analysis cases: an uncracked disk, a single bore crack, and a single slot bottom crack. The crack in the slot bottom had an area of 0.021 in² and the bore crack area was 0.395 in². Radial displacement amplitudes of 0.098 inch were found in the uncracked disk. Displacement variations in the cracked disks were on the order of 0.1 percent of the steady-state displacement. The observed variations in the tip displacement patterns due to the cracks correlated extremely well with the results of spin pit testing.

The model predictions were supplied to Hood Technology Corporation, who were conducting the Pax River spin pit tests on this disk. Signatures predicted from the FE analyses were programmed into the data collection system, so that measured patterns resembling the predicted crack signatures could be monitored during testing. Measured displacement patterns closely resembling predicted signatures from

finite element analysis (FEA) grew steadily during the remainder of the test, and increased dramatically in amplitude several major loading cycles prior to failure of the disk. The observed patterns were distinctive enough to cause Hood Technology to consider ending the test; however, the decision was made to continue the test, and catastrophic failure occurred several cycles later.

3.3 CRACK PROPAGATION SIMULATION (F-100 Compressor Disk)

A solid geometry CAD model of the Pratt & Whitney F-100 12th stage compressor disk was generated in SolidWorks. A FEM of a 15-degree sector of the disk was analyzed with properties for Waspaloy at 1200 °F. The disk rotation was varied from 6,500 to 13,000 RPM ($R = 0.25$). An ABAQUS submodel, driven by the results of the sector model, was used to analyze a crack in the snap ring flange near the antirotation tang. The crack growth simulation was performed using Zencrack. An initial crack size of 0.015 inch was grown to 0.07 inch on the inboard side of the snap ring flange in 306 cycles. The crack grew from 0.98 to 1.01 inch on the outboard side of the snap ring flange. The performance of Zencrack 7.0 on this problem was very disappointing, since we would invariably run into convergence difficulties after a small amount of crack propagation regardless of the choice of tolerances. Recently we have experienced better success with Zencrack 7.1, in which new tolerancing and crack growth control logic are included.

3.4 NONLINEAR ACOUSTICS

The goal of this investigation [Burke et al.] is to evaluate the efficacy of the beta parameter that is associated with the nonlinear acoustic behavior of a metal. When a wave pulse of a baseline frequency is introduced in a metal, harmonic frequencies can be detected with increasing amplitudes associated with fatigue damage accumulation.

Several studies of nonlinear acoustic properties in metallic materials in recent years have shown promise as a new NDE technique for early detection of fatigue damage. For many materials, this early damage before identifiable crack initiation or during the formation of microcracks is a significant portion of fatigue life of a component. Thus, quantification of this precursor damage becomes an important factor in knowing the health of the material and in damage prognosis.

The beta parameter is proportional to the amplitude generated for the second harmonic frequency. A group of specimens of a nickel-base superalloy were fatigued at 650 °C to various fractions of fatigue life of the material. Also, a specimen was exposed at test temperature for the duration of fatigue life with no fatigue cycles applied to it. The results of the beta parameter evaluation for early detection of fatigue damage in these specimens will be discussed in the presentation.

4.0 LIFE PREDICTION WITH RESIDUAL STRESSES

4.1 THERMAL RESIDUAL STRESS RELAXATION

4.1.1 Thermal Residual Stress Relaxation in Powder Metal IN100 Superalloy [C1]

Relaxation of shot peen induced compressive residual stresses due to thermal exposure was measured using XRD. The material was a hot isostatically pressed (HIP) PM IN100 nickel base superalloy. A total of 14 test samples were shot peened to an Almen intensity of 6A using MI-170-R shot with 125 percent coverage. The sample dimensions were nominally 16- by 13- by 4-mm thick with an irradiated x-ray region of 8 by 5 mm. Residual stress measurements were made at the surface and at nominal depths of 12, 25, 50, 75, 125, 175, 250, and 350 microns. The shot peen samples were thermally exposed to two temperatures (650 and 704 °C) and a range of exposure times (0.5 to 300 hours). Residual stress measurements on shot peen samples with no thermal exposure were used as a basis for comparison. The relaxation of shot peen compressive residual stresses under purely thermal loading was examined. Results from this study show that shot peen compressive residual stresses change significantly with thermal exposure. The residual stresses exhibited an initial rapid decrease on the surface and in the depth at all temperatures. However, continued thermal exposure produced little or no change in surface residual stresses while peak compressive stresses in the depth continued to relax with time at both temperatures.

4.1.2 Residual Stress Relaxation Modeling

Analytical studies have continued to determine the nature of residual stress relaxation in PM IN100 under thermal exposure. The analytical studies have been performed using models representing rectangular parallelepipeds, with the models extending several millimeters into the depth to the region in which the residual stresses associated with surface enhancement processes are negligible. For early analyses, XRD measurements made by Lambda Research, Inc. on baseline specimens not subjected to high temperature after shot peening have been used to supply the initial conditions for the analytical models. The lambda measurements include both surface stresses and residual stress profiles into the depth. The direct stress components are initialized to the stress distributions obtained from the corrected XRD measurements; plastic strains are initialized to values obtained from the cold work values measured experimentally. The initial conditions are introduced into the model via ABAQUS user subroutines SIGINI and HARDINI, respectively.

Analyses have been performed to evaluate creep deformation as a function of exposure time. The analytical model is subjected to the temperature condition corresponding to the specific specimen being modeled, using the temperature-dependent stress-strain characteristics of the PM IN100 alloy. Various creep models have been investigated and additional experiments have been conducted to determine the creep characteristics of PM IN100 as a function of stress level and prior prestrain. Results from creep deformation analyses using stress and plastic strain values from the baseline measurements made by lambda suggest that a significant change in the stresses occurs at low exposure times (on the order of 30 minutes or less) which cannot be accounted for by creep deformation. Investigations are continuing to determine the phenomenon by which the baseline stresses undergo significant relaxation at these low exposure times. Subsequent analyses have been performed with initial conditions defined using stresses and plastic strains from lambda for specimens after 30 minutes of exposure. Typical strain-hardening and time-hardening power law creep models appear to accurately capture the subsequent relaxation at increasing exposure times.

4.2 CRACK INITIATION AND GROWTH IN FEATURE SPECIMENS

4.2.1 Characterization of Corner Crack Growth in Subelement Geometries

Several specimen geometries for corner crack growth analysis have been designed and machined from forgings and retired turbine engine disks for fatigue crack growth (FCG) testing. All geometries were designed to investigate corner crack growth from features in turbine engine disks at elevated temperature. FCG feature specimens were extracted from wrought Waspaloy and PM René 88DT turbine disks. Emphasis was placed on collecting corner crack growth data for small cracks, near the NDE detection limit of approximately 100 μm . Electric discharge machining (EDM) starter notches were machined into features to initiate crack growth at a specific location.

A thick double edge notch tension (DEN(T)) FCG geometry was designed with the gage section of the specimen (slug) to be machined from a thick portion of the René 88DT turbine disk. The slugs were inertia welded to IN718 bar stock and machined to the final dimensions. The DEN(T) geometry provided the capability to study corner crack growth behavior in René 88DT at a simulated feature from the disk at 593 °C under simulated engine loading conditions. A second corner crack geometry, similar to the SAE keyhole geometry, was designed around a bolt hole of a Waspaloy compressor disk. The design of the specimen allowed use of existing pin loaded fixtures such as those used for the compact tension geometry. The bolt hole was shot peened by the OEM to retard crack initiation and growth. Therefore this specimen provided the unique opportunity to investigate crack growth from actual extracted features with exact surface conditions and surface treatments of the disk. The FCG tests on Waspaloy feature specimens were performed at 650 °C and under simulated engine loading conditions.

All tests were instrumented with direct current potential difference (DCPD) hardware to continuously measure crack growth. Optical crack length measurements were also made with a traveling microscope. The optical crack length data was used to correct the continuously recorded DCPD data. Periodically, tests were interrupted to perform acetate replica measurements of crack lengths at room temperature. SEM analysis of specimen fracture surfaces was completed to determine the precrack profile at the interior of the sample and to identify and measure marker blocks.

4.2.2 FEA of Corner Crack Growth Analysis under Spectrum Loading Conditions

FEMs of the feature specimens described in the previous section were developed for fatigue crack growth predictions. The crack growth predictions were accomplished using a program called Zencrack, which was developed by Zentech under an Air Force Small Business Innovative Research (SBIR) contract. The original uncracked FE mesh was modified to replace a large single element with a special crack block that contained a definition of the crack front and a predefined number of elements. The Zencrack program called a FE program, such as ABAQUS, ANSYS or Marc, to solve for the energy release rate around the crack front at each increment in crack length. Zencrack calculated ΔK and increments in crack length along the crack front profile. The Zencrack program also modified the mesh inside the crack block to accommodate the new crack front profile. Crack growth predictions with block loading spectrums and constant amplitude spectrums were completed. Fatigue crack growth predictions for both feature specimens were completed. The predicted crack length versus cycle count from Zencrack matched the experimental crack growth results from the feature tests.

4.3 BULK RESIDUAL STRESSES IN ROTORS

4.3.1 Characterization of Residual Stress and Strain Fields in Waspaloy Compressor Disk

Residual stresses and strains in a 12th stage Waspaloy disk were determined using several complementary analytical and experimental techniques. Past efforts have included experimental techniques such as x-ray diffraction, moiré, strain gages and fiducial marks. Strain gages and fiducial marks have been used routinely. Strain gages provide very precise strain measurements for a given location and orientation. The fiducial marks provide displacement boundary conditions across a radial cut to the annulus to drive the closed form elasticity solution and the FE solution described in Sections 4.3.2 and 4.3.3, respectively. For thin disks where the measured radial displacement across the split varies, in general, proportionally with respect to the radius, the elasticity and the FE predictions show excellent agreement with measured strain gage data. For disks with thick bore sections, the radial displacement is not linear with respect to radial position and hence, the measured and predicted strains were not in agreement.

The elasticity and FE solutions both assume that the split disk is stress and strain free. To check the validity of the stress free assumption a previously split disk was strain gaged with a several of radial and circumferential oriented gages. All gages were placed on a radial line 180° from the line where the disk was originally split. Since this location is the furthest removed in a circumferential sense from the stress-free split boundary, it is expected to show the maximum magnitude of retained residual stresses and strains. The strain-gaged region was sectioned into a number of small pieces to remove all the bulk remaining bulk residual stresses. Strain gage readings were measured continuously during the entire EDM sectioning process. Strains measured during sectioning were comparable to strains measured during the original splitting of the disk.

4.3.2 Elasticity (Closed Form) Solution for Bulk Residual Stresses

The closed-form solution, as previously discussed [Ashbaugh et al., 2003], is based on the complete relaxation to the zero state of the residual stresses when a radial cut is made through the annulus of the disk of uniform thickness. In this solution, the hoop displacement across the cut is proportional to the radial location along the cut. Also, the ends of the cut disk are stress free, i.e., not in contact. When the solution has been extended to a variable thickness disk through the use of concentric rings of appropriate local thickness, the results have been in general agreement with those results obtained from detailed 3-D FEMs.

From our measurements of actual components, a thin disk having a ratio of maximum thickness to annulus width < 0.2 is more likely to produce displacements across the radial cut that are proportional to radial location than a thick disk having a ratio > 0.4 . Two thick disks were cut during this reporting period and the hoop, radial, and out-of-plane displacements were measured across the cut as well as on sections of the disk opposite the cut. The hoop displacements across the cut for these disks were not proportional to radial location. Also, the change in hoop displacements opposite the cut did not conform to deformation associated with the complete relaxation of residual stresses.

The proper use of these measurements when the stresses are not completely relaxed is to first model the expected residual stress pattern in either a half or a whole disk model. Then, simulate a cut in the model and compare the displacements at the locations in the model to those measured in the physical disk at the same locations. Reasonable agreement between the measured displacements and the model displacements would indicate that the stresses state in the uncut model represents the bulk residual stresses in the physical disk.

4.3.3 FE Solution for Bulk Residual Stresses Using Displacement Boundary Conditions

UDRI has performed numerous solutions for bulk residual stresses in compressor and turbine disks, using FEMs driven by displacement boundary conditions based on measured displacements. The displacement measurements have been obtained by high-precision measurements of the motions of fiducial marks along the radius of a disk when the disk is cut along a radial line. In general, the motions of the fiducial marks have been used to estimate the circumferential displacements at discrete points on the radius, which then can be curve-fit and applied (negated) as prescribed values in the FE calculation. Radial and axial displacements are not prescribed, since the data and resulting curve fits are not sufficient to allow accurate prescription of these components. In some of our calculations, we have employed sector models, which take advantage of the periodic symmetry of the disk geometry; in others, we have employed half-models of the disk. The resulting stress solution furnishes the stresses (and surface tractions on the cut surface) that have been relieved when the disk is cut. The half-disk models provide localized stress information that should be more precise than the sector models, since the deformation caused by cutting is not assumed to be identical in each sector of the disk.

Cut-disk models of two versions of the Pratt & Whitney F-100 12th stage compressor disk have been analyzed using this technique. For this particular disk, the results from a sector model of the disk exhibited quite good agreement with both closed-form elasticity solutions, and experimental results from strain gage and moiré fringe measurements. In our models of this disk, the curve fits used for the circumferential displacements are linear in the radial coordinate, and for the most part pass through zero; that is, a constant angular displacement is assumed. The experimental data support the results of the sector model, in the sense that additional displacements and stains measured as additional cuts are made in the disk are relatively small. The analytical solutions done using a more sophisticated representation of the residual stress field (see Section 4.3.4) do reveal additional residual stresses associated with localized features in the geometry.

Cut-disk models driven by measured displacements also have been used to estimate the residual stresses in the P&W AIM subscale disk. In this case, the flange area is so large and stiff that the angular displacement rate is not uniform along the radius of the disk. The prescribed displacement field for the final model consists of two linear segments corresponding to the flange and web areas, joined by a cubic spline to maintain continuous displacement and slope. Interestingly, the use of a linear displacement function (constant angular displacement) along the radius, which might be envisioned as being overconstrained, does not result in an overestimate of the residual stresses. Instead, the linear assumed displacement shape actually imposes hoop strains that are too small in the flange and web regions (i.e., at the inner and outer radii), leading to a significant underestimate of the residual hoop stress. The piecewise circumferential displacement fit resolves this problem.

For the GEAE F-404 turbine disk, both sector and half-disk models have been created and analyzed. The results of these two models are quite different, apparently because of the distinctive pattern of residual stress created by the forging process. The radial variation of the circumferential displacements is distinctly nonlinear, as is the pattern of residual stress in the disk cross section. Results from the half-disk model are believed to provide an accurate picture of the residual stress field in this part. The local residual stresses from the half-disk model correspond extremely closely to residual stresses predicted independently by GEAE using the DEFORM code to perform an axisymmetric forging simulation, followed by ANSYS analysis to predict the residual stresses after finishing of the part. Strain gage measurements performed by GEAE do not agree with either of these predictions, and the cause for the disagreement has not been determined.

4.3.4 FE Solution for Bulk Residual Stresses Using Imposed Temperature Fields

Residual stress estimations for the P&W 12th stage compressor disk have been made based on a technique that uses prescribed temperature distributions as potential functions for the residual stress field. The philosophy behind this model is that the disk residual stresses, like thermal stresses, are caused by mutual constraints that prevent individual material elements from deforming to assume a stress-free condition. Near free surfaces, which are traction-free, the appropriate stress components must vanish; similarly, in the model when new surfaces are introduced by cutting, the corresponding residual stresses will conform to the natural boundary condition of zero traction. This technique has the advantage of accommodating any amount and combination of experimental data to drive the solutions, including displacement and strain measurements and data obtained from multiple or partial cuts.

In cutting the 12th stage compressor disk, measurements have been obtained corresponding to several cut lengths during the initial splitting of the disk, and for subsequent cuts from the same disk. A FEM of the rotor was developed with various boundary conditions representing different lengths of cut. Nominal levels of several residual strain states were imposed on the model, and the resulting equilibrium strain and displacement conditions were computed. A best-fit linear combination of the nominal strain states was identified using optimization techniques, such that the error between the measured and computed strains was minimized for all the various lengths of cut. Finally, the optimized set of residual strains was imposed on a model of the uncut rotor, allowing the residual stress and strain in the uncut rotor to be predicted. This analysis method resulted in excellent agreement between measured and predicted data for several of the strain gage locations. It also results in excellent agreement between the measured and computed opening displacement at the cut location. The predicted strains did not agree well with measured data at a few strain gage locations, an error that is believed to be attributed to bending of the rotor, which was not included in the model.

5.0 PHYSICALLY BASED CONSTITUTIVE MODELING

5.1 MODELING OF DEFECTS IN Ni-BASED SUPERALLOYS

Our recent work in modeling defects in nickel-based superalloys focuses on automated, parametric modeling techniques, and on detailed modeling of nonmetallic inclusions. In both cases, the objectives are twofold: to characterize the worst-case behavior that results in life-limiting conditions; and to develop probabilistic representations of stress conditions in the neighborhood of defects for use in advanced constitutive equations.

For parametric modeling of defects, we have developed scripts using the Python scripting language that can be used to create ABAQUS models using ABAQUS/CAE, for specified defect sizes and spacing. The modeling approach is based upon Boolean operations that cannot be performed in PATRAN. Defects in the model may consist of either voids or inclusions. In the case of inclusions, the Python scripts automatically establish exact continuity between the meshes in the parent material and the inclusion, so that stress hot spots caused by pointwise constraints between mesh segments are eliminated. This approach can be used to model void stringers as well as interactions between neighboring voids or inclusions.

We also have performed detailed modeling of large nonmetallic inclusions (alumina) in René 88DT. The inclusion size is typical of defects observed at AFRL to be instrumental in life-limiting behavior, while occurring infrequently enough in the material volume to be statistically insignificant in the defect size distributions. Because the alumina is stiffer than the superalloy, but lower in strength and brittle, differences the local stress field under tensile and compressive loading are quite different. ABAQUS user material routines have been developed that allow brittle fracture of the alumina in tension, while the compressive behavior is elastic-plastic. The models give detailed information about localized stress amplification at the inclusion boundaries, which ultimately can be integrated into probabilistic material models of the superalloy. These FEMs also have been used to obtain first-order estimates of the residual stress fields in the neighborhood of a large defect, assuming a stress-free temperature below the point where significant creep would contribute to stress relaxation.

5.2 PROBABILISTIC MODELING

The parametric modeling techniques described in the previous section are being used to set up Monte Carlo simulations of stress concentrations in the neighborhood of common defect types. The key challenge in this work is computational, since: a) the computing requirements are quite large; and b) the Monte Carlo simulation must initiate and control many separate ABAQUS jobs that execute in a remote batch environment at the Wright-Patterson MSRC.

Our earlier Monte Carlo analysis, based on analytical solutions for a pair of elliptical voids, provided a means of relating measured defect distributions to probability distributions of stress components, but was limited to a pair of defects, relatively simple loading conditions, and elastic behavior. The recently developed parametric modeling techniques will permit similar analyses that include multiple defects, arbitrary loading (including submodels), and elastic-plastic behavior.

6.0 INTEGRATION OF EXPERIMENTAL PROCEDURES AND ANALYSES

6.1 HYSTERESIS LOOP DATA ACQUISITION CAPABILITY

The WinMATE mechanical automation test software is used extensively in the MLLMN laboratory to control and acquire data from material characterization tests. An enhancement was added to the DCPD FCG module to allow collection of auxiliary data sets in addition to the primary data which includes crack length, applied load, and cycle count information. Each auxiliary data set consists of up to 10,000 data samples acquired at evenly spaced intervals over a period of time from 10 ms to 1,000,000 s. Each data sample consists of a time data stream plus up to 10 data streams taken from the 32 WinMATE analog-to-digital (A/D) channels. The auxiliary data acquisition capability is typically used to collect load and displacement hysteresis loops, although many other uses are possible.

6.2 GENERAL MONOTONIC TESTING (GMT) MODULE CONTROL MODE

The GMT module was originally designed to allow completely automated control of both measured and calculated parameters on a real-time basis. This code was developed and beta tested; however, due to the need for a less sophisticated operator interface and remaining control loop tuning issues, the decision was made to convert the module to a simpler version that will only control operator-preset measured parameters. This conversion is in process and will allow immediate use of the module on the simpler tests envisioned for the near future in the MLLMN laboratories. The original version of the code with the more sophisticated control modes remains available for implementation at a future date.

6.3 INFRARED (IR) DAMAGE DETECTION SYSTEM (IDDS) ENHANCEMENTS

The IDDS module was originally written as a demonstration utility designed to allow the operator to collect and view IR images using a fixed image processing scheme. The module did not include any of the documentation, cross-module safety guards, or other features that are standard on all other WinMATE test control modules. After noting the lack of data traceability and the difficulty in deciphering older data sets with little or no internal documentation, the decision was made to upgrade the IDDS module so that it included a standard test log file containing all of the test documentation as well as a chronological record of the events taking place during the test. This work is approximately 70 percent complete.

6.4 HCF TEST CONTROL MODULE

The next test control module on the WinMATE priority list is the HCF module. Work has begun on this module and the effort is approximately 20 percent complete.

7.0 HCF AND FRETTING

7.1 FRETTING FATIGUE CRACK PROGRESSION STUDY

A study was conducted to quantify fretting fatigue damage and to evaluate the residual fatigue strength of specimens subjected to specific fretting fatigue test conditions, and apply a fracture mechanics methodology to model the crack growth behavior of any fretting fatigue-nucleated cracks included in the damage. Flat Ti-6Al-4V specimens were tested against flat Ti-6Al-4V fretting pads with blending radii at the edges of contact. Fretting fatigue damage was examined for 10 percent of total life for a given static average clamping stress of ~620 MPa and applied axial stress of ~250 MPa, corresponding to a fatigue strength for a 107 cycle fatigue life, identified in earlier work [Hutson, et al.]. These conditions are known to be similar to those found in turbine engine blade root attachments. All samples were inspected using SEM, to identify and measure fretting-fatigue nucleated cracks, and were heat-tinted in air at 420 °C for 4 hours to mark crack front locations. The effect of the fretting fatigue damage on uniaxial fatigue strength was quantified by step-loading the fretting-damaged specimens under uniaxial fatigue loading at R=0.5 and 300 Hz. After specimen fracture, crack aspect ratios were measured via optical fractography. The shape and size of the crack front were then used in calculating threshold stress intensity factors, ΔK_{th} , for each crack. Resulting uniaxial fatigue limit and ΔK_{th} values were compared with the baseline fatigue strength (825 MPa) for this material and the ΔK_{th} value (2.9 MPa \sqrt{m}) for naturally initiated cracks tested at R=0.5.

As an extension of prior efforts to quantify the adverse effect of fretting fatigue, additional specimens were produced under the conditions discussed above, to expand the database on which the following conclusions are based. Resulting cracks, ranging in size from 30 to 800 μm were detected. Fretting fatigue cracks with surface length, $2c$, of 100 μm or more were required before significant decreases in residual fatigue strength were noted. Aspect ratios measured for cracks that propagated to fracture during uniaxial fatigue cycling were very near unity for crack surface lengths below 150 μm , but decreased with increasing crack surface length. Threshold stress intensity factors computed for these cracks indicated threshold behavior consistent with naturally initiated cracks that were stress relieved to remove load history effects.

Propagation lives for each cracked sample are being calculated assuming mode I propagation of a surface crack. A prior study indicated a minimal effect of mode mixity on the uniaxial growth of cracks of the size used in this investigation. Resulting lives will be compared with the 9 million-cycle propagation life that would have been expected in the experiments, if the contact conditions had not been removed. In the previous investigation, coefficients of friction, μ , of 0.3 and 1.0 were considered. For this study, simulations will be performed for μ values of 0.5 and 0.7, and the trends will be compared. Results will be documented at the 5th International Conference on Fatigue Damage of Structural Materials.

7.2 EFFECT OF CONTACT MATERIAL ON FRETTING FATIGUE BEHAVIOR OF Ti-6Al-4V [C2]

A cooperative study with the Air Force Institute of Technology (AFIT) was conducted to explore the fretting fatigue behavior of Ti-6Al-4V specimens in contact with pads of varying surface composition. Three conditions were selected to provide a range of compositions and hardnesses: Ti-6Al-4V (low-stress ground and polished to RMS 8), two comparable aluminum alloys and two comparable nickel alloys. A fourth condition (Ti-6Al-4V, grit blasted to RMS 64 and stress relieved) was selected to interrogate the effect of surface roughness. Behavior against the four pad conditions was evaluated with step testing and S-N fatigue testing using two contact pad geometries (cylinder-on-flat and flat-on-flat with a blending radius) in two independent fretting fatigue fixtures. Laboratory experiments were conducted at different applied stress levels and contact forces. Average applied clamping stresses for the flat-on-flat contact were set at ~200 MPa and ~620 MPa. Applied contact forces for the cylinder-on-flat contact were

selected to provide two Hertzian peak pressures of 292 and 441 MPa. The coefficient of friction, μ , was quantified to help identify possible crack nucleation mechanisms and the contact pad surfaces were characterized through hardness and composition evaluation, and surface profile measurements. FE analyses of the two fretting fixtures were conducted to assess variability in relative slip and local stress state for each pad material.

The same basic trends were observed for both fretting fatigue fixtures. In general, fretting fatigue behavior was insensitive to the pad material employed in the contact. This conclusion was supported by both experimental and analytical results from the two contact types. The nickel-based pads indicated a nominal improvement in fretting fatigue behavior, but only under certain conditions, namely, high applied clamping stress and lower axial fatigue stress. The mechanisms for this improvement were not clear, but some characterization results from prior work suggest that it may be synergistic effect of higher pad roughness coupled with higher clamping stress. Finally, material tended to transfer from the softer material in the pair, until oxidation accelerated by wear produced abrasive particles, such as TiO_2 or Al_2O_3 , that abraded the harder material. No trends in fretting fatigue behavior were evident in association with the wear results.

7.3 FRETTING FATIGUE DAMAGE CHARACTERIZATION [C3]

An investigation was conducted to study the nature of fretting fatigue damage prior to crack nucleation. In the experimental apparatus employed in this study, several locations on each test specimen exist where cracks can nucleate due to local contact conditions; however, not all of the sites bear cracks upon test completion. This study was developed to evaluate the condition of noncracked sites on several fretted specimens in an effort to identify differences between these and sites where small cracks were observed, and to locate sites where crack nucleation was imminent prior to removal of the contact.

A single test condition of 620 MPa average applied static clamping stress and 250 MPa applied axial fatigue stress for $R=0.5$ was selected, based on the quantity of data and test specimens from prior work. Several destructive and nondestructive characterization methods were chosen to facilitate material evaluation: SEM, residual stress measurement, TEM, and thermography. Each site at which crack nucleation could occur was inspected in the SEM and was then characterized using XRD to quantify trends in the residual stresses. Then TEM foils were cut from one area on an as-received specimen with tiny cracks, and dislocation densities were observed. A novel technique was used to prepare the TEM foils. A FIB was used to cut small pieces from specific sites, identified with in situ SEM imaging. These pieces were then placed on a specially designed holder and thinned using the FIB to create sections of suitable thickness. This method permitted TEM samples to be obtained from regions in close proximity on the original specimen, a task that is not possible with conventional TEM preparation.

Comparisons were made between as-received and stress-relief annealed specimens, on which the stress-relief was applied prior to fretting fatigue testing. Comparisons were also made between specimens tested to fracture and specimens tested to 10 percent of an estimated fatigue life. SEM inspection was useful for qualitative analysis of wear debris and identification of cracks as small as 20 μm , but provided no quantitative data on the level of fretting fatigue damage beyond crack size. Trends were noted in the residual stresses for the stress relief annealed specimens, but the changes in residual stress on the as-received specimens were obscured by the initial residual stress produced by the manufacturing process. Also, no stress peaks were noted in the edge of contact regions, probably due to the small scale of the affected regions on the specimen compared to the 1 mm spot size used in obtaining the residual stress measurements. The dislocation structure decayed rapidly into the specimen thickness, but the cause of the dislocations, machining or edge of contact (EOC) stress peaks, could not be determined with only one specimen. Thermography, which can usually identify cracks as small as 25 μm , was unable to identify any cracks on any of the specimens that were inspected with this technique. Although a more rigorous

analysis is required to determine the cause of these results conclusively, the fretting debris in the crack mouth is a likely factor in obscuring the fretting fatigue cracks.

7.4 HIGH CYCLE FRETTING FATIGUE TECHNICAL SUPPORT

UDRI has provided technical support for testing programs being conducted by MLLMN personnel, including uniaxial fatigue experiments performed at ultra-high frequency, ongoing investigations of fretting fatigue under conditions of constant and variable contact loading for various contact geometries employed in three fretting fatigue test systems, and assessment of fretting nucleated crack behavior via bend testing of C-shaped specimens. This support has been provided in the form of recommendations on various hardware requirements and modifications to data acquisition software. For the 20-kHz test system, UDRI has continued the refinement of LabView®-based software during the past year, and has assisted in the experimentation used to verify the loads conveyed to the ultrahigh frequency test specimen for $R=-1$.

7.5 A FRETTING FATIGUE CRACK NUCLEATION DETECTION FEASIBILITY STUDY USING SHEAR WAVE NDI [C4]

A study was conducted to determine the efficacy of using shear wave ultrasonic NDI to locate fretting fatigue nucleated cracks in Ti-6Al-4V in situ. Experiments were performed at 300 Hz under ambient laboratory conditions with flat Ti-6Al-4V pads that had relatively large blending radii at the edges. Two average applied clamping stresses of 200 and 620 MPa were selected, which represent the range of stresses expected for turbine engine blade attachments. Fretting fatigue limit stresses for a 107 cycle fatigue life for each of these clamping stress conditions were 330 MPa and 250 MPa, respectively. These values correspond to 40 and 30 percent of the uniaxial fatigue limit (825 MPa) for this material at $R = 0.5$.

Feasibility of detecting fretting fatigue nucleated cracks in situ using the shear wave NDI was confirmed, and fretting fatigue cracks were identified for the selected stresses. Using the shear wave ultrasonic technique, cracks with a surface length of ~ 2.5 mm were detected on 10 mm wide specimens in tests conducted at higher clamping stress. Prior work indicated that crack nucleation life for this condition was ~ 10 percent of life, and nucleation sites were found to occur within 500 μm of the specimen edge. For the lower clamping stress, crack nucleation required over 95 percent of the total life, and no cracks were identified with the shear wave NDI. Posttest correlation of the data provided signals that were easier to inspect for changes in the waveform by eliminating the reflections produced by coupling with the pad.

A specimen with four EDM notches, each located at an EOC, was tested at the higher clamping stress condition to evaluate the response of the ultrasonic crack detection hardware and to determine the sensitivity of the technique in the presence of components in contact. On one face of the specimen, a 250- μm notch was located on the EOC at the intersection with the specimen centerline and a 500- μm notch was located on the other EOC at the intersection with the specimen centerline. On the opposite face of the specimen, a 500- μm notch was located on each EOC with one notch 500 μm from the edge of the specimen and the other notch 2.5 mm from the edge. These four notches were manufactured and located to obtain a variety of signatures from the ultrasonic responses. First, reflections from the notches without applied clamping loads were recorded. Then, the clamping load was applied, and reflections from the notches were documented. Next, the sample was cycled under the fretting fatigue stress condition described above until shear wave signal changes were noted. Then, the sample was inspected using ultrasonic c-scanning, was heat-tinted, and then fractured in uniaxial fatigue to facilitate inspection of the fretting fatigue crack wake.

Detection of the 500- μm center notch without the contact was dependent of the force used to press the transducer against the specimen, which controlled the thickness of the coupling layer in the bench test. Thickness of the coupling layer combined with the presence of the contact in the fatigue test prevented any of the notches from being detected. The notch closest to the edge propagated rapidly compared to the

other notches, and the resultant crack was detected when it was ~2.5 mm long, similar to the cracks that nucleated in the absence of a notch. Overall, application of the technique to a contact environment was determined to be viable, but many refinements would be required to improve resolution. Autocorrelation performed in situ would further improve crack detectability.

7.6 CHARACTERIZATION OF FRETTING FATIGUE BEHAVIOR WITH DIAMOND-LIKE CARBON (DLC) COATING

A DLC coating has been identified as a possible fretting and fretting fatigue amelioration method. The coating is applied via a plasma spray deposition process that does not require line of sight, and the resulting layer minimizes friction at the contact. Preliminary testing by Boeing [ref] does not indicate any reduction in uniaxial fatigue strength that might be expected with a brittle surface layer. To further evaluate the coating benefits and drawbacks, a testing program has begun to compare the wear and fretting fatigue behavior of specimens with and without the coating. This program involves application of a range of experimental methods to be performed by MLLMN and ML's Tribology group MLBT. MLLMN is conducting uniaxial fatigue experiments to verify the results obtained by Boeing, and is performing fretting fatigue experiments in two different fixtures characterized by different levels of wear.

UDRI is responsible for performing the fretting fatigue tests with the minimum level of wear and has completed some tests that, although inconclusive, seem to support the beneficial aspects of the coating. Additional experiments will be performed in an effort to provide more conclusive results and to compare this coating with other surface treatment systems under consideration, including low pressure, high-intensity plasma nitriding and electroless Ni-B plating.

7.7 CHARACTERISTICS AND EFFECTS OF PAD ALLOYS AND Cu-Ni COATING ON FRETTING FATIGUE BEHAVIOR OF Ti-6Al-4V

An experimental study was conducted to explore fretting fatigue behavior of Ti-6Al-4V in contact with pads of varying surface composition. Four conditions were selected to provide a range of compositions and hardnesses: Ti-6Al-4V, 7075-T6 Al, IN100, and Cu-Ni plasma spray-coated Ti-6Al-4V. Fretting fatigue behavior against each pad type was characterized through evaluation of fretting fatigue strength for 107 cycles. Coefficient of friction, μ , was quantified and pad surfaces were characterized through hardness and composition evaluation, as well as surface profile measurements. Limited difference in fatigue strength was associated with contact material. A modest increase in fretting fatigue strength was observed for specimens tested against coated pads as compared to those tested against Ti-6Al-4V pads; however, roughness of the coated pad was identified as the cause for the increased capability. Another factor was determined to be μ , which was identified as ~0.3 for coated pads, ~0.7 for Ti-6Al-4V, ~0.6 for IN100 and ~0.3 for Al pads. Fretting wear was minimal for all cases, and the coating remained intact throughout the tests. The rougher surfaces tended to get smoother during cycling, while the smoother surfaces, similar to the specimens, tended to stay the same.

8.0 DAMAGE TOLERANCE STUDIES OF γ -TiAl-BASED Ti ALUMINIDES

8.1 MODELING EFFORTS OF STRESS STATES LEADING TO CRACK INITIATION

8.1.1 Elastic-Plastic Models of Lamellar Grain Structures

Work on the definition of the crystal plasticity model for γ -TiAl was completed by identifying appropriate strength, hardening, and rate sensitivity parameters for the 395M material developed at AFRL. The elastic-plastic properties were defined using a similar procedure to that followed in defining orthotropic elastic properties. Ten large-grained dogbone specimens were modeled in detail, with all grain geometry represented explicitly in the FE meshes. Orientations of the lamellar colonies were defined based on OIM measurements, in most cases taken from multiple surfaces in each colony. Strengths for each group of slip geometries (basal, prismatic, pyramidal, gamma-only, and interlamellar) were determined iteratively based on strain gage measurements. Length scale corrections of Hall-Petch type have been introduced in the model, based on both the domain size within lamellar planes and the interlamellar spacing. The mean free path length associated with any slip system is determined by the projection of the slip direction onto these two dimensions, and the resulting length is used in the usual Hall-Petch equation for size dependence of the slip strength.

Three of the large-grained specimens are dual-colony specimens, with two lamellar colonies arranged roughly in series in the gage section of the specimen. In all three cases, the crystal plasticity model predicts the qualitative features of the response very accurately, in that strains in one of the lamellar colonies is typically significantly larger than in the other. The quantitative agreement of the predictions with measured data is good, but not perfect. The chief reason for the discrepancies observed is that the slip strengths exhibit significant statistical variation, based on analysis of the remaining dogbone specimens.

The resulting model also has been used to predict the uniaxial response of several K5 polycrystal specimens tested at AFRL. Because these specimens are polycrystals containing a significant number of grains, several models were analyzed using grain geometries generated from assumed size statistics, with uniformly random orientations. The properties of the K5 material were assumed to be identical to 395M. No data about domain size in either material is available, so predictions were performed for the K5 specimens for several domain sizes between 10 and 100 microns. The assumed domain size for 395M in the original model is 50 microns. The predictions agree well with the measured data for K5 for domain sizes in the range of 40-50 microns.

Experiments were performed to determine the rate sensitivity of γ -TiAl, since previous tests conducted at AFRL were all at quasi-static rates. Additional tests provided yield stresses for strain rates at 0.001/s, 0.1/s, 1/s, and 10/s, and suggest that the rate sensitivity exponent is approximately $m=0.0105$. Yield stresses from the earlier quasi-static tests at AFRL fall directly in line with those from the higher-rate tests for $m=0.0105$.

8.1.2 Experimental and Analytical Evaluation of Room Temperature Tensile Behavior of a Gamma Ti Aluminide Alloy

An experimental and analytical approach to determine the elastic and plastic behavior of large colony, gamma Ti aluminide specimens under tensile loading was pursued. A full-field deformation mapping technique and conventional strain gages were employed to monitor displacement changes during the tensile testing. A 3-D FEM was used to deduce the elastic behavior. An FE-based crystal plasticity model was developed to aid in the prediction of the onset and degree of plastic deformation (see 8.1.1).

Additionally, fractographic analysis of the failed specimens was performed to further our understanding of the mechanisms leading to failure.

8.2 MICROSPECIMEN TESTING

The use of microspecimens and nanoindentation test equipment to acquire material behavior information for use in our modeling efforts continued. Microspecimens, in this case, are columnar posts with diameters in the range of 20 to 100 microns that are tested in compression. The microspecimens were machined from the same large colony K5 material used in the deformation mapping work. Specific locations from which the microspecimens were machined were identified using OIM. OIM allows for the lamellar orientation of the microspecimen to be known before machining commenced. Machining of the specimens was done using two approaches. The first approach involved using FIB processes to accomplish all of the machining. Since the FIB-based approach has very low material removal rates, it can take in excess of 24 hours to produce a single post. As time on the FIB microscope is very limited due to their current popularity, a different method to aid in specimen manufacturing was necessitated. The second approach for producing microspecimens uses micro-EDM technology to do the bulk material removal followed by using FIB for the final surface preparation. The micro EDM is a very cost- and time-efficient approach when compared to FIB machining and allows the FIB time to be cut by at least 67 percent (<8 hours).

Compression tests were performed on a number of specimens and the load, time, and displacement data was analyzed for input into the FE-based crystal plasticity model being developed.

9.0 DAMAGE ACCUMULATION AND FAILURE OF CMCs

9.1 CHARACTERIZATION OF OXIDE/OXIDE, SiC/SiC AND C/SiC CMC

9.1.1 Creep Rupture Behavior of $\pm 45^\circ$ Oxide/Oxide Nextel™720/AS Composite [C5]

Oxide/oxide CMCs are currently being demonstrated in high-temperature aerospace applications where their beneficial resistance to oxidation is critical to a successful design. Many applications are engine components that are axisymmetric in shape and subjected to axisymmetric thermal and mechanical loadings. However, traditional woven CMC materials used in these components are typically made from $0^\circ/90^\circ$ fiber architectures. In many cases, the highest stresses are not always coincident with the orientation of the reinforcing fibers. Therefore, these components may experience stress states that approach off-axis tensile and creep strengths. The oxide/oxide CMC investigated in this study was Nextel™720/AS. Nextel™720/AS is composed of an alumina-silica matrix reinforced with an eight-harness satin weave (8HSW) of Nextel™720 fibers. Tensile and creeps tests at 1100°C on $\pm 45^\circ$ Nextel™720/AS were performed to characterize the off-axis material behavior. The $\pm 45^\circ$ orientation had approximately two thirds the ultimate tensile strength of the $0^\circ/90^\circ$ orientation. However, the tensile toughness of the $\pm 45^\circ$ orientation was higher than the $0^\circ/90^\circ$ orientation by a factor of 2 times. The creep rupture strength at 100 hours for the $\pm 45^\circ$ orientation was approximately one third that of the $0^\circ/90^\circ$ orientation.

9.1.2 Interrupted Fatigue Testing of MI and CVI C/SiC CMC

Experimental support was provided to Dr. Shanker Mall for interrupted fatigue testing of MI C/SiC. These tests supported a program with NASA to develop a nondestructive assessment method for material damage in CMC. There were a total of 36 test specimens in the test matrix. The effect of frequency, stress ratio, maximum stress and temperature were investigated. The test matrix had four interruptions during the life of the specimen for nondestructive measurements by NASA. Three of the four nondestructive measurements have been completed. The first NDE measurements were made prior to any mechanical cycling. The second NDE measurements were performed after cycling at 10 Hz for 10,000 cycles on each specimen. The third NDE measurements were performed after cycling at 10 Hz for 100,000 cycles on each specimen.

9.2 HCF OF CVI C/SiC COMPOSITE

Experimental support was provided for high-frequency (375 Hz) HCF testing of CVI SiC/SiC CMC at room and elevated temperature. Dynamic load calibrations were completed for this study and were shown to be consistent with previous calibrations. Additional support was provided on damage accumulation of CVI C/SiC CMC for 10^6 cycles per specimen for the NASA program described in Section 9.1.2.

10.0 ANCILLARY TEST FACILITY ACTIVITIES

10.1 MATERIAL BEHAVIOR

10.1.1 Tensile and Fatigue Testing of Gamma TiAl

Twenty-nine gamma Ti aluminide specimens of varying chemical and process conditions were tested in support of work being performed in AFRL/MLLMD. Specifics concerning material composition, heat treatment, and testing conditions are provided in Table 1.

Table 1. Material Characteristics and Test Conditions

Material Characteristics			Test Conditions	
Chemical Composition (at %)	Designation	Heat Treatment	Qty/Type Test	Temperature
Ti-46Al-1Cr-3Nb-0.3W-0.5C-0.2Si	02K5B2	48 hours	1 Tensile	Room temp
		800 °C/ 200 hours	2 Tensile	Room temp
Ti-45Al-1Mn-6Nb-0.5W-0.15B-0.6C-0.2Si	02DB1	24 hours	3 Fatigue	Room temp
		48 hours	2 Tensile	Room temp
		48 hours	1 Tensile	704 °C
		48 hours	1 Tensile	815 °C
		800 °C/200 hours	2 Tensile	Room temp
		48 hours	3 Fatigue	Room temp
Ti-45Al-1Mn-6Nb-0.5W-0.15B-0.6C-0.2Si	02DB2	24 hours	2 Tensile	Room temp
		24 hours	1 Tensile	704 °C
		24 hours	1 Tensile	815 °C
		800 °C/200 hours	2 Tensile	Room temp
		48 hours	3 Fatigue	Room temp
Ti-45Al-7Nb-0.2W-0.2Hf-0.2Zr-0.1Y-0.3B-0.3O-0.15C	99GA2	900 °C/24 hours	1 Tensile	Room temp
Ti-45.9Al-1Cr-3Nb-0.3W-0.2B-0.2Y-0.34C-0.25Si	02CA2	800 °C/200 hours	1 Tensile	Room temp
Ti-44.8Al-0.98Mn-6Nb-0.61W-0.22B-0.62C-0.19Si-0.21O	02DA2	800 °C/200 hours	1 Tensile	Room temp
	02DB1	800 °C/200 hours	1 Tensile	Room temp
Ti-45Al-1Cr-6Nb-0.4W-0.2B-0.6C-0.2Si	02GA1	800 °C/200 hours	3 Tensile	Room temp
	02GB1	800 °C/200 hours	1 Tensile	Room temp

10.1.2 Uniaxial and Torsion Fatigue Tests of Turbine Blade Material (Ti-6Al-4V), with Quantified Impact Damage

A series of tests has been conducted to assess the fatigue strength of flat specimens that have been impacted by 3.2-mm-diameter steel spheres at velocities of 200 and 300 m/s. Indents of the same depth as those under ballistic impact were generated quasi-statically by pressing the same size spheres into the material as well as by low velocity pendulum impacts, also using the same spheres. Rectangular specimens with and without (baseline) the three types of indents were tested in tension, and torsion. Bend testing has just been started. Half the specimens were stress relief annealed to remove any residual stresses developed during the indenting process. The other half were tested as indented. This procedure provides a method for sorting out the individual effect of residual stress. Testing was a cooperative effort with AFIT/ENY.

10.1.3 Tensile and Fatigue Testing of Waspaloy Billet Material

Eighteen tensile and two fatigue tests were conducted to support a metal processing study for AFRL/MLLMP. These tests provided baseline data used to establish current testing were elevated temperature fatigue tests are interrupted for replication work to detect location and growth of cracks. Summary of test conditions are provided in Table 2.

Table 2. Test Conditions

Grain Structure Designation	Qty/ Type of Test	Temperature
E	3 Tensile	Room temp
	4 Tensile	650 °C
	2 Tensile	700 °C
	1 Fatigue	650 °C
M	3 Tensile	Room temp
	4 Tensile	650 °C
	2 Tensile	700 °C
	1 Fatigue	650 °C

10.1.4 Fatigue Testing of Newly Developed 7000 Series Aluminum Alloy

Initial work began in support of a program to characterize fatigue life of a new aluminum alloy at room and cryogenic (LN₂) temperatures. Specimen geometry, test fixturing, and an alignment specimen have been designed and currently being manufactured. No actual equipment modification or testing has occurred at time of reporting. This program provides data to AFRL/MLLMD.

10.2 LABORATORY ENHANCEMENTS

10.2.1 Upgrade of Laboratory Test Automation Hardware and Instrumentation

Two additional servohydraulic test systems (SH 4 and SH 31) were updated to windows based WinMATE DCPD software control. One additional portable MATE system was constructed to supplement testing requirements. Preliminary work was performed to determine hardware and software requirements necessary to conduct DCPD crack growth under TMF conditions. Currently, a system is being constructed to demonstrate feasibility of TMF DCPD crack growth using a combination of MATE and WinMATE control systems.

10.2.2 Improvement in Load Frame Alignment Equipment and Procedures

Preliminary documentation concerning procedures for aligning load frames with the different styles of alignment specimens was completed. One additional specimen (button head-cylindrical body) was added to our collection of geometry specific alignment specimens. Two load frames (SH 42 and SH 44) were modified to accept the MTS 609 alignment fixture.

10.2.3 Improvements to the Laboratory Water Cooling System

Improvements started in FY 2003 were completed in November 2003. Work completed during this contract period include removal of the old reservoir tank and pump system and replacing with a smaller flushable reservoir tank, inline system filter and two pumps in series providing approximately 60 gallons per minute (GPM) at 40 pressure per square inch (PSI) system pressure. A low maintenance corrosion inhibitor has been implemented.

10.3 DATA ARCHIVAL SYSTEM

The data archive is a central data server on which test data generated by RG 2.3 is stored and indexed. Its purpose is to prevent the loss of valuable test data and provide independent user access within RG 2.3. UDRI provides continued support for local server administration of file access privileges and works with MLOC on global system administration. In addition, UDRI assisted MLOC with the transfer of all data archive files to updated server hardware, and obtained from them a DVD copy of the data residing on the old server hardware for permanent storage by MLLMN. During this process, we also identified and resolved a problem in which special characters used in filenames (from Macintosh or some Windows-based systems) prevented transfer of those files to other media, CDs and DVDs in particular.

A large volume of test data for coupons was added to the archive to the archive this year, and the documentation provided to the users was maintained. A process was also begun to transfer all test data from the lab machines for archival. Many specimens tested by MLLMN engineers had either not been archived, or had been archived but not removed from the original test system. These data have been moved to the archive server, except for ongoing tests or test series, to prevent loss of data and to minimize duplication of archival efforts. Education of new and existing users is continuing, as needed.

11.0 REFERENCES

Ashbaugh, N.E., et al., Life Prediction Methodologies for Aerospace Materials, Interim Annual Report for Period 25 May 1998 – 24 May 1999, AFRL-ML-WP-TR-2001-4007 (AD number ADA388507), Materials & Manufacturing Directorate, AF Research Laboratory, AF Materiel Command, WPAFB, OH 45433-7750, August 2000.

Ashbaugh, N.E., et al., Life Prediction Methodologies for Aerospace Materials, Interim Annual Report for Period 25 May 1999 – 24 May 2000, AFRL-ML-WP-TR-2001-4020 (AD number ADA391400), Materials & Manufacturing Directorate, AF Research Laboratory, AF Materiel Command, WPAFB, OH 45433-7750, January 2001.

Ashbaugh, N.E., et al., Life Prediction Methodologies for Aerospace Materials, Interim Annual Report for Period 25 May 2000 – 24 May 2001, AFRL-ML-WP-TR-2001-4153 (AD number ADA413469), Materials & Manufacturing Directorate, AF Research Laboratory, AF Materiel Command, WPAFB, OH 45433-7750, June 2001.

Ashbaugh, N.E., et al., Life Prediction Methodologies for Aerospace Materials, Interim Annual Report for Period 25 May 2001 – 24 May 2002, AFRL-ML-WP-TR-2004-4026 (AD number ADA421560), Materials & Manufacturing Directorate, AF Research Laboratory, AF Materiel Command, WPAFB, OH 45433-7750, June 2002.

Ashbaugh, N.E., et al., Life Prediction Methodologies for Aerospace Materials, Interim Annual Report for Period 25 May 2002 – 24 May 2003, AFRL-ML-WP-TR-2004-4283 (AD number ADA429753), Materials & Manufacturing Directorate, AF Research Laboratory, AF Materiel Command, WPAFB, OH 45433-7750, June 2003.

Burke, E., Ashbaugh, N.E., and Sathish, S., Life Nonlinear Acoustic Behavior in a Nickel-Base Superalloy, AFRL-ML-WP-TR-2004-xxxx, Materials & Manufacturing Directorate, AF Research Laboratory, AF Materiel Command, WPAFB, OH 45433-7750, September 2004.

Hutson, A.L., Neslen, C.L., and Nicholas, T., "Characterization of Fretting Fatigue Crack Initiation Processes in Ti-6Al-4V," *Tribology Int'l*, Vol. 36, No. 2, pp. 113-144.

12.0 LIST OF MANUSCRIPTS

- Ashbaugh, N.E., Porter, J.W., Rosenberger, A.H., and Sunder, R., "Environment-Related Load History in Elevated Temperature Fatigue of a Nickel-Base Superalloy," *Proceedings of the Eighth International Fatigue Congress*, A.F. Blom, Ed., Engineering Materials Advisory Services, LTD., West Midlands, U.K., pp. 1275-1282.
- Brockman, R.A., "Analysis of Elastic-Plastic Deformation in TiAl Polycrystals," *International Journal of Plasticity*.
- Brockman, R.A., G.J. Frank, and S.E. Olson, "Elastic-Plastic Stress Analysis of Gamma Titanium Aluminide Polycrystals," *Proceedings 3rd International Symposium on Structural Intermetallics*, Jackson Hole, WY, 23-27 September 2001.
- Buchanan, D.J., John, R., and Zawada, L.P., "Creep Rupture Behavior of $\pm 45^\circ$ Oxide/Oxide Nextel720/AS Composite," *Proceedings of the 27th Annual Cocoa Beach Conference and Exposition*, The American Ceramic Society, January 2003.
- Buchanan, D.J., John, R., and Zawada, L.P., "Notched Fracture Behavior of Oxide/Oxide NextelTM720/AS Composite," *Proceedings American Ceramics Society 2000 Conference and Exposition*, Cocoa Beach, FL, 23-28 January 2000.
- Buchanan, D.J., Kramb, V.A., John, R., and Zawada, L.P., "Effect of Small Effusion Holes on Creep Rupture Behavior of Oxide/Oxide NextelTM720/AS Composite," *Proceedings of the 25th Annual Cocoa Beach Conference and Exposition*, The American Ceramic Society, January 2001.
- Dolley, E.J. Jr., Ashbaugh, N.E., and Worth, B.D., "High-Cycle-Fatigue Behavior and Life Estimates of a Gamma Titanium Aluminide," *Life Prediction Methodologies for Aerospace Materials*, Interim Annual Report for Period 25 May 1998 – 24 May 1999, AFRL-ML-WP-TR-2001-4007, pp. 87-98.
- Frank, G.J., Olson, S.E., and Brockman, R.A., "Numerical Models of Orthotropic and Lamellar Grain Structures," *Intermetallics*, April 2003, vol. 11, issue 4, pp 331-340. Garner, D.I., Sieverding, M., and Johansen, K., "User's Manual for the Compact Fiber Test Machine," UDRI-TR-00-00060, February 2000.
- Hartman, G.A. and Larsen, J.M., "Infrared Damage Detection System," web site, Society of Experimental Mechanics and AFOSR, http://sem.org/afosr/Hartman_top.asp, July, 2002.
- Huston, A.L., Niinomi, M., Nicholas, T., and Eylon D., "Effect of Various Surface Conditions on Fretting Fatigue Behavior of Ti-6Al-4V," *International Journal of Fatigue*, 2002, Vol. 24, pp. 1223-1234.
- Hutson, A. L., Conner, B. and Chambon, L., "Observations of Fretting Fatigue Micro-damage of Ti-6Al-4V," *Wear*, 2003, Vol. 255, No. 1-6, pp. 259-268.
- Hutson, A.L. And Nicholas, T., "Fretting Fatigue Behavior of Ti-6Al-4V against Ti-6Al-4V under Flat-on-Flat Contact with Blending Radii," *Fretting Fatigue: Current Technology and Practices*, ASTM STP 1367, D.W. Hoepfner, V. Chandrasekaran and C.B. Elliot, Eds., American Society for Testing and Materials, 1999, pp. 308-321.
- Hutson, A.L., and Nicholas, T., "Effect of Flat-on-Flat Contact Fretting Fatigue on the Fatigue Life of Ti-6Al-4V," *Proceedings of the National Conference on High Cycle Fatigue*, Monterey, CA, U.S. Air Force, Feb. 1999, on compact disc.
- Hutson, A.L., Ashbaugh, N.E., and Nicholas, T., "An Investigation of Fretting Fatigue Crack Nucleation Life of Ti-6Al-4V Under Flat-on-Flat Contact" *Fretting Fatigue: Advances in Basic Understanding and Applications*, STP 1425, Y. Mutoh, S.E. Kinyon, and D.W. Hoepfner, Eds., ASTM International, 2003, pp. 307-322.
- Hutson, A.L., Nicholas, T., and Stubbs, D., "Characterization of Fretting Fatigue Crack Nucleation Life

of Ti-6Al-4V in a Flat-on-Flat Contact," Proceedings of the National Conference on High Cycle Fatigue, Chandler, AZ, US Air Force, Mar. 2000, on compact disc.

Hutson, A.L., Nicholas, T., Olson, S. and Ashbaugh, N., "In Search of a Parameter for Fretting Fatigue," Advances in Fracture Research, Proceedings of ICF-10, K. Ravi-Chandar, B.L. Karihaloo, T. Kishi, R.O. Ritchie, A.T. Yokobori Jr. and T. Yokobori, Eds., Paper # 0809, CD ROM, Elsevier, 2001.

Hutson, A.L., Nicholas, T., Olson, S.E., and Ashbaugh, N.E., "Effect of Sample Thickness on Local Contact Behavior in a Flat-on-Flat Fretting Fatigue Apparatus," International J. of Fatigue, November 2001, Vol. 23, pp. S445-S454.

Hutson, A.L., Nicholas, T., Olson, S.E., and Ashbaugh, N.E., "Effect of Normal to Shear Load Ratios on HCF Stress Limit Under Fretting Fatigue Conditions," Proceedings of 6th National Turbine Engine HCF Conference, Jacksonville, FL, 5-8 March 2001, on compact disc.

Hutson, A.L., Stubbs, D.A., and Nicholas, T., "An Investigation of Fretting Fatigue Crack Nucleation Life Using Shear Wave NDT," Experimental Mechanics, May 2004, Review pending.

Hutson, A.L.; Neslen, C.; and Nicholas, T., "Characterization of Fretting Fatigue Crack Initiation Processes in Ti-6Al-4V," Tribology International, 2003, Vol. 36, No. 2, pp. 113-144.

Hutson, A.L.; Olson, S.; and Nicholas, T.; "Fretting Fatigue of Dissimilar Metals," Proceedings of 7th National Turbine Engine High Cycle Fatigue Conference, West Palm Beach, FL, May 2002, on compact disc.

Jha, S. K., J. M. Larsen, A. H. Rosenberger and G. A. Hartman, "Dual Fatigue Failure Modes in Ti-6Al-2Sn-4Zr-6Mo and Consequences on Probabilistic Life Prediction," Scripta Materialia, Vol. 48, pp. 1637-1642, 2003.

Jha, S. K., J. M. Larsen, A. H. Rosenberger and G. A. Hartman, "Variability in Fatigue Life of Ti-6Al-2Sn-4Zr-6Mo," In Press, Materials Science and Engineering A, 2004.

Jha, S. K., Larsen, J. M., Rosenberger, A. H., and Hartman, G. A., "Mechanism-Based Variability in Fatigue Life of Ti-6Al-2Sn-4Zr-6Mo," Probabilistic Aspects of Life Prediction, ASTM STP 1450, W. S. Johnson and B. M. Hillberry, Eds., ASTM International, West Conshohocken, PA, 2004, pp. 116-127.

John, R. and Buchanan, D.J., "Bridging Stress Distributions During Fatigue Crack Growth in Continuously Reinforced [0] Metal Matrix Composites," Vol. 23, No. 2, 2001, pp. 69-81.

John, R., Buchanan, D., and Zawada, L.P., "Fracture and Creep Rupture Behavior of Notched Oxide/Oxide and SiC/SiC CMC," Proceedings of the 10th Int'l Congress of Fracture, Honolulu, HI, 3-7 December, 2001, on compact disc.

John, R., Buchanan, D.J., and Zawada, L.P., "Creep Deformation and Rupture Behavior of a Notched Oxide/Oxide Nextel™720/AS Composite," Proceedings of American Ceramics Society 2000 Conference and Exposition, Cocoa Beach, FL, 23-28 January 2000, on compact disc.

John, R., Buchanan, D.J., Kramb, V.A., and Zawada, L.P., "Creep Rupture Behavior of Oxide/Oxide Nextel®720/AS and MI SiC/SiC Composites with Effusion Holes," Ceramic Engineering & Science Proceedings, 26th Annual Conf. on Composites, Advanced Ceramics, Matls., and Structures: A, The American Ceramic Society, Westerville, OH, 2002. Paper No.ECD2-L-02.

John, R., DeLuca, D., Porter, W.J., and Rosenberger, A.H., "Mixed Mode Crack Growth in a Gamma Titanium Aluminide," Fatigue '99: Proceedings of the Seventh International Fatigue Conference, X.R. Wu and Z.G. Wang, Eds., Higher Education Press, Beijing, PRC, and Engineering Materials Advisory Services Ltd., Midlands, UK, 1999, pp. 1567-1572.

- John, R., Lackey, A.F., and Ashbaugh, N.E., "Cyclic Crack Propagation Parallel to Fibers in a Unidirectionally Reinforced Metal Matrix Composite," submitted to *Composite Science and Technology*, May 2000.
- John, R., Larsen, J.M., Buchanan, D.J., and Ashbaugh, N.E., "Incorporating Residual Stresses in Life Prediction of Turbine Engine Components," Proceedings of Fatigue 2002, Stockholm, Sweden, 2-7 June 2002, p. 1063-1070.
- John, R., Larsen, J.M., Buchanan, D.J., and Ashbaugh, N.E., "Incorporating Residual Stresses in Life Prediction of Turbine Engine Disks," NATO RTO Symposium on Monitoring and Management of Gas Turbine Fleets for Extended Life and Reduced Costs, 8-11 October 2001, on compact disc.
- John, R., Porter, W.J., Johnson, D.A., and Olson, S., "Colony Property Determination in a Gamma Titanium Aluminide," Structural Intermetallics 2001 (ISSI3), eds K.J. Hemker, D.M. Dimiduk, H. Clemens, R. Darolia, H. Inui, J.M. Larsen, V.K. Sikka, M. Thomas and J.D. Whittenberger (TMS Warrendale PA, 2001), pp 339-346.
- John, R., Rosenberger, A.H., Porter, W.J., DeLuca, D.P., and Li, K., "Mixed Mode Crack Growth in a Gamma Titanium Aluminide Alloy," Gamma Titanium Aluminides 1999, Y-W Kim, D.M. Dimiduk, and M.H. Loretto, Eds., TMS, Warrendale, PA, 1999, pp. 535-540.
- John, R., W.J. Porter, III*, and S. Olson, "Measurement and Modeling of Orthotropic Elastic Behavior of Grains in a Gamma Titanium Aluminide Alloy," *Intermetallics*, 12, (2004), pp.1-9.
- Kramb, V.A., and John, R., "Damage Progression from Notches in an Oxide/Oxide Ceramic Matrix Composite Using Ultrasonic C-Scans," submitted to *Composites Science and Technology*, May 2000.
- Kramb, V.A., Buchanan, D.J., and John, R., "Damage Progression from Notches in an Oxide/Oxide Ceramic Matrix Composite under Sustained Loads," Life Prediction Methodologies for Aerospace Materials, Interim Annual Report for Period 25 May 1999 – 24 May 2000, AFRL-ML-WP-TR-2001-4020, pp. 113-134.
- Kramb, V.A., Buchanan, D.J., John, R., and Zawada, L.P., "In-Plane Shear Behavior in Oxide/Oxide Ceramic Matrix Composites at Room and Elevated Temperature," Life Prediction Methodologies for Aerospace Materials, Interim Annual Report for Period 25 May 2001 – 24 May 2002, AFRL-ML-WP-TR-200x-xxxx, pp. 111-124.
- Kramb, V.A., John, R., and Zawada, L.P., "Fracture Behavior of an Oxide/Oxide Ceramic Matrix Composite," *J. American Ceramic Society*, Vol. 82, No. 11, 1999, pp. 3087-3096.
- Larsen, J.M., John, R., Russ, S.M., Maxwell, D.C., Worth, B.D., Rosenberger, A.H., Li, K., and Porter, W.J., "The Role of Near-Threshold Small-Crack Behavior in Life Prediction of Titanium Alloys for Use in Advanced Turbine Engines," Small Fatigue Cracks: Mechanics and Mechanisms, K.S. Ravichandran, R.O. Ritchie, and Y. Murakami, Eds., Elsevier Science, Oxford, UK, 1999, pp. 131-142.
- Larsen, J.M., Rosenberger, A.H., and Hartman, G.A., "A Mission-Element Approach for Crack Growth under Turbine Engine Spectra," Proceedings of Fatigue 2002, Stockholm, Sweden, 2-7 June 2002, pp. 1029-1036.
- Larsen, J.M., Rosenberger, A.H., Li, K., Porter, W.J., and John, R., "Tailoring TiAl Intermetallic Alloys to Satisfy Damage Tolerance Requirements for High Performance Turbine Engines," Fatigue '99: Proceedings of the Seventh International Fatigue Conference, X.R. Wu and Z.G. Wang, Eds., Higher Education Press, Beijing, PRC, and Engineering Materials Advisory Services Ltd., Midlands, UK, 1999, pp. 1559-1566.
- Larsen, J.M., Rosenberger, A.H., Worth, B.D., Li, K., Maxwell, D.C., and Porter, W.J., "Assuring Reliability of Gamma Titanium Aluminides in Long-Term Service," Gamma Titanium Aluminides 1999, Y-W. Kim, D.M. Dimiduk, and M.H. Loretto, Eds., TMS, Warrendale, PA, 1999, pp. 463-472.

- Li, K., N. E. Ashbaugh and A. H. Rosenberger, "Effects of Defects on Crack Initiation of IN100 (P/M) Under Low Cycle Fatigue Conditions," Proceedings of Fatigue 2002, Stockholm, Sweden, 2-7 June 2002, pp. 851-858.
- Li, K., Porter, W.J., Rosenberger, A.H. and Larsen, J.M., "Defects in Wrought Gamma Titanium Aluminides," Fatigue '99 - Proceedings of the Seventh International Fatigue Conference, X.R. Wu and Z.G. Wang, eds., Higher Education Press, Beijing, PRC, and Engineering Materials Advisory Services Ltd., Midlands, UK, 1999, pp. 1597-1602.
- Li, K., Porter, W.J., Rosenberger, A.H., and Larsen, J.M., "Lamellar Colony Orientation Determination in Gamma Titanium Aluminides Using Orientation Imaging Microscopy (OIM)," Proceedings 11th AeroMat Conference & Exposition, ASM International, Bellevue, WA, 26-29 June, 2000.
- Li, K., Rosenberger, A.H., Worth, B.D., Larsen, J.M., and Porter, W.J., "Effects of Microstructural Anisotropy on Fatigue Behavior of Gamma TiAl Alloys," submitted to *Fatigue & Fracture of Engineering Materials & Structures*, July 2001.
- Li, K.; Porter, W.J.; and Rosenberger, A.H., "Macro-segregation in Gamma Titanium Aluminides," submitted to *Intermetallics*, August 2002.
- Martinez, C.M., Birkbeck, J.C., Eylon, D., Ruschau, J.J., Thompsom, S.R., Porter, W.J., and Nicholas, T., "Characterization of FOD Impact Sites on Ti-6Al-4V Simulated Airfoils," to be published in the Proceedings of the 5th National Turbine Engine High Cycle Fatigue Conference, Chandler, AZ, March 7-9, 2000.
- Nicholas, T. and Maxwell, D.C., "Evolution and Effects of Damage in Ti-6Al-4V under HCF," Eighth International Conference on the Mechanical Behaviour of Materials, Victoria, BC, pp. 16-21 May 1999
- Nicholas, T., Hutson, A. L., John, R. and Olson, S. E., "A Fracture Mechanics Methodology Assessment for Fretting Fatigue," *International Journal of Fatigue*, Vol. 25, pp. 1069-1077, 2003.
- Niinomi, M., Hutson, A. L., Shell, E. B., Eylon, D., and Nicholas, T., "Effect of Cu-Ni Plasma Coating on Fretting Fatigue Characteristics of Ti-6Al-4V Under Flat-on-Flat Contact" Fretting Fatigue: Advances in Basic Understanding and Applications, STP 1425, Y. Mutoh, S.E. Kinyon, and D.W. Hoepfner, Eds., ASTM International, 2003.
- Porter, W.J., John, R., Olson, S., and Li, K., "Elastic Behavior of Fully Lamellar Gamma Titanium Aluminides," Ashbaugh, N.E., et al., Life Prediction Methodologies for Aerospace Materials, Interim Annual Report for Period 25 May 2000 – 24 May 2001, AFRL-ML-WP-TR-2001-4153, pp. 31-38.
- Porter, W.J., Li, K., Rosenberger, A.H., and Dimiduk, D.M., "Primary Melting Issues Related to Gamma Titanium Aluminides," Structural Intermetallics 2001 (ISSI3), eds K.J. Hemker, D.M. Dimiduk, H. Clemens, R. Darolia, H. Inui, J.M. Larsen, V.K. Sikka, M. Thomas and J.D. Whittenberger (TMS Warrendale PA, 2001), pp. 201-206.
- Porter, W.J., Li, K., Rosenberger, A.H., and Larsen, J.M., "Processing Issues in Gamma Titanium Aluminides," Gamma Titanium Aluminides 1999, Y-M Kim, D.M. Dimiduk, and M.H. Loretto, Eds., TMS, Warrendale, PA, 1999, pp. 587-593
- Porter, W.J., R. John, and S. Olson, "Determination of Young's Modulus in Large-grain Gamma Titanium Aluminides," *Scripta Materialia*, 49 (2003) pp. 327-332.
- Sunder, R., "Fatigue by Diffusion-Induced Brittle Micro-Fracture," submitted to *Fatigue and Fracture of Eng Mats & Structures*, July 2002.
- Sunder, R., "Microscopic Markers Reveal Root of the Fatigue Process in Al Alloys," *ASM Advanced Materials and Processes*, Vol. 159, No. 4, 2001, pp. 41-42.

Sunder, R., Ashbaugh, N.E., Porter, W.J., and Rosenberger, A.H., "Multi-Mechanism Synergy in Variable-Amplitude Fatigue", Fatigue Testing and Analysis Under Variable Amplitude Loading Conditions, ASTM STP 1439 , P.C McKeighan and N. Ranganathan, Ed(s)., ASTM International, West Conshohocken, PA, 2004, in press.

Sunder, R., Porter, W.J., and Ashbaugh, N.E., "Fatigue Voids and Their Significance," *Fatigue & Fracture of Eng Materials and Structures*, 2001, Vol. 25, Issue 11, November 2002, pp. 1015-1024.

Sunder, R., W.J. Porter and N.E. Ashbaugh, "The Role of Air in Fatigue Load Interaction," *Fatigue and Fracture of Engineering Materials & Structures*, Vol. 26, Issue 1, January 2003, pp. 1-16.

Tandon, G.P., Buchanan, D.J., Pagano, N.J., and John, R., "Effective Elastic and Thermal Properties of a Damaged Woven Oxide/Oxide Composite," submitted to the Journal of American Ceramics Society, February 2002.

APPENDIX
COMPILATION OF MANUSCRIPTS

Paper	Page
C1 Buchanan, D.J., R. John, N.E. Ashbaugh, “Thermal Residual Stress Relaxation in Powder Metal IN100 Superalloy,” <i>J ASTM International</i> , May 2004 Vol. XX, No. X	47
C2 , Lee, H., and Mall, S., “Effect of Dissimilar Metals on Fretting Fatigue Behavior of Ti-6Al-4V,” submitted to <i>Tribology Int’l</i>	63
C3 Hutson, A.L. and Shamachary Sathish, “Ti-6Al-4V Fretting Fatigue Crack Precursor Damage Characterization,” 9th National Turbine Engine HCF Conference; Pinehurst NC; March 2004.	74
C4 Hutson, Alisha L. and David Stubbs, “A Fretting Fatigue Crack Detection Feasibility Study Using Shear Wave NDI,” Society for Experimental Mechanics.	85
C5 Buchanan, Dennis J., Reji John, and Larry P. Zawada, “Off-axis Creep Behavior of Oxide/Oxide Nextel™720/AS-0,” Proceedings 27th Ann Conf on Ceramics.	100

Thermal Residual Stress Relaxation in Powder Metal IN100 Superalloy

ABSTRACT: Relaxation of shot peened induced compressive residual stresses due to thermal exposure was measured using x-ray diffraction. The material used in this study was a hot isostatically pressed (HIP) power metal (PM) IN100 nickel base superalloy. A total of 14 IN100 samples were shot peened to an Almen intensity of 6A using MI-170-R shot with 125% coverage. The sample dimensions were nominally 16 x 13 x 4 mm thick with an irradiated x-ray region of 8 x 5 mm. Residual stress measurements were made at the surface and at nominal depths of 12, 25, 50, 75, 125, 175, 250 and 350 microns. The shot peened samples were thermal exposed to two temperatures (650, 704°C) and a range of exposure times (0.5 – 300 hours). Residual stress measurements on shot peened samples without thermal exposure were used as a basis for comparison. The relaxation of shot peened compressive residual stresses under purely thermal loading was examined. Results from this study show that shot peened compressive residual stresses change significantly with thermal exposure. The residual stresses exhibited an initial rapid decrease on the surface and in the depth at both temperatures. However, continued thermal exposure produced little or no change in surface residual stresses while peak compressive stresses in the depth continued to relax with time at both temperatures.

KEYWORDS: residual stress, shot peen, thermal exposure, thermal relaxation, stress relaxation, IN100, superalloy, x-ray, cold work

Introduction

Shot peening components to impart a compressive residual surface stress for retardation of crack initiation and crack growth has been employed for many years. Numerous studies have characterized the beneficial effects of compressive residual surface stresses on fatigue life [1-5]. In design applications that utilize aluminum and titanium alloys, subjected to moderate temperatures and stresses, the residual stresses can be assumed to be stable with repeated cyclic stress controlled loading. In contrast, nickel based superalloys are typically selected for applications where temperatures reach 70% of the melting temperature and stresses approach the yield strength. Hence, under elevated temperature and high stress loading conditions plasticity, creep and relaxation will alter the residual stress depth profile. Additional complications are caused by changes to the microstructure and mechanical behavior from shot peening and long term elevated temperature exposure.

Accurate characterization of the initial residual stress and plastic strain state depth profiles are required for accurate prediction of the evolution of stresses and plastic strains with applied thermal and mechanical loading. The accuracy of predictions depends on accuracy of the initial

Air Force Research Laboratory, Materials and Manufacturing Directorate, AFRL/MLLMN, 2230 Tenth Street, Suite No. 1, Wright-Patterson Air Force Base, Ohio 45433-7817, U.S.A.

* University of Dayton Research Institute, 300 College Park, Dayton, Ohio 45469, U.S.A.

conditions, specifically the residual stresses and plastic strains. There are many variables that affect the residual stress and plastic strain depth profile. The elastic and inelastic material properties of the material itself have a pronounced effect on the resulting residual stress and plastic strain profile. For example, machining and surface finishing processes prior to shot peening such as grinding and polishing all impart residual stresses into the component. The shot peening process itself has many variables that contribute to variability of imparted residual stresses; shot size, hardness, coverage and angle just to name a few. There have been several empirical and physics based models developed to determine the residual stress depth profile as a function of material properties and shot peening parameters [6-9,21]. These models are useful for designers who wish to incorporate the beneficial effects of residual stresses for retardation of fatigue crack initiation and growth into life prediction. In some cases cyclic stress relaxation is incorporated into life prediction models to account for changing residual stress profiles and their effect of fatigue life. However, thermal relaxation of residual stresses is often overlooked or ignored. The failure to incorporate thermal residual stress relaxation could result in a nonconservative estimate of both fatigue crack initiation and crack growth resistance and ultimately a component that will not meet an expected design lifetime.

The aim of this paper is to describe an experimental program developed using design of experiments (DOE) concepts coupled with experimental mechanics and analytical modeling to produce reliable experimental thermal residual stress relaxation data for a nickel base superalloy, IN100. Further, this paper will present the experimental results and discuss observed thermal relaxation behavior as a function of temperature and exposure time.

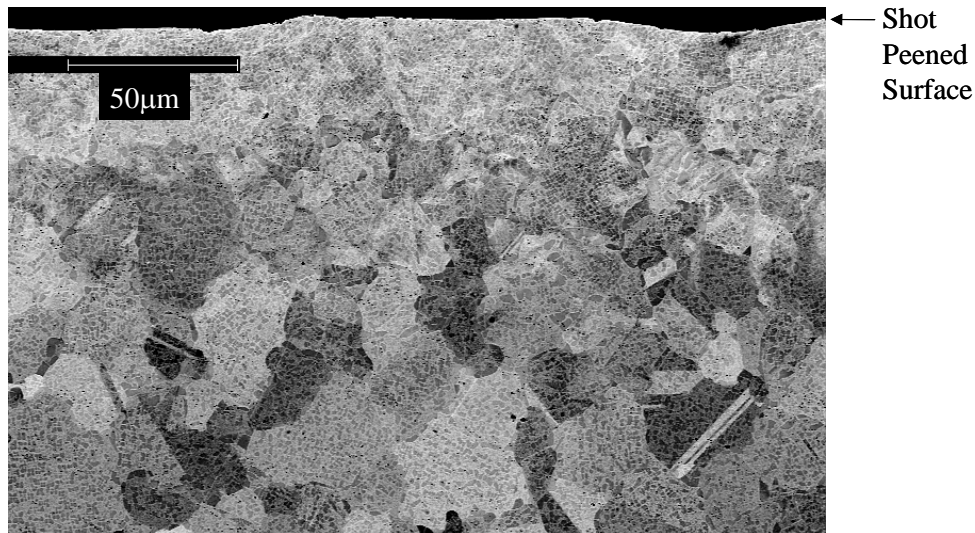


FIG. 1— *Cross section of IN100 as shot peened microstructure (no thermal exposure).*

Material

IN100 is a powder metal (PM) nickel base superalloy with Face Centered Cubic (FCC) structure with a nominal grain size of 20-25 μm , similar to the alloy described by Wusatowska-Sarnek et. al. [11,12]. Scanning electron microscopy (SEM) analysis of the baseline (no

exposure) and the extreme exposure (704°C @ 300hr) show no apparent differences in the microstructure. For example, there was no difference in grain size, no γ' coarsening, or no new phases present. However, there were obvious changes to the microstructure on all samples near the shot peened surface. Material deformation, cavities and even embedded shot fragments were found on the surface of the samples. Figure 1 is a micrograph of a polished section of IN100. The top of the image was the surface of the material that was shot peened. The top 50 μ m show a distinct change in microstructure resulting from the shot peening induced deformation. The bottom portion shows the interior and a typical representation of the microstructure and individual grains.

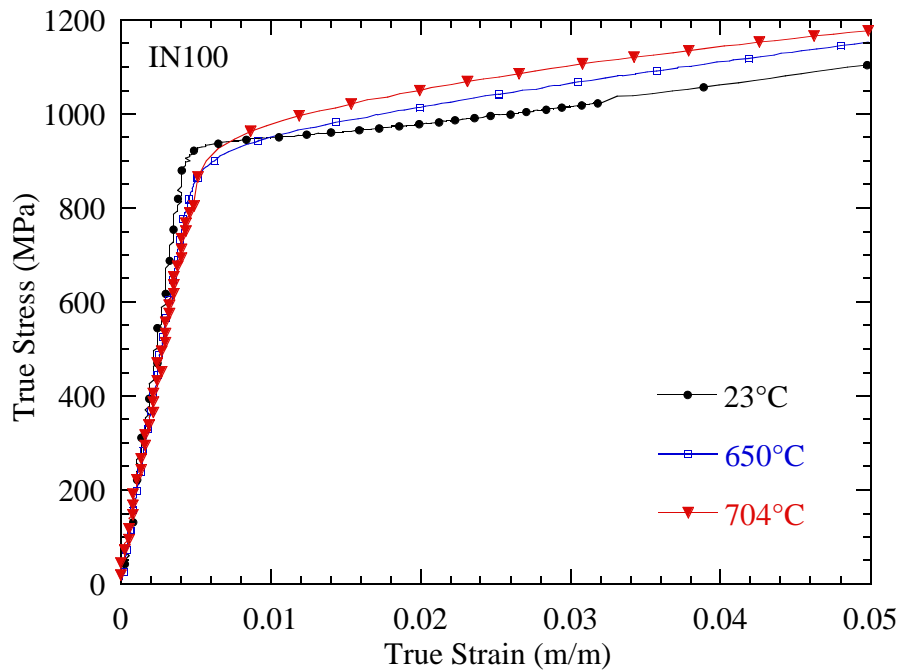


FIG. 2— Monotonic true stress-true strain curves for IN100 at temperatures 23°C, 650°C, and 704°C.

The monotonic true stress – true strain data for IN100 at temperatures (23, 650 and 704°C) are shown in Fig. 2. During the course of each tension test a low-stress (≈ 200 MPa) elastic loading cycle was performed at room temperature and at the intended test temperature. Fine ranges on the load cell and extensometer were used to accurately measure the elastic modulus during the elastic loading cycles. The elastic loading was performed multiple times to determine the repeatability of the modulus measurements. All tensile tests were performed in displacement control with the control signal generated by a 16-bit D/A function generator. The displacement rate in the elastic region ($< \sigma_y$) was nominally 0.007 mm/s and was increased by a factor of ten to 0.07 mm/s in the inelastic region to reduce the possible inclusion of time dependent behavior, creep, at elevated temperatures. A quartz-lamp heating unit with four-zone temperature control was used for the elevated temperature tension tests. Four K-type thermocouples were used to measure and control the temperature of the test specimen. Four-zone temperature control

provided the capability to minimize the temperature gradients through the specimen thickness and along the loading axis of the specimen. Thermal profile maps on the specimen showed that the specimen was uniformly heated over the entire gage section of the specimen. Applied load, temperature, displacement and extensometry data were collected during tensile tests. All tests were conducted in laboratory air using a computer controlled servo-hydraulic test system [10].

Specimen Design

Specimen design should not be trivialized as a simple task. For many standardized tests such as tensile, creep and fatigue, the specimen geometry is specified in the testing standard to avoid the pitfalls of specimen design. Research projects with a significant experimental program should not be compromised by a poorly designed specimen geometry. The cost of raw material, machining, preparation, testing and analysis of the data makes for a large financial investment that often cannot be repeated. In this study a great deal of effort was devoted to designing the specimen based on the mechanics of the shot peening process, the experimental testing program and anticipated modeling efforts.

First and foremost was identification of all steps involved in the experimental procedures and the analytical analysis of the experimental x-ray diffraction (XRD) data to be collected. After identification of limiting factors such as material availability, size of test matrix, experimental and analytical requirements a rectangular parallelepiped geometry was chosen. Final dimensions of the sample were based on the XRD experimental techniques and finite element (FE) analysis of residual stress profiles and layer removal simulations.

A three dimensional FE model with quarter symmetry was used to provide insight for selecting dimensions of the sample. Based on residual stress depth profiles from another superalloy, IN718 [14,15] and typical shot peening specifications for turbine engine components, an Almen intensity of 6A was selected [3]. A temperature profile was imposed on the FE model to produce a residual stress depth profile similar to that measured on IN718 with an Almen intensity of 6A [3].

The in-plane dimensions were based on the grain size of the material, nominally 20-25 μm , the desired irradiated x-ray region (5 x 8mm), the electropolishing region and the anticipated shot peened residual stress profile. The irradiated region was maximized to measure an average residual stress over as many grains as possible. A constant biaxial compressive residual stress was desired over the entire (5 x 8mm) irradiated region. To achieve the constant biaxial compressive stress state over the entire irradiated region requires a surrounding border of material sufficiently wide to allow the normal stresses to decay to zero at the free surface. FE analysis was employed to determine the necessary amount of material surrounding the irradiated region needed for the residual stresses decay to zero at the free surface. A 4mm wide band of material was sufficient to have a uniformly stressed 5 x 8mm measurement region. Figure 3 is a plot of the in-plane surface residual stresses (σ_{xx} and σ_{yy}) along a centerline from the center of the specimen to the edge of the specimen in the X-direction. The thick solid line represents half the length (4 mm) of the irradiated region in the X-direction. The solid circles and solid rectangles are stresses in the x and y-direction, respectively, as a function of distance in the x-direction. The stresses are equal in value and constant over the range of the XRD measurement region. Both stresses decrease in magnitude as they approach the edge of the sample. The stress in the x-direction changes rapidly as it approaches the free surface where it becomes zero. Figure 4 is a plot of the in-plane surface residual stresses (σ_{xx} and σ_{yy}) along a centerline from

the center of the specimen to the edge of the specimen in the y-direction. This line is perpendicular to the line described in Fig. 3. The thick solid line represents half the width (2.5 mm) of the irradiated region in the y-direction. Both stresses decrease in magnitude as they approach the edge of the sample. The stresses in the y-direction change rapidly as it approaches the free surface where it becomes zero.

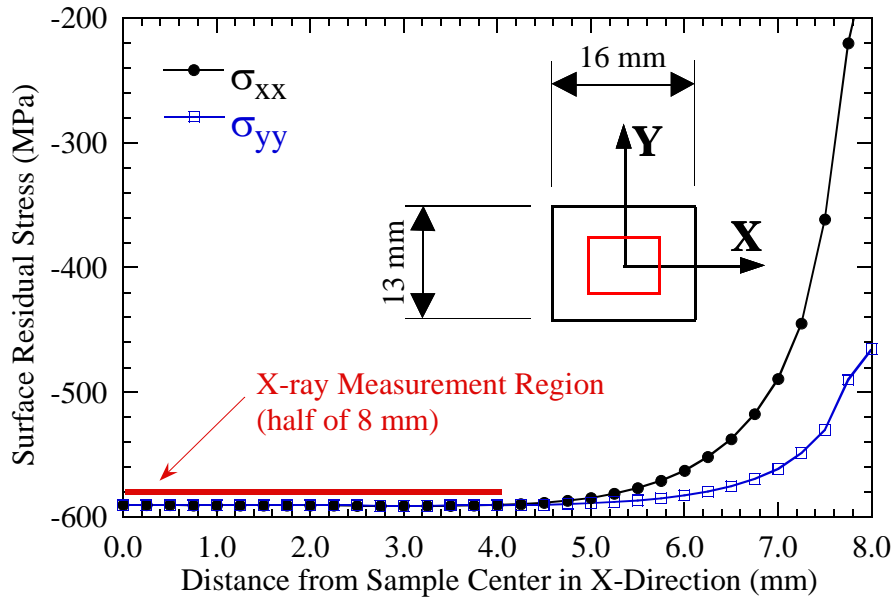


FIG. 3— Profile of FE simulated surface residual stresses (σ_{xx} and σ_{yy}) from the center of sample to edge of sample in x-coordinate direction.

XRD measurements are interpreted on the diffraction of radiation reflected from the surface and to a depth of approximately 10 microns, for this material. Since the technique measures an average throughout a volume it was important to have a uniform stress field in the plane of the material. Nonlinear gradients in the plane of the stress field would not be captured and would produce erroneous errors in the measured residual stress. Using the assumption that the stress is equally biaxial and only varies as a function of the depth, corrections for volume averaging can be made for electropolishing and for subsequent depth measurements.

Another aspect considered was out-of-plane displacement associated with shot peening one side of the specimen at a time. A specimen that is too thin would produce an excessive amount of out-of-plane displacement and will not be able to be placed back in the shot peening fixture. The FE model was used to determine the amount of out-of-plane deformation produced by shot peening a single side of the plate. The FE model was also used to simulate layer removal by electropolishing for depth measurements and the resulting out-of-plane displacement. Based on these analyses and recommendations from the shot peening vendor, Metal Improvement Company, Inc. of Blue Ash, OH, a specimen thickness of 4mm was chosen.

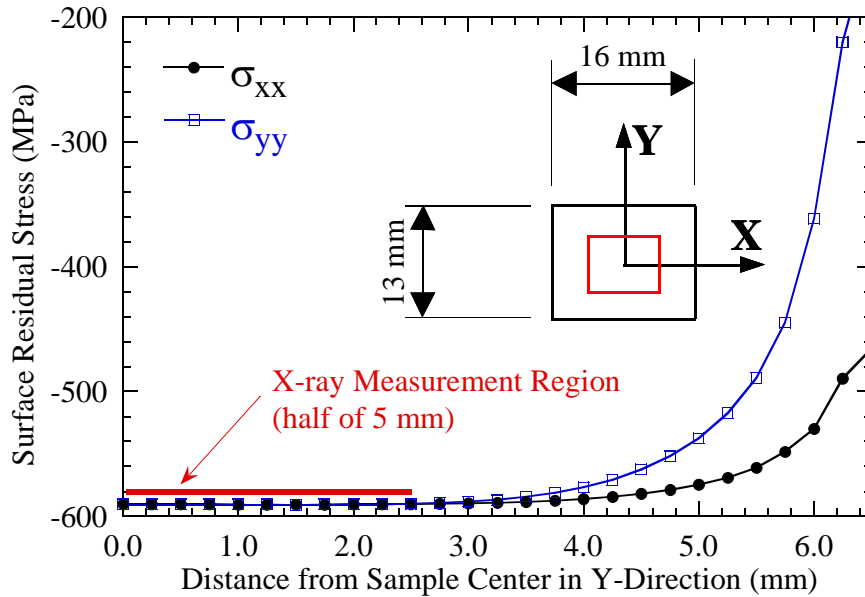


FIG. 4— Profile of FE simulated surface residual stresses (σ_{xx} and σ_{yy}) from the center of sample to edge of sample in y-coordinate direction.

Shown in Fig. 5 are the final specimen dimensions and cutout plan from the parent plate. The samples were taken from a 3 x 3 matrix of samples with the parent plate measuring 49mm x 40mm x 4mm in size. In an effort to minimize the variation in shot peening from specimen to specimen the plates were shot peened first then split into the final sample dimensions via electro-discharge machining (EDM). Machining and shot peening the larger plates also reduced costs and made fixturing and shot peening profiles more repeatable.

Shot Peening Conditions

The IN100 superalloy was shot peened to an Almen intensity of 6A-0+2 using a MI-170-R (SAE 170 max. cast steel shot, regular) shot with 125% coverage. PEENSCAN® was applied prior to shot peening to verify complete coverage and uniformity over the entire surface of the plates [13]. A total of six plates were shot peened, only three were used for this study. The three plates (A2, B2, C1) used in this study, as shown in Table 1, were all shot peened at the same time. Both sides of the plates were shot peened simultaneously to reduce out-of-plane deformation often associated with shot peening a single side.

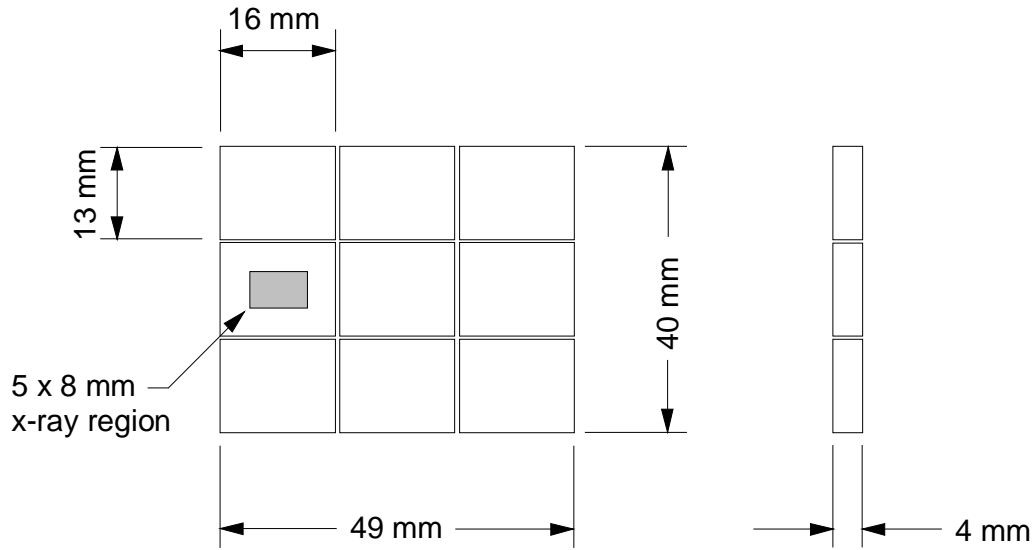


FIG. 5— Schematic of cutout plan for shot peened plates of IN100 for thermal exposure and x-ray analysis.

Test Conditions & Thermal Exposure Procedure

Thermal residual stress relaxation data in the literature [20-23] have shown that both temperature and exposure time have a significant affect on relaxation of stress and reduction in cold work depth profiles. The stress relaxation rates are driven material properties, temperature, residual stress and cold work depth profiles. Exposure times and temperatures where selected on the basis of expected usage temperatures for this alloy.

TABLE 1—Temperature and thermal exposure time matrix for IN100.

Plate #	B2	C1	A2
	Temperature		
Exposure Time (hours)	73°F	1200°F	1300°F
	23°C	650°C	704°C
0.0	x	x	x
0.5		x	x
1.0		x	x
3.0			x
10.0		x	x
100.0			x
300.0		x	x

To minimize specimen-to-specimen variations in thermal exposure each specimen was instrumented with a thermocouple and the temperature history logged on a strip chart recorder.

All samples, for each given elevated temperature, were placed into the furnace at the same time. Individual samples were removed from the furnace after reaching the desired exposure time. This procedure was repeated for both exposure temperatures shown in Table 1. This DOE approach minimizes errors often associated with sequential testing procedures that can include changes in furnace performance, thermocouple aging, temperature fluctuations, etc., which may be carried over multiple shifts, days or weeks. Recorded temperature measurements on specimens indicated that the specimens reached the desired exposure temperature in approximately nine minutes or less after insertion into the furnace.

Deformation Mechanism Maps (DMM) for nickel base superalloys indicate that typical turbine engine operating temperatures are nominally 0.5 to 0.6 of the melting temperature, often called the homologous temperature. The homologous temperatures for 650 and 704°C are 0.59 and 0.62, respectively. Therefore residual stress relaxation was expected to occur at these two temperatures. In general, a homologous temperature of approximately 0.8 is an upper bound usage temperature for nickel base superalloys.

X-ray Stress Analysis

The x-ray elastic constant $E/(1+\nu)$ and the cold work calibration were experimentally measured on the same source of material as the test samples for the residual stress relaxation study. The x-ray elastic constant was measured on the crystallographic direction normal to the (311) plane of the FCC lattice. Determination of the elastic constant was completed using a thin rectangular beam under four-point bending in accordance with ASTM Test Method for Determining the Effective Elastic Parameter for X-Ray Diffraction Measurements of Residual Stress (E1426) [26].

An empirical equation, based on a relationship developed by Prev y [23], was used to relate the peak width at the half height of the diffraction peak to the percent cold work. This empirical relationship was established by XRD measurements on cylindrical samples deformed in compression to a range of cold work levels. For this residual stress relaxation study the cold work was determined using the width of the (311) diffraction peak at half-height and the empirically measured relationship. X-ray diffraction measurements for residual stress were completed in accordance with SAE J784a using the diffraction radiation from the (311) planes of the FCC structure of the IN100 material.

The residual stress and cold work measurements were made at the surface and at nominal depths of 12, 25, 50, 75, 125, 175, 250 and 350 microns. Measurements were made in the direction of the short axis (13mm) of the sample at the center of the sample face. The irradiated area over which the measurements were taken was 5 x 8mm centered in the 13 x 16mm sample dimensions. This provided a 4mm border around the entire perimeter of the irradiated region for which the residual stresses to decay to zero at the free edge as discussed in the specimen design section and shown in Figs. 3 and 4.

Another opportunity to improve the consistency of the measured data and remove possible experimental uncertainties was with the electropolishing procedure for residual stress depth measurements. The entire surface of the sample was electropolished layer-by-layer. The stress corrections for layer removal were completed in accordance with the Moore and Evans [16] elasticity solution for flat plates. This avoided possible errors associated with stress gradient produced by pocket electropolishing.

Thermal Relaxation Results

Four baseline residual stress depth profiles with no thermal exposure were measured. Three of the depth profiles, one from each plate (A2, B2, C1), were measured by Lambda Research Inc. and a fourth was measured elsewhere. Each profile was interpolated to a common set of nominal depths. The average residual stress and range of measurements are shown in Fig. 6. Overall the peak compressive stresses and the overall response for all four samples were similar. The peak compressive residual stress always occurred within 50 microns of the surface, consistent with the changes in the microstructure as shown in Fig. 1.

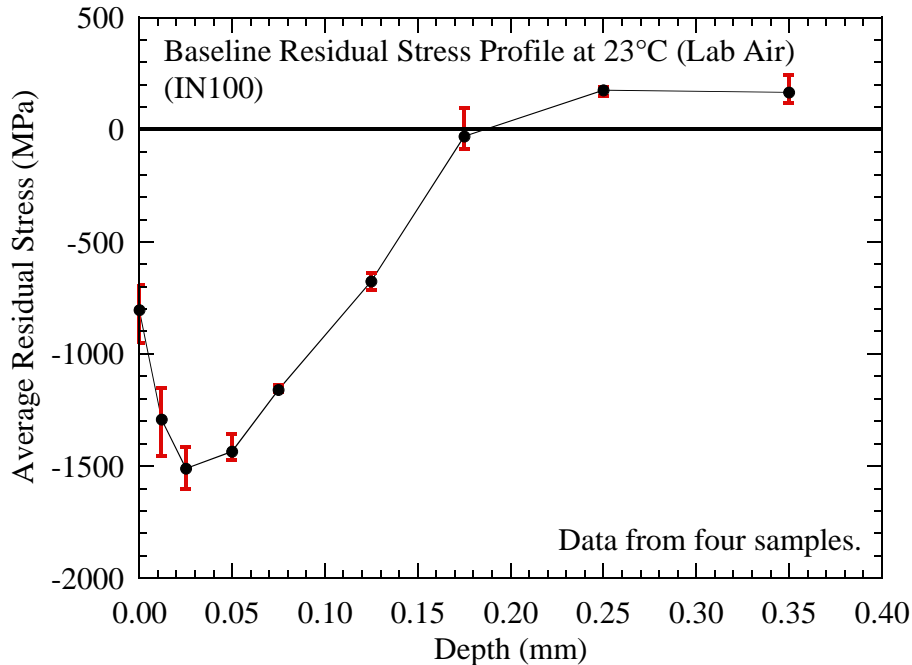


FIG. 6— *Repeatability of baseline residual stress distribution in IN100 at 23°C.*

Figures 7 and 8 show the residual stress and cold work depth profiles, respectively for IN100 thermally exposed at 650°C for up to 300 hours. These results were collected on five samples, all taken from plate (C1). A compressive surface residual stress of 250-400 MPa remained at the surface for all exposures. Stress relaxation was greatest at the free surface. The stress relaxation was less for the peak compressive stress. However, after 300 hours of exposure to 650°C residual stress retention is approximately 65%. There was also a shift of the peak compressive stress from 25 μm to approximately 75 μm . Below the free surface the residual stress profile did not follow the expected relaxation with increased exposure time. In particular at a depth of 50 to 130 μm the 300-hour exposure had a more compressive residual stress than the 10-hour exposure. In contrast, there was a clear trend of decreasing cold work with increasing exposure time as shown in Fig. 8. The cold work profiles show a large change at the surface and to a depth of approximately 175 microns with increased exposure. This depth was coincident with where the stresses are below the monotonic yield strength of the material.

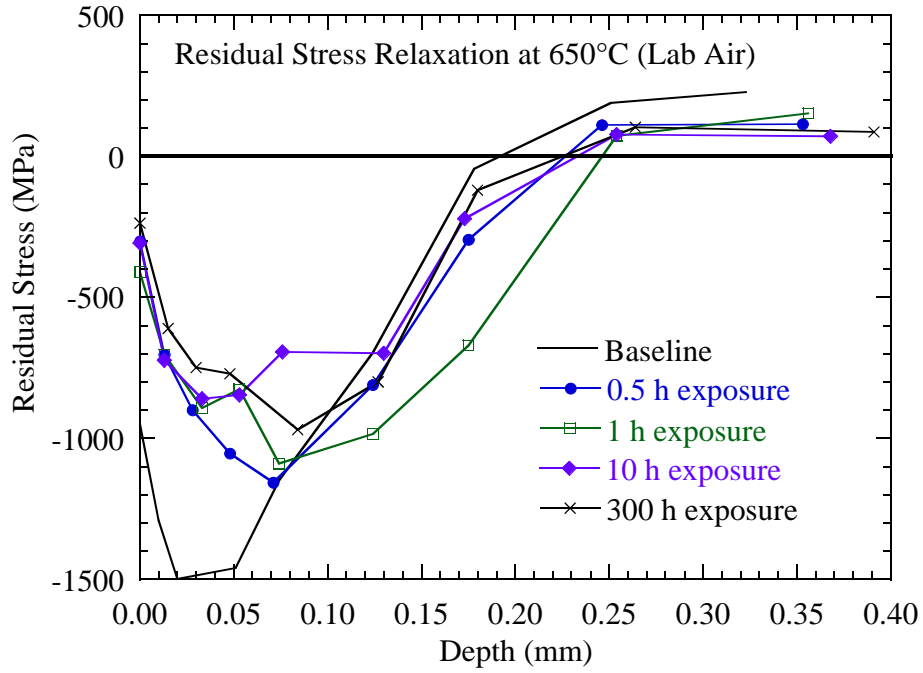


FIG. 7— Residual stress distribution in IN100 versus exposure time at 650°C.

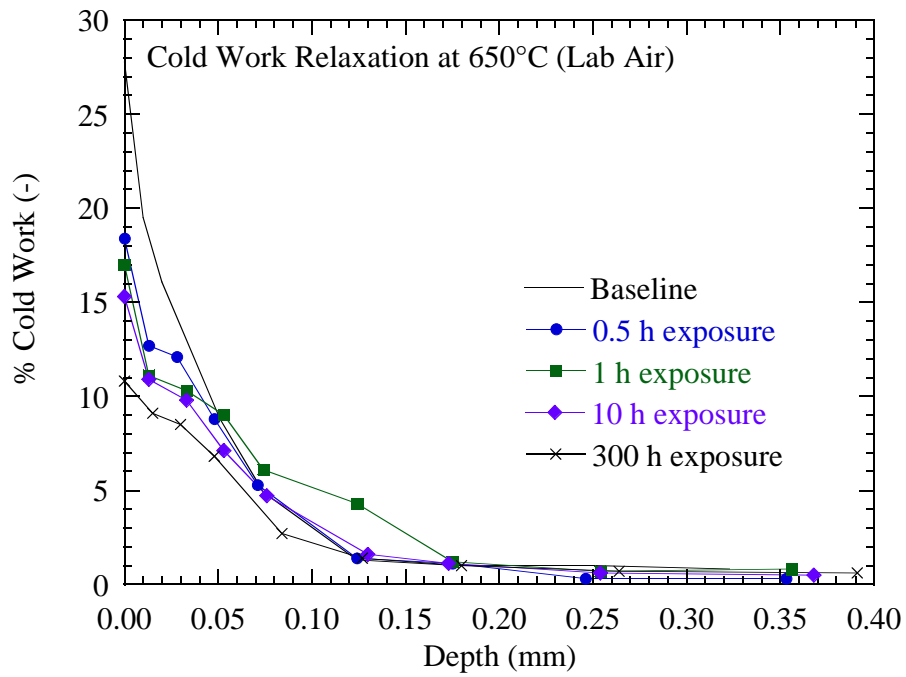


FIG. 8— Cold work distribution in IN100 versus exposure time at 650°C.

Figures 9 and 10 show the residual stress and cold work depth profiles, respectively for IN100 thermally exposed at 704°C for up to 300 hours. These results were collected on seven samples, all from plate (A2). A compressive surface residual stress of 200-450 MPa remained at the surface for all exposures. Stress relaxation at the free surface was similar in magnitude to the relaxation that occurred at the peak compressive stress. However, after 300 hours of exposure to 704°C residual stress retention is approximately 62%. The cold work profiles show a large change at the surface and to a depth of approximately 100 microns with increased exposure. There was a clear trend of decreasing cold work with increased exposure time that was also observed at 650°C. The maximum stress relaxation and reduction in cold work was observed at the surface of the specimen at both 650 and 704°C.

XRD of surface residual stress measurements have been proposed as a nondestructive method for characterizing the retained residual stresses in shot peened turbine engine components [24]. Figure 11 illustrates the difference in relaxation behavior of the surface versus the peak residual stress with exposure time at 704°C. The data plotted in Fig. 11 include the raw surface measurement, corrected surface and peak compressive residual stresses. The raw surface data is the as-measured surface value that represents the residual stress averaged to a depth of approximately 10 μ m. The corrected surface data is a computed value that can only be determined by making depth measurements and correcting the surface value based on the stress gradient into the depth. Finally, the peak compressive stress is the largest compressive residual stress in the depth. All three measures of residual stress were plotted versus exposure time. The raw and corrected surface residual measurements exhibited a rapid 450MPa change in compressive residual stress while the peak compressive residual stress changed only 225MPa with initial thermal exposure, approximately thirty minutes. Both the raw and corrected surface residual stress exhibit negligible change in the residual stress with increased exposure time after the initial change. However, the peak residual stress exhibited a continual reduction in compressive stress with increased exposure time. The raw surface residual stress overestimates the actual or corrected compressive residual stress on the surface for every exposure. Prev y [27] has reported that the error between the raw and corrected surface residual stress was typically maximum at the surface. Therefore any crack initiation predictions based on raw surface measurements will be nonconservative since they overestimate the actual compressive surface residual stress. In contrast, the raw surface residual stress measurement significantly underestimates the peak compressive residual stress in the depth. The peak compressive residual stress in the depth can retard crack growth and even stop small surface cracks from growing. In this case crack growth life predictions will be too conservative and the full benefit of residual stresses will not be incorporated into the life prediction. Clearly corrected and especially uncorrected (raw) surface residual stress measurements do not provide the capability for characterizing the relaxation of residual stress profiles, nor do they reflect the same relaxation behavior of the peak compressive residual stress. Hence, raw surface measurements alone are no substitute for characterizing residual stress relaxation of residual stress depth profiles.

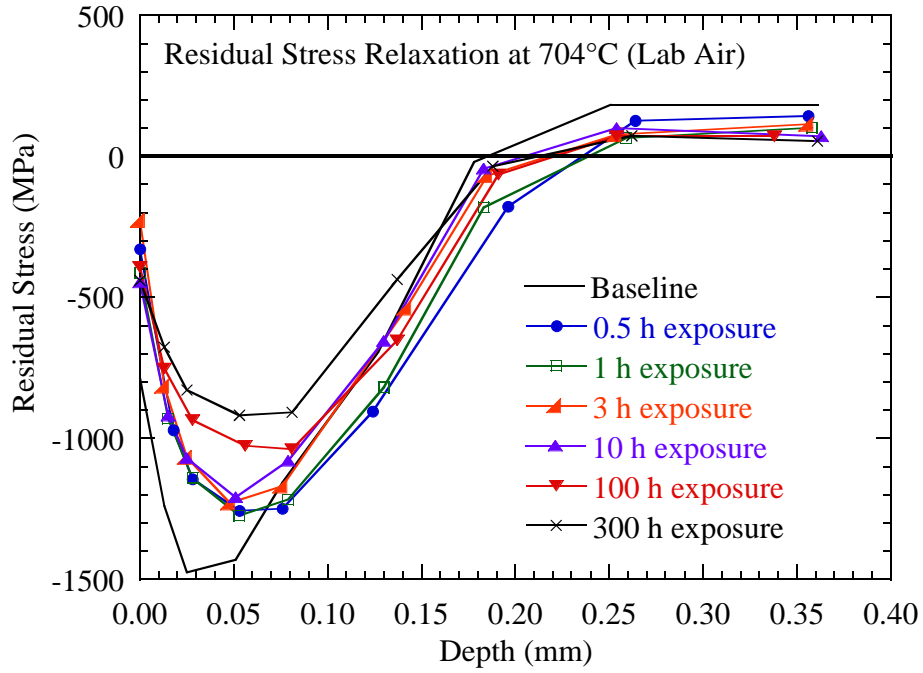


FIG. 9— Residual stress distribution in IN100 versus exposure time at 704°C.

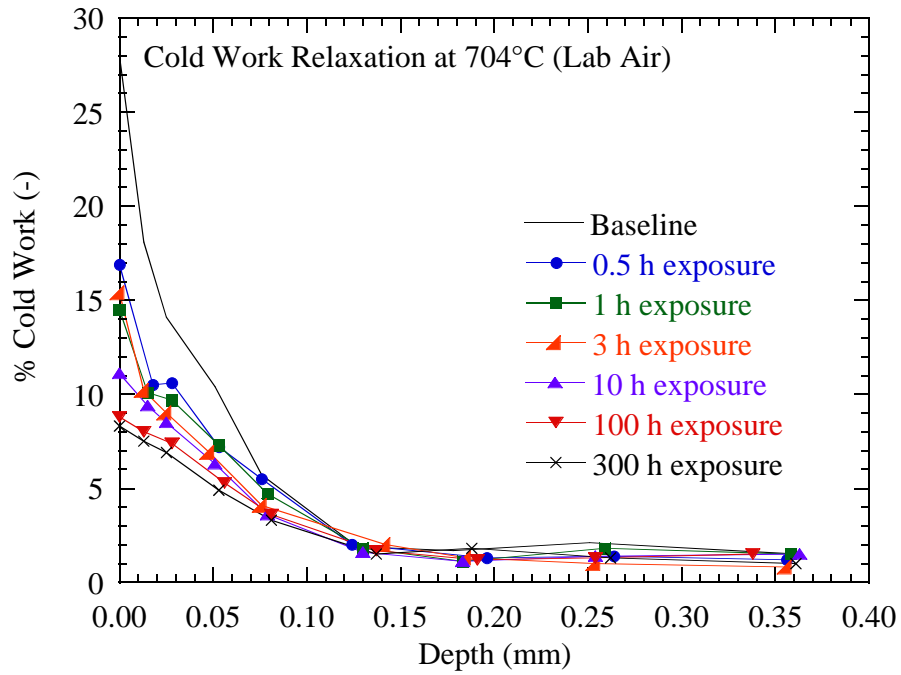


FIG. 10— Cold work distribution in IN100 versus exposure time at 704°C.

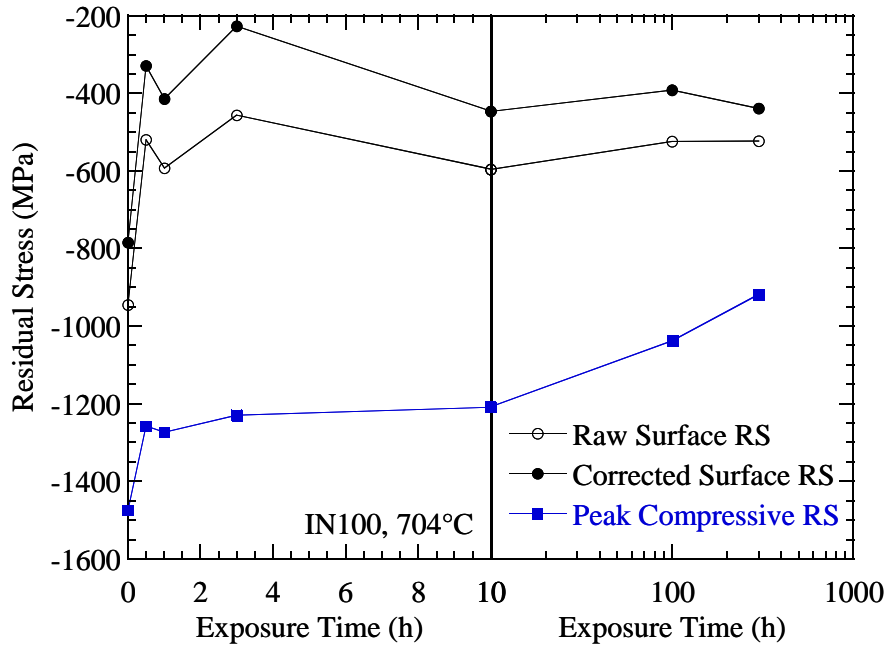


FIG. 11— *Surface and peak residual stress with increasing exposure time at temperature 704°C in IN100.*

Discussion

The thermal residual stress relaxation depth profiles exhibited an rapid decrease with initial exposure that decreased with time. The relaxation rates and residual stress and cold work profiles were stress and temperature dependent. Surface residual stresses stabilized quickly, approximately one hour, whereas interior stresses continued to relax with increased exposure time. The difference in stress relaxation behavior between raw or corrected surface stresses and interior stresses precludes surface measurements as a single method for characterizing residual stress relaxation in shot peened materials with a stress gradient into the depth. The overestimate of beneficial compressive residual surface stresses resulting from raw surface measurements clearly provides a nonconservative estimate of crack initiation resistance. More importantly, without subsurface measurements the degree of nonconservatism cannot be determined. Also, surface measurements provided no indication of stress relaxation behavior of compressive stresses in the interior that occurred with increased exposure time. Clearly, XRD surface residual stress measurements alone do not properly characterize residual stress relaxation behavior for the test conditions in this study.

This difference in measured surface and peak residual stress relaxation behavior indicates that a simple scalar representation of residual stress alone is probably not sufficient for accurate modeling of the relaxation behavior of the entire depth profile. Full tensor stress and plastic strain information would be required to accurately model the complex relaxation behavior. The change in microstructure and material properties from shot peening, as a function of temperature

and exposure time contribute to the complexity of characterizing residual stress relaxation behavior.

Conclusions

This experimental investigation characterized the thermal residual stress relaxation of IN100 superalloy. The shot peened samples were thermally exposed to two temperatures (650, 704°C) and a range of exposure times (0.5 – 300 hours). The residual stresses exhibited an initial rapid relaxation on the surface and in the depth at both temperatures. However, continued thermal exposure produced little or no change in surface residual stresses while peak compressive stresses in the depth continued to relax with exposure time. After 300 hours of exposure to 650 and 704°C residual stress retention is approximately 65 and 62%, respectively. Comparisons of residual stress relaxation on the surface and in the depth demonstrated the inability of surface measurements to adequately characterize the relaxation behavior of the subsurface residual stress profile. In general, raw surface residual stress measurements are not a reliable method of characterizing residual stress relaxation especially in the presence of subsurface stress gradients. Therefore, raw surface residual stress measurements alone should not be incorporated into a life prediction or life extension methodology to exploit the beneficial effects of residual stresses on retardation of fatigue crack initiation and propagation when thermal residual stress relaxation is present. However, the results from this study do show that there is significant potential for taking credit, even if only partial, for shot peen residual stresses in life management of components.

Acknowledgments

This research was conducted at the Materials and Manufacturing Directorate, Air Force Research Laboratory (AFRL/MLLMN), Wright-Patterson Air Force Base, OH 45433-7817 under onsite contract number F33615-98-C-5214. The authors gratefully acknowledge the support of Dr. Leo Christodoulou of the Defense Advanced Research Projects Agency (DARPA) under DARPA orders M359-00 and M978-00. The thermal exposures and x-ray analysis were conducted at Lambda Research Inc. of Cincinnati, OH under subcontract to the University of Dayton. The authors also acknowledge the SEM analysis of the shot peened samples by Dr. Kezhong Li and the finite element analysis by Dr. Steve Olson, both of the University of Dayton Research Institute.

References

- [1] Scott, J. A., "The influence of processing and metallurgical factors on fatigue," *Metal Fatigue: Theory and Design*, Ed. A. F. Madayag, John Wiley & Sons, Inc., New York, 1969.
- [2] Jilia, R., Renzhi, W., and Xiangbin, L., "Investigation of shot peening strengthening of René95 powder alloy," *Proceedings of the Sixth International Conference on Shot Peening*, San Francisco, CA, 1996, pp. 338-347.
- [3] Happ, M. B., Mourer, D. P., and Schmidt, R. L., "Residual stress analysis and LCF test results for peened bolt hole and dovetail configurations," *Proceedings of ASM's Conference on Residual Stress – In Design, Process and Materials Selection*, Ed. William B. Young, Cincinnati, OH, April 1987, pp. 127-136.

- [4] Akber, J. A., Kyriacou, S., and El-Zafrany, A. M., "Effect of shot peening on the fatigue life of axially loaded notched components," *Proceedings of the Fifth International Conference on Shot Peening*, Christ Church Oxford University, 1993, pp. 349-358.
- [5] Gray, H., Wagner, L., and Lütjering, G., "Influence of shot peening induced surface roughness, residual macrostresses and dislocation density on the elevated temperature HCF-properties of Ti alloy," *Proceedings of the Third International Conference on Shot Peening*, Eds. H. Wohlfahrt, R. Kopp and O. Vöhringer, Garmisch-Partenkirchen (FRG), 1987, pp. 447-457.
- [6] Fuchs, H. O., "Approximate analysis for optimizing prestress treatments," *Analytical and experimental methods for residual stress effects in fatigue*, ASTM STP 1004, Eds. R. L. Champoux, J. H. Underwood, and J. A. Kapps, American Society for Testing and Materials, Philadelphia, PA, 1988, pp. 13-20.
- [7] Kyriacou, S., "Shot-peening mechanics, a theoretical study," *Proceedings of the Sixth International Conference on Shot Peening*, San Francisco, CA, 1996, pp. 505-516.
- [8] Fathallah, R., Inglebert, G., and Castex, L., "Modelling of shot peening residual stresses and plastic deformation induced in metallic parts," *Proceedings of the Sixth International Conference on Shot Peening*, San Francisco, CA, 1996, pp. 464-473.
- [9] Wohlfahrt, H., "A model for predicting residual stresses produced by shot peening," *Proceedings of the European Conference on Residual Stresses*, Eds. E. Macherauch and V. Hauk, Translated from the German by Janet Mordike, Karlsruhe, 1983, pp. 347-364.
- [10] Hartman, G. A., Ashbaugh, N. E., and Buchanan, D. J., "A sampling of mechanical test automation methodologies used in a basic research laboratory," *Automation in fatigue and fracture: testing and analysis*, ASTM STP 1231, Ed. C. Amzallag, American Society for Testing and Materials, Philadelphia, PA, 1994, pp. 36-50.
- [11] Wusatowska-Sarnek, A. M., Blackburn, M. J., and Aindow, M., "Techniques for microstructural characterization of powder-processed nickel-based superalloys," *Material Science and Engineering A360*, 2003, pp. 390-395.
- [12] Wusatowska-Sarnek, A. M., Ghosh, G., Olson, G. B., Blackburn, M. J., and Aindow, M., "Characterization of the microstructure and phase equilibria calculations for the powder metallurgy superalloy IN100," *Journal of Materials Research*, Vol. 18, No. 11, Nov. 2003, pp. 2653-2663.
- [13] *Shot Peening Applications*, 8th edition, Metal Improvement Company, Inc., a subsidiary of Curtiss-Wright Corporation, Paramus, New Jersey.
- [14] Prevéy, P., Hornbach, D., and Mason, P., "Thermal residual stress relaxation and distortion in surface enhanced gas turbine engine components," *Proceedings of the 17th Heat Treating Society Conference and Exposition and the 1st International Induction Heat Treating Symposium*, Eds. D.L. Milam et.al., ASM Materials Park, OH, 1998, pp. 3-12.
- [15] Prevéy, P., "The effect of cold work on the thermal stability of residual compression in surface enhanced IN718," *Proceedings: 20th ASM Materials Solutions Conference & Exposition*, St. Louis, Missouri, October 10-12, 2000.
- [16] Moore, M. G., and Evans, W. P., "Mathematical correction for stress in removed layers in x-ray diffraction residual stress analysis," *SAE Transactions*, Vol. 66, 1958, pp. 340-345.
- [17] Vöhringer, O., "Relaxation of residual stresses," *Proceedings of the European Conference on Residual Stresses*, Eds. E. Macherauch and V. Hauk, Translated from the German by Janet Mordike, Karlsruhe, 1983, pp. 47-80.
- [18] Hoffman, J., Scholtes, B., Vöhringer, O., and Macherauch, E., "Thermal relaxation of shot peened residual stresses in the differently heat treated plain carbon steel Ck 45," *Proceedings of the Third International Conference on Shot Peening*, Eds. H. Wohlfahrt, R. Kopp and O. Vöhringer, Garmisch-Partenkirchen (FRG), 1987, pp. 239-247.
- [19] Schulze, V., Vöhringer, O., and Macherauch, E., "Thermal relaxation of shot peened residual stresses in a quenched and tempered steel 42 Cr Mo 4," *Proceedings of the Fifth International Conference on Shot Peening*, Christ Church Oxford University, 1993, pp. 265-274.
- [20] Cao, W., Khadhraoui, M., Brenier, B., Guédou, J. Y., and Castex, L., "Thermomechanical

- relaxation of residual stress in shot peened nickel base superalloy,” *Material Science and Technology*, Vol. 10, November 1994, pp. 947-954.
- [21] Khadhraoui, M., Cao, W., Brenier, B., Castex, L., and Guédou, J. Y., “Experimental investigation and modeling of relaxation behavior of shot peening residual stresses at high temperature for nickel base superalloys,” *Material Science and Technology*, Vol. 13, April 1997, pp. 360-367.
- [22] Ahmad, J., Chandu, S., Kroupa, J., and Prevéy, P., “An assessment of residual stresses induced by surface treatments,” *Proceedings of the 6th National Turbine Engine High Cycle Fatigue Conference, HCF 2001*, Jacksonville, FL., March 2001.
- [23] Prevéy, P., “The measurement of subsurface residual stress and cold work distributions in nickel base alloys,” *Proceedings of ASM’s Conference on Residual Stress – In Design, Process and Materials Selection*, Ed. William B. Young, Cincinnati, OH, April 1987, pp. 11-19.
- [24] Vukelich, S., Berkley, S., Russ, S., and Bradley, E. F., “Residual stress measurement and its application to achieve predicted full life potential of low cycle fatigue (LCF) engine disks,” *The 9th International Symposium on Transport Phenomena and Dynamics of Rotating Machinery*, Honolulu, Hawaii, February 2002.
- [25] Standard Test Method for Verifying the Alignment of X-Ray Diffraction Instrumentation of Residual Stress Measurement, E915-96, Vol. 03.01.
- [26] Standard Test Method for Determining the Effective Elastic Parameter X-Ray Diffraction Measurements of Residual Stress, E1426-98, Vol. 03.01.
- [27] Prevéy, P., “X-ray diffraction residual stress techniques,” *Metals Handbook*, Metals Park: American Society for Metals, 1986, pp. 380-392.

Effect of Dissimilar Metals on Fretting Fatigue Behavior of Ti-6Al-4V

Alisha Hutson*, Hyukjae Lee[†] and Shankar Mall[†]

Air Force Research Laboratory, Mechanical Behavior and Life Prediction Section (AFRL/MLLMN)

**Advanced Materials Characterization Group, Structural Integrity Division
University of Dayton Research Institute, Dayton, OH 45469-0128, USA.*

[†]Department of Aeronautics & Astronautics, Air Force Institute of Technology (AFIT/ENY), Building 640, 2950 P. Street, Wright-Patterson Air Force Base, OH 45433-7765, USA.

ABSTRACT

An investigation was conducted to explore the fretting fatigue behavior of Ti-6Al-4V specimens in contact with pads of varying surface composition. Three conditions were selected to provide a range of compositions and hardnesses: Ti-6Al-4V (low-stress ground and polished to RMS #8), two comparable aluminum alloys and two comparable nickel alloys. A fourth condition (Ti-6Al-4V, grit blasted to RMS #64 and stress relieved) was selected to interrogate the effect of surface roughness. Behavior against the four pad conditions was evaluated with step testing and S-N fatigue testing using two contact pad geometries (cylinder-on-flat and flat-on-flat with a blending radius) in two independent fretting fatigue fixtures. Laboratory experiments were conducted at different applied stress levels and contact forces. Average applied clamping stresses for the flat-on-flat contact were set at ~200 MPa and ~650 MPa. Applied contact forces for the cylinder-on-flat contact were selected to provide two Hertzian peak pressures of 292 and 441 MPa. The coefficient of friction, μ , was quantified to help identify possible crack nucleation mechanisms and the contact pad surfaces were characterized through hardness and composition evaluation, and surface profile measurements. Finite element analyses of the two fretting fixtures were conducted to assess variability in relative slip and local stress state for each pad material.

1. Introduction

Fretting fatigue, a type of damage occurring in contacts subject to small relative motions and leading to premature crack initiation and failure, has been the focus of numerous investigations over the years [1-4]. Because it has been identified in a wide range of hardware configurations and service components, a variety of testing devices have been developed to study its different aspects. However, little or no standardization exists to either guide the development of test systems or to allow comparison of test results between the various existing test systems.

This fact has lead the authors to the focus of the current study, which involves in part, comparing the results of two fretting fatigue studies that were conducted in parallel with similar goals, but were executed using two different test systems. The studies were intended to investigate the effects of dissimilar metals on fretting fatigue behavior and compare the results to a baseline condition of like metals in contact under the same nominal conditions. In each study, normal loads were varied, stress fields were calculated using a finite element approach, and the resultant damage was characterized using scanning electron microscopy and spectral analysis.

For the purposes of this investigation, the results from each of the prior studies are discussed with a focus on the observed trends. Details of the testing from both studies are presented, including

evaluation of the coefficient of friction, μ , for each material pair. Finite element analysis results are presented. Then similarities between results from the two studies are presented.

2. Experiments

Material Specifications

Specimens were taken from forged Ti-6Al-4V plates used throughout the High Cycle Fatigue program. The processing details are reviewed in previous work [5,6]. Fretting pads were manufactured from one of three materials: the Ti-6Al-4V used in the specimen manufacture, an aluminum alloy or a nickel-base superalloy. Specific materials differed somewhat between the two investigations, but in general, pad materials were selected to provide a sampling of the properties found in structural metals. The material properties for the different pad materials are shown in Table 1. All tests were conducted under ambient lab conditions.

Table 1: Material Properties

	AFRL Materials		AFIT Materials		Common Materials
	7075-T6 Al	IN 100 (supersolvus)	2024-T3 Al	Inconel 718	Ti-6Al-4V
E (GPa)	71.7	200	72.4	200	120
ν	0.33	0.312	0.3	0.3	0.3

Experimental Apparatus: AFIT

The AFIT fretting fatigue fixture uses a cylinder-on-flat contact configuration. The pads are applied to either side of a dogbone specimen, using a fretting fixture attached to a servo-hydraulic machine (see Fig. 1). In this arrangement, an axial stress, σ_{axial} , and a shear force, Q , may be applied to the specimen while keeping the contact force, P , constant. Applied axial and tangential loads are measured using a load cell in the top grip and a pressure transducer in the bottom grip. The contact force is applied through lateral springs and measured by pressure gauges on both sides of the specimen. A careful pad alignment is performed prior to each test to ensure uniform contact.

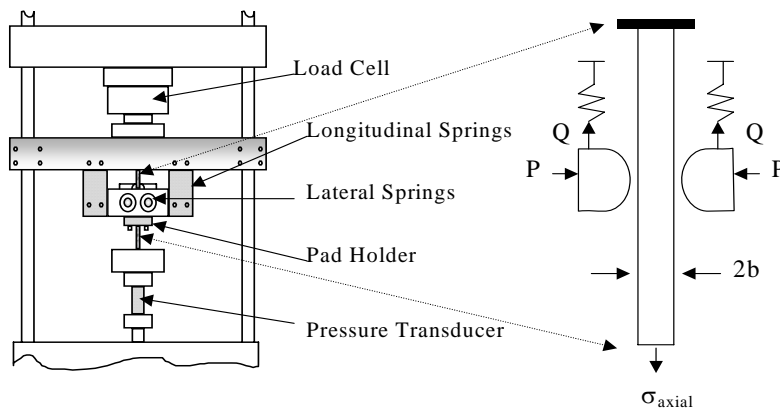


Fig. 1. AFIT fretting fatigue apparatus.

Fretting fatigue tests were conducted at two normal stress conditions corresponding to ~ 292 MPa or ~ 441 MPa peak Hertzian pressure for the 2''-radius pads. Contact forces selected to achieve one of these two peak pressures are different for each pad material. To achieve the lower peak pressure, 1757 N was used with the 2024 Al pads, 1063 N was used with the Inconel 718 pads and 1335 N was used with the Ti-6Al-4V pads. To achieve the

higher peak pressure, 4000 N was used for the aluminum pads and 2425 N was used for the Inconel 718 pads. A test frequency of 200 Hz was used with the lower contact forces; 50 Hz was used with the higher contact forces. Maximum axial stresses, σ_{axial} , ranged from 400 to 700 MPa, and stress

ratios, R , ranged from 0 to 0.7. Data are presented in the form of an effective stress, calculated using the Walker method [7], which is expressed as:

$$\sigma_{\text{eff}} = \sigma_{\text{axial,max}} (1-R)^m$$

Where σ_{eff} is the effective stress on the specimen to account for stress ratio effects, $\sigma_{\text{axial,max}}$ is the maximum applied stress on the specimen, R is the stress ratio, and m is a fitting parameter, previously determined to be 0.45 [8]. Coefficients of friction, μ , may also be calculated for each test from the Q/P values determined for each cycle or data acquisition interval. Gross sliding occurs during the first few cycles of each test, and for these cycles, Q/P corresponds directly to μ . After a few thousand cycles, μ reaches a steady state value, which was evaluated for the experiments presented here and was used in the finite element analyses to be discussed later.

Experimental Apparatus: AFRL

The AFRL fretting fatigue fixture uses a flat-on-flat contact configuration with blending radii at the edges of contact. Normal and shear loads are applied to the specimen using instrumented bolts, as shown in Fig. 2. Axial loads are applied to the specimen using an electromagnetic shaker system. The test geometry differs from conventional fretting fatigue tests [1,2] in two fundamental ways. First, the axial stress is transferred entirely to the fixture through shear, thus restricting the maximum nominal shear stress to that which can be reached for a given nominal clamping stress before total slip occurs. Resulting stresses in the specimen are zero on one end of the pad, so the shear force into the pad is determined from the load applied to the specimen. Second, symmetry of the apparatus provides a specimen which breaks on one end, leaving the other end with a fretting scar and damage obtained under nominally identical conditions. As with a conventional fretting fatigue apparatus, the clamping force is constant and only the axial and shear loads are oscillatory.

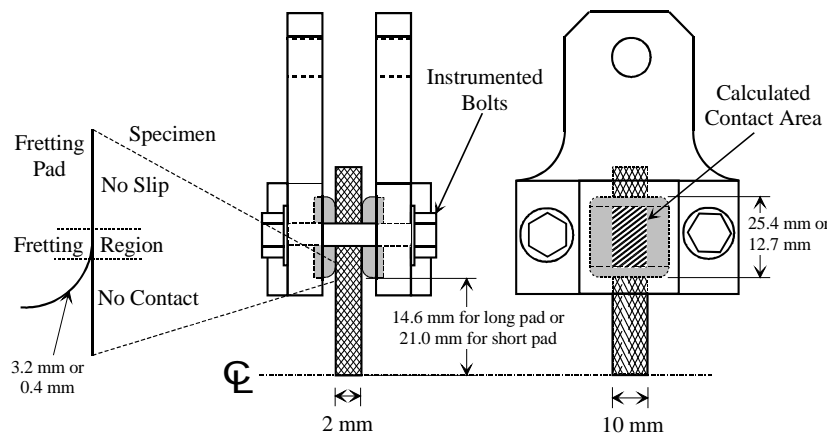


Fig. 2. AFRL fretting fatigue apparatus.

Two clamping stresses (~240 MPa and ~650 MPa) were selected for the experiments with the IN 100 and aluminum pads, and were produced by varying pad length and clamping force. The pad lengths used were 12.7 mm and 25.4 mm. When combined with a 3.175 mm blending radius, the resulting contact lengths were 6.35 mm and 19.05 mm. These pad geometries were used in tests with the Ti-6Al-4V pads to produce a broad range of clamping stresses,

including 240 and 650 MPa. Unlike the Hertzian contact, the stresses were calculated for the flat-on-flat configuration using a simple load-divided-by-area calculation, so the same normal loads were used for all pad materials at a given clamping stress condition. All fretting fatigue tests for this study were performed at 300 Hz at $R = 0.5$.

Three types of tests were performed using the AFRL apparatus: step tests, S-N tests, and μ tests. The step tests provide an experimental determination of the fretting fatigue limit stress for a 10^7 cycle fatigue life. These results are presented with results from classical S-N tests. The fretting

fatigue tests for this geometry could not be used to make a direct determination of μ , however, μ can be evaluated if gross sliding is allowed to occur. This technique was to evaluate μ for the flat-on-flat configuration by applying the desired clamping stress and then subjecting the specimen to a stroke controlled tension test. The resulting stroke vs. load curve was then used to identify the axial load corresponding to the onset of sliding, and a Q/P calculation was performed.

3. Analysis

Analyses of both experimental fixtures were conducted to determine the states of stress for each material combination of interest. In both the AFIT and AFRL models ABAQUS was used as the analysis package. Quasi-static linear elastic behavior under plane stress was assumed and the meshes in the regions of highest expected peak stresses were refined to $\sim 6 \mu\text{m}$. Details of the finite element methods are presented in [9,10] for the AFRL system and the AFIT system, respectively.

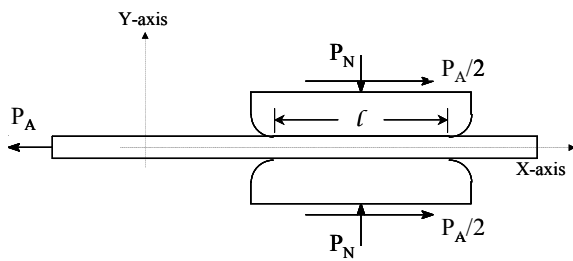


Fig. 3. AFRL finite element geometry.

The clamping stress was applied by imposing the desired force on the back of the pad, which resulted in a uniform displacement of the pad. A similar technique was used to impose the axial stress on the specimen. Axial and clamping load conditions were selected based on experimental observations. Contact was defined for the entire top region of the specimen and the pad bottom including the full radius. The material was modeled as a Ti-6Al-4V specimen against a pad of one of the three materials used in the experiments. Only the first half of the initial fatigue cycle was

modeled, and μ was taken as 0.3. The specimen was modeled as 2 mm thick by 10 mm wide. Clamping loads on the pads were 41.275 kN ($\sigma_N = 650 \text{ MPa}$), which corresponds to the conditions used for the short pad.

Analyses for the long pad are given in [10].

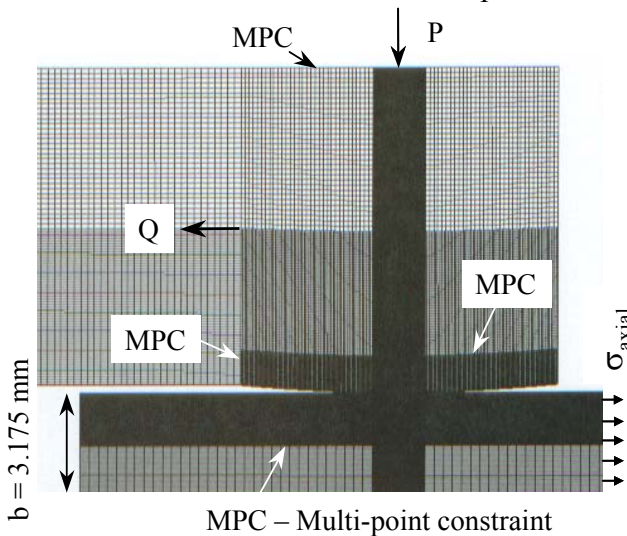


Fig. 4. AFIT finite element model geometry.

MPC was also defined wherever elements of dissimilar size were placed adjacent to each other, to prevent smaller

The fretting pad was constrained in the x-direction and prevented from rotating by defining a MPC (Multi Point Constraint) along the top of the pad. The specimen was constrained in the x and y-directions through boundary conditions defined along the left and bottom of the specimen, respectively. MPC was also

defined wherever elements of dissimilar size were placed adjacent to each other, to prevent smaller

Model	Pad Material	Clamping Load (N)	Clamping Stress (MPa)	Specimen Axial Stress (MPa)	COF
AFRL	Ti-6Al-4V	41,275	620	250	0.3
AFRL	IN 100	41,275	620	330	0.3
AFRL	7075-T6 Al	41,275	620	256	0.3
AFIT	Ti-6Al-4V	1335	292	538	0.3
AFIT	Inconel 718	1064	292	610	0.5
AFIT	Inconel 718	2425	441	538	0.5
AFIT	2024-T3 Al	4000	441	538	0.35

elements from penetrating larger ones. Additional details on the FEA can be found in [11].

Loads were applied in this model in the following sequence. First, the normal load, P , was applied. Then the maximum tangential load, Q_{max} , and the maximum axial stress, $\sigma_{axial,max}$, was imposed, followed by the minimum tangential load, Q_{min} , and the minimum axial stress, $\sigma_{axial,min}$. The loading conditions used were those

identified during the experimental portion of the study and are listed in Table 2. The value of μ defined at the contact interface was also determined experimentally, for which the procedure is discussed in reference [8]. 0.5 was used for the Inconel 718 pads; 0.35 was used for the 2024 Al pads. These values correspond to the stabilized values first observed after ~ 1500 fretting fatigue cycles.

4. Experimental Results

Results from the AFRL test system are shown in Figs. 5 and 6. In Fig. 5 the results from the initial AFRL work are shown [12]. The fretting fatigue limit stresses (σ_{FF}) for a 10^7 cycle fatigue life are plotted as a function of average applied clamping stress. Only specimens tested against IN

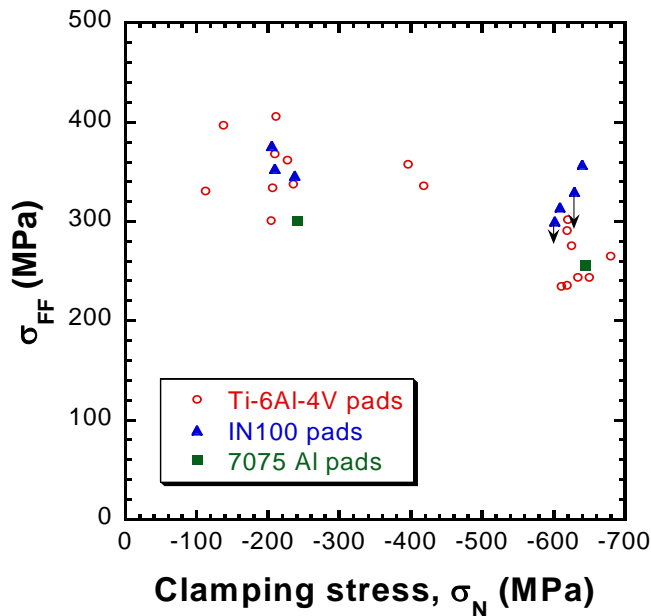


Fig. 5. AFRL results – fretting fatigue strength, σ_{FF} for a 10^7 cycle fatigue life versus applied clamping stress, σ_N .

100 pads indicate a benefit from contact with dissimilar material, and then, only at the higher clamping stress condition. Surface roughness analysis from that earlier work indicated a possible correlation with initial pad roughness, but that mechanism should also work at the lower clamping stresses. No clear trend was noted when considering the results in light of the m values determined experimentally for the three material pairs (Ti-on-Ti = 0.5 to 0.7, Ni-on-Ti = 0.63, Al-on-Ti = 0.32). A lower coefficient of friction should improve the fretting fatigue behavior by lowering the local stresses [10].

The results shown in Fig. 6 are limited to the higher clamping stress, and are shown in S-N form, with the maximum axial stress, σ_{axial} , on the abscissa. New S-N data are included. The data that fall on the line at 10^7 cycles correspond

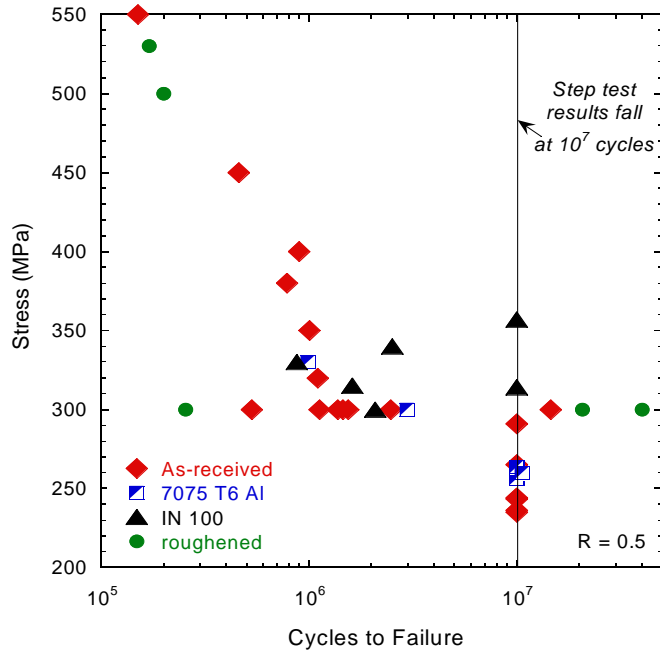


Fig. 6. AFRL results – maximum axial stress versus cycles to failure.

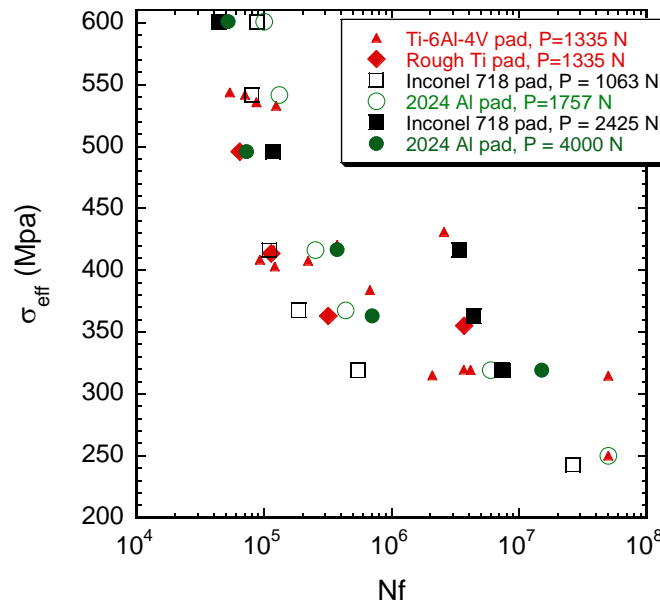


Fig. 7. AFIT results – effective stress versus fatigue life.

fretting fatigue and fretting wear mechanisms were the same, and so the effect of certain variables, like contact material, would also be the same. That theory does not seem valid in light of the results documented in both the AFRL and AFIT studies.

5. Analytical Results

Analytical results for the AFRL system are shown in Figs. 8-10. In these figures, the loaded end of the specimen is to the left of the chart while the right end of the specimen is stress free

to the fatigue limit stresses calculated for those tests. Again, the fretting fatigue behavior of specimens tested against IN 100 pads seems a bit better than those tested against other pad materials. Further tests were conducted with roughened pads, for comparison. The three points at 300 MPa σ_{axial} (included from [13]) indicate a moderate improvement in fretting fatigue behavior. The new tests conducted for this study, at 500 and 530 MPa σ_{axial} did not produce measurably longer fretting fatigue lives than the as-received condition.

Results for the AFIT experiments are shown in Fig. 7, where the results are shown in terms of an effective stress, σ_{eff} , discussed earlier. Data are shown for roughened and as-received Ti-6Al-4V pads as well as for the Inconel 718 and 2024 Al pads with two peak Hertzian stresses (292 or 441 MPa). This data, except for that obtained for the rough Ti-6Al-4V pads, was taken from reference [14]. No clear trend with contact material is observed, except with the Inconel 718 pads where a slight improvement was observed for lower effective stresses. A distinct step in the fatigue lives is present between $\sigma_{eff} = 420$ and 480 MPa for the higher peak Hertzian stress condition. All remaining data fall within the scatter expected for the Ti-on-Ti condition.

These findings are significant in light of the conventional wisdom that fretting fatigue behavior is quite sensitive to contact material. This opinion originated from investigations on fretting wear, in which the tribological properties of the contact radically affected the wear behavior of the contact pair. It has long been assumed that

outside the right edge of contact.

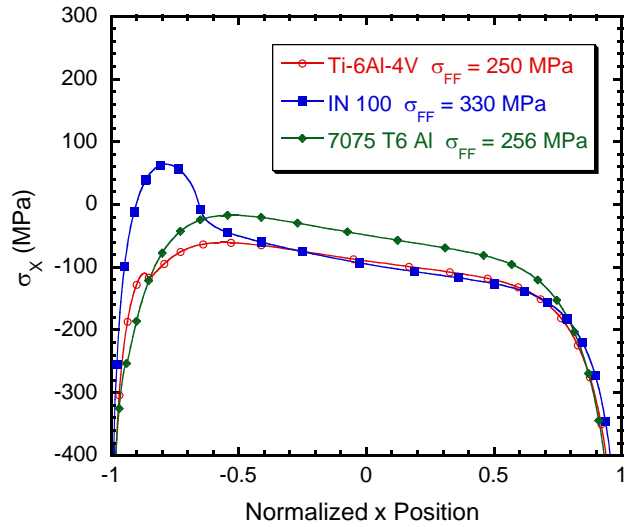


Fig. 8. AFRL – x-component stress distribution under contact pad.

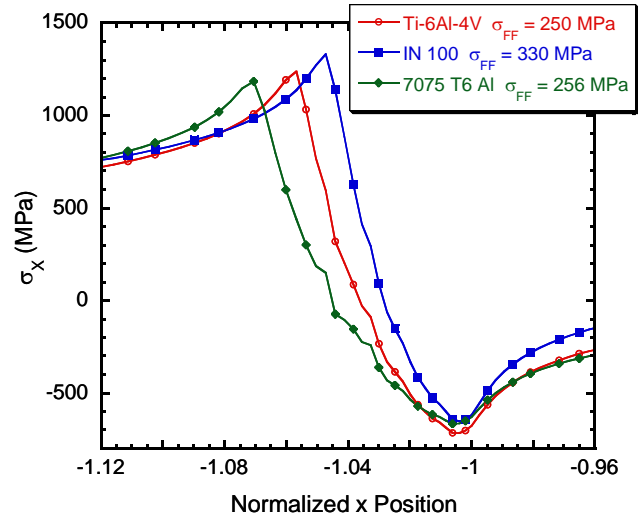


Fig. 9. AFRL – x-component stress concentrations at EOC.

The σ_x stress distributions along the length of the pad for the three pad materials are shown in Fig. 8, where x is normalized with respect to the half-length of the pad between the center and the position of undeformed contact (UEC). The stress concentrations at the edges of contact are included in Fig. 9. In prior work, τ_{xy} and σ_y stresses distributions were very similar. Significant differences in stress distribution were observed only for the σ_x stress, so the τ_{xy} and σ_y stresses are not discussed here. The σ_x stresses are dominated by the applied clamping stress, and all fall below zero, except for a small portion of the curve for the IN 100 pad model.

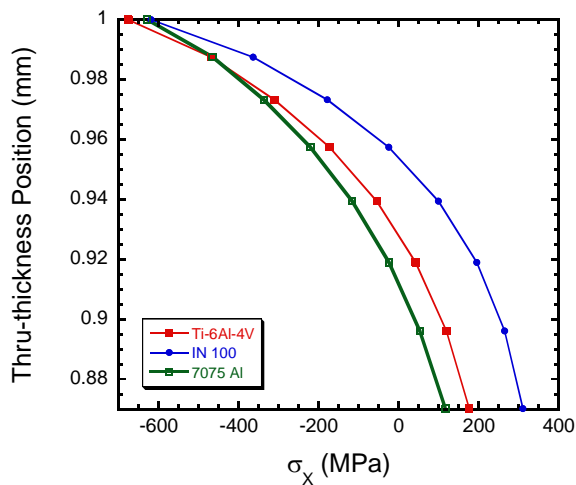


Fig. 10. AFRL – x-component stress distribution into specimen thickness. 1 corresponds to the specimen surface.

the contact geometry under investigation. It stands to reason that the gradients into the specimen thickness will be localized in the same manner. Representative σ_x curves are shown in Fig. 10 for the three models that have been discussed. In this figure, the coordinate $y=1$ corresponds to the surface of the specimen in contact with the pad and lower numbers correspond to locations within

The edge of contact (EOC) stresses for the three different short pad models are shown in Fig. 7. For the EOC plot (Fig. 9), -1 corresponds to the left EOC and is the same location as -1 in Fig. 8. Here, the magnitudes of the stress peaks are slightly different and the exact location of the peaks differs slightly due to the differing material moduli. However, the general shape of the stress distribution is the same and shows that peak stresses are very localized near the EOC. The exact location of the peak seems to be a function of material modulus and/or applied axial stress.

The stress gradient along the contact length was shown in Fig. 9 to be very steep for

the specimen thickness. Data for each curve was taken at the model UEC location at the loaded end of

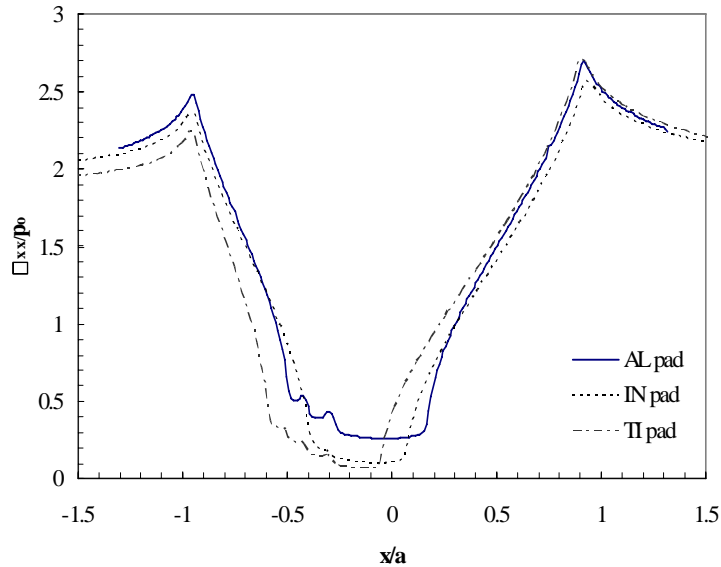


Fig. 11. AFIT – x-component stress distributions for the three pad materials.

the specimen. The stress profiles show that the σ_x stresses decay rapidly, with stresses at 100 μm below the surface ($y=0.9$) being almost the same as those much deeper. Thus, stress gradients into the thickness are of the same order of magnitude as those along the surface.

Analytical results for the AFIT system are shown in Figs. 11-12. In these figures, the loaded end of the specimen is to the right of the chart. The x-component stress curves, shown in Fig. 11, are normalized with the corresponding value of peak Hertzian stress. The x-axis values are normalized with the theoretical half contact width, a , so that values of $x/a < -1$ or > 1 correspond to locations on the specimen

not in contact with the pad. The overall shape of the three curves is similar, with the only differences being attributed to differences in the material moduli or the applied loads.

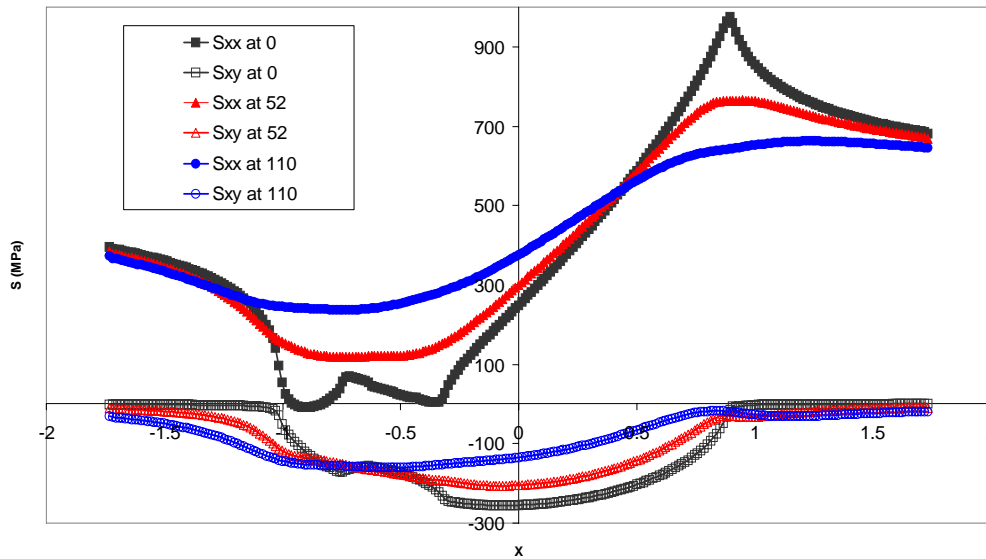


Fig. 12. AFIT – x-component and shear stresses for different locations within a specimen in contact with a Ti-6Al-4V pad. 0 coincides with the specimen surface, 52 indicates 52 μm below the specimen surface, and 110 indicates 110 μm below the specimen surface.

Fig. 12 shows σ_{xx} and τ_{xy} data for an AFIT model featuring a Ti-6Al-4V pad. Three pairs of curves are shown, each representing three locations in the specimen, 0 (specimen surface), 52 (52 μm below the specimen surface) and 110 (110 μm below the specimen surface). The stress peaks decay rapidly from ~ 975 MPa (σ_{xx}) to ~ 600 MPa within 110 mm of the specimen's surface.

These gradients are similar to those in the AFRL fixture in spite of radical differences in contact geometry. Both geometries produce σ_{xx} stress peaks that decay within ~ 100 μm of the specimen surface.

6. Characterization Results

Scanning Electron Microscopy (SEM) and spectral analysis (EDS) were used to evaluate the fretting scars after testing. The SEM was used to evaluate fretting debris, and to identify cracks on the unfractured end of AFRL specimens. Representative micrographs for the AFRL specimens are shown in Figs. 13 – 15, which include fretting scars in the region of fretting crack nucleation for specimens tested against Ti-6Al-4V, aluminum and IN 100 pads, respectively. Each of the specimens shown was subjected to a clamping stress of approximately 650 MPa. The aluminum pads (Fig. 14) left less debris on the specimen than the IN 100 or Ti-6Al-4V pads (Figs. 13 and 15), possibly due to the lower μ value for Al (0.32 for Al, compared to ~ 0.6 for Ti and 0.63 for IN 100). Also, numerical analyses of the test fixture designed to calculate local stress distributions indicated higher values of relative slip and slip length at the edge of contact for the IN 100 pads [13]. This mechanism explains the volume of debris produced with the IN100 pads, while adhesion and delamination mechanisms would account for the wear debris from the Ti pads.

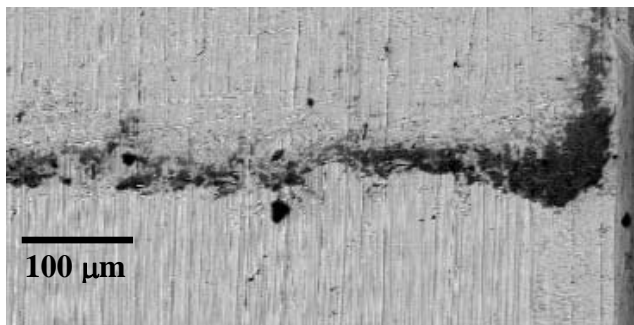


Fig. 13. Fretting scar from an AFRL specimen tested at 250 MPa axial stress (R=0.5) using Ti-6Al-4V pads.

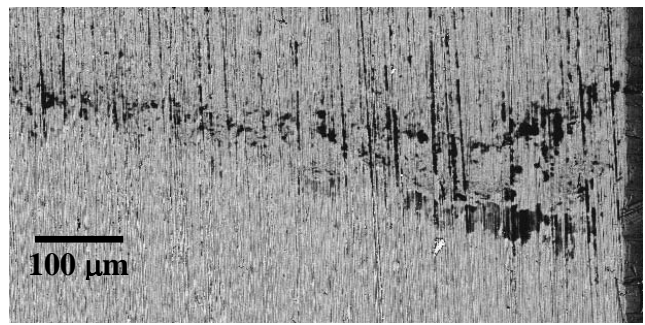


Fig. 14. Fretting scar from an AFRL specimen tested at 256 MPa axial stress (R=0.5) using 7075 Al pads.

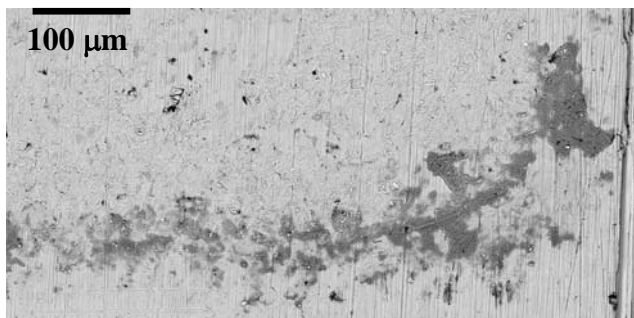


Fig. 15. Fretting scar from an AFRL specimen tested at 300 MPa axial stress (R=0.5) using IN 100 pads.

Similar trends were observed on the AFIT specimens. Micrographs of two specimens are shown in Figs. 16 and 17, for tests conducted under similar conditions against Inconel 718 and 2024 Al pads, respectively. The fretting scar dimensions are shown on these unfractured specimens, and as expected, the scar from the Al pad is larger because of the lower material modulus. Also, more debris was observed on the contact with the Inconel pad. As with the AFRL results, μ was higher for Inconel (0.5) than for 2024 Al (0.35) on Titanium.

Higher volumes of wear debris were also observed for lower peak Hertzian stress values. As seen in Fig. 18 through 21, the higher Hertzian stress resulted in considerably less wear debris. Specimens tested against lower peak stresses are shown in Figs. 19 and 21, and indicate considerably more wear debris than Figs. 18 and 20. (Note: asymmetrical scar in Fig. 18 is an artifact of specimen pullout after fracture, not from misalignment of the pads and specimen.)

Elemental content of the as-received specimen surfaces and post-test fretting debris was characterized using Energy Dispersive technique. For the Ti-6Al-4V pads, oxidation of the alloying elements took place during the generation of debris products, as noted by increased oxygen levels compared to unfretted material. For both test systems, aluminum was transferred to the specimen surface and oxidized debris products were created in the aluminum on Ti-6Al-4V contact. Trace

amounts of titanium were noted on the aluminum pad, probably due to an alumina particle wearing at the titanium surface.

The most significant differences to note are in the IN 100 on Ti-6Al-4V contact. For this material pair, relatively large amounts of debris were observed suggesting the possibility of higher EOC temperatures. Analysis of debris on specimens from both the AFRL and AFIT systems, which indicated a marked increase in oxygen was noted in the debris, would support such a conclusion.

Since oxygen is relatively small, large amounts are required to produce sizeable peaks. Also, significant amounts of nickel, chromium and cobalt were identified in the debris on the specimen, indicating material transfer from the pad to the specimen. The authors suggest this transfer of material was caused by TiO_2 produced by fretting wear mechanisms. The dominance of such

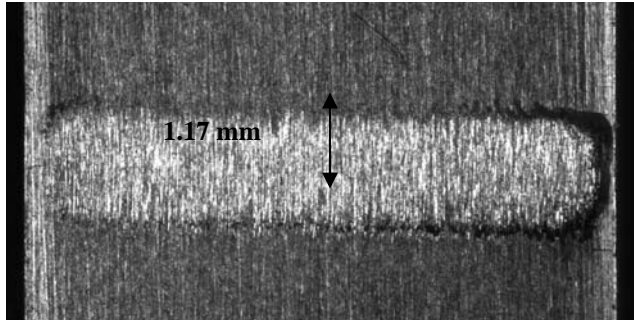


Fig. 16. AFIT specimen fretting scar – Inconel 718 pad, $\sigma_{eff} = 363$ MPa, $P = 2425$ N

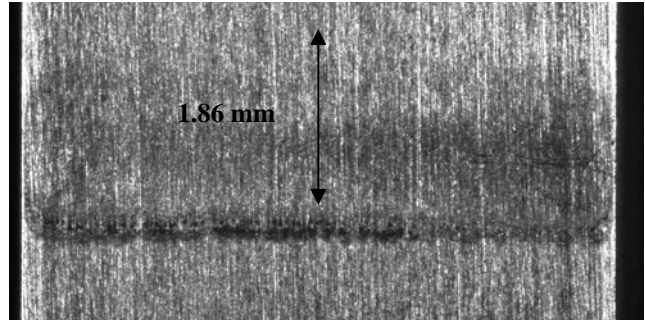


Fig. 17. AFIT specimen fretting scar – 2024 Al pad, $\sigma_{eff} = 363$ MPa, $P = 4000$ N

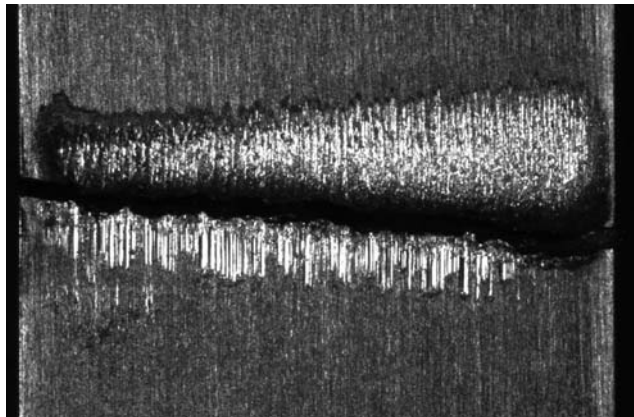


Fig. 18. AFIT specimen fretting scar – Inconel 718 pad, $\sigma_{eff} = 601$ MPa, $P = 2425$ N

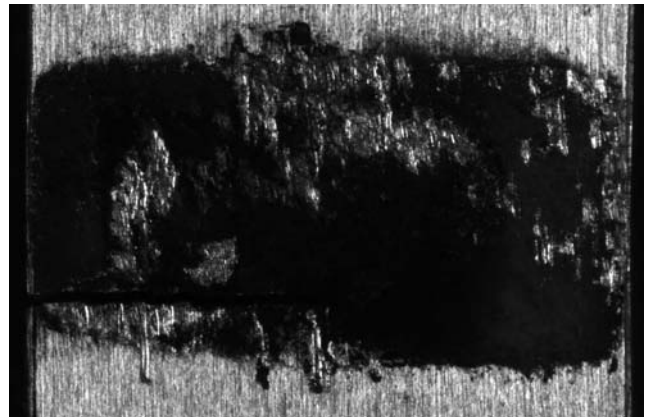


Fig. 19. AFIT specimen fretting scar – Inconel 718 pad, $\sigma_{eff} = 601$ MPa, $P = 1063$ N

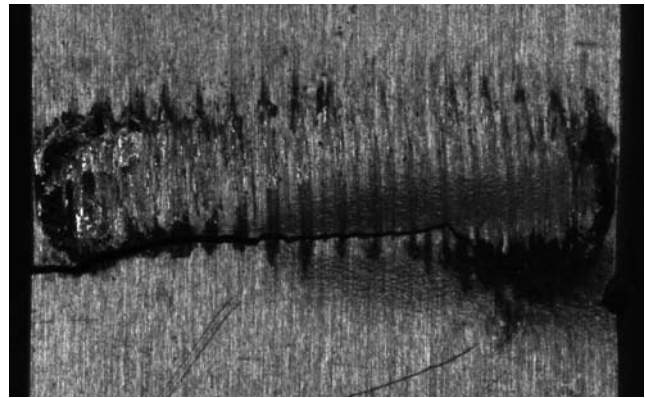
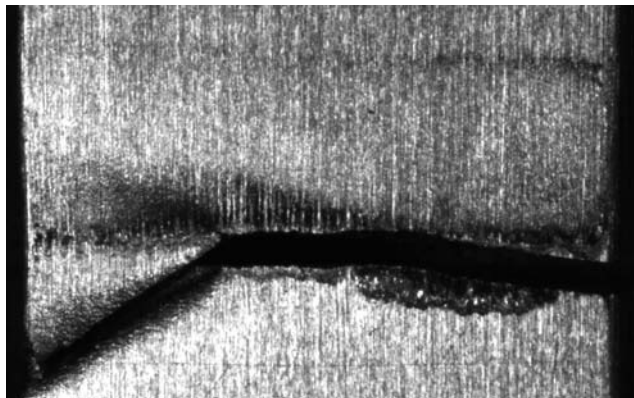


Fig. 20. AFIT specimen fretting scar – 2024 Al pad, $\sigma_{\text{eff}} = 495$ MPa, $P = 4000$ N Fig. 21. AFIT specimen fretting scar – 2024 Al pad, $\sigma_{\text{eff}} = 417$ MPa, $P = 1757$ N

mechanisms can improve fretting fatigue behavior by wearing away small cracks before they have a chance to propagate, and might better explain why the IN 100 pads produced improved fretting fatigue behavior in the Ti-6Al-4V specimens, but only for the higher clamping stress condition.

7. Conclusions

1. The same general trends were observed in both fretting fatigue test systems.
2. Fretting fatigue behavior of Ti-6Al-4V is relatively insensitive to the contact pad material, as indicated by both experimental & analytical results.
3. A slight improvement in fretting fatigue behavior was observed with IN 100 or Inconel 718 pads under certain conditions. The mechanisms for improvement is not clear, but it may be related to the dominance of wear mechanisms present at the higher clamping stress condition coupled with higher roughness of the pad surface.
4. Material transfer between the pad and specimen is dependent on the material properties. Transfer of the softer material to the harder one generally occurs, but some abrasive particles (TiO_2 or Al_2O_3) may be generated due to oxidation.

References

- 1) *Fretting Fatigue, ESIS 18*, R.B. Waterhouse and T.C. Lindley, Eds., Mechanical Engineering Publications, London, 1994, pp. 171-182.
- 2) *Standardization of Fretting Fatigue Test Methods and Equipment, ASTM STP 1159*, M. H. Attia, and R. B. Waterhouse, Eds., American Society for Testing and Materials, Philadelphia, 1992.
- 3) *Fretting Fatigue Current Technologies and Practices, ASTM STP 1367*, D.W. Hoepfner, V. Chandrasekaran, and C.B. Elliot, Eds., American Society for Testing and Materials, West Conshohocken, PA, 2000.
- 4) *Fretting Fatigue: Advances in the Basic Understanding and Applications, ASTM STP 1425*, S.E. Kinyon, D.W. Hoepfner, Y. Mutoh, Eds., American Society for Testing and Materials, West Conshohocken, PA, 2003.
- 5) Peters, J.O. and Ritchie, R. O., *Int. J. Fatigue*, 23, 2001, pp. S413-S421.
- 6) Moshier, M.A., Nicholas, T. and Hillberry, B.M., *Int. J. Fatigue*, 23, 2001, pp. S253-S258.
- 7) Walker, K., *Effects of Environment and complex load history on fatigue life, ASTM STP 462*, Philadelphia, PA, American Society for Testing and Materials, 1970.
- 8) Lykins, C.D., Mall, S. and Jain, V.K., *Int. J. Fatigue*, 22, pp. 703-16, 2000.
- 9) Hutson, A.L., "Fretting Fatigue of Ti-6Al-4V Under Flat-on-Flat Contact with Blending Radii," M.S. Thesis, School of Engineering, University of Dayton, Dayton, OH, August, 2000.
- 10) Hutson, A.L., Nicholas, T., Olson, S.E., and Ashbaugh, N.E., *Int. J. Fatigue*, 23, 2001, pp. S445-S453.
- 11) Tsai, T.C. and Mall, S., *Finite Element Anal. Des.*, 36, pp171-87, 2000.
- 12) Nicholas, T., Hutson, A.L., Olson, S. and Ashbaugh, N., *Advances in Fracture Research, Proceedings of ICF-10*, K. Ravi-Chandar, B.L. Karihaloo, T. Kishi, R.O. Ritchie, A.T. Yokobori Jr. and T. Yokobori, Eds., Paper # 0809, CD ROM, Elsevier, 2001.
- 13) Hutson, A. L., Niinomi, M., Nicholas, T. and Eylon, D., *Int. J. Fatigue*, xx, 2002, pp. x-y.
- 14) Lee, H and Mall, S., *Trib. Int.*, 37, 1, pp. 35-44, 2004.

Ti-6Al-4V Fretting Fatigue Crack Precursor Damage Characterization

Alisha Hutson* and Shamachary Sathish[†]

Air Force Research Laboratory, Mechanical Behavior and Life Prediction Section (AFRL/MLLMN)

*Advanced Materials Characterization Group, Structural Integrity Division
University of Dayton Research Institute, Dayton, OH 45469-0128, USA.

[†]Air Force Research Laboratory, Nondestructive Evaluation Branch (AFRL/MLLP)
Wright-Patterson AFB, OH 45433, USA.

Abstract

An investigation was conducted to explore the nature of fretting fatigue damage prior to crack nucleation. In the experimental apparatus employed in this study, several locations on each test specimen exist where cracks can nucleate due to local contact conditions; however, not all of the sites have cracks upon test completion. This study was developed to evaluate the condition of non-cracked sites on several fretted specimens in an effort to identify differences between these and sites where small cracks were observed, and to locate sites where crack nucleation was imminent prior to removal of the contact.

A single test condition of 620 MPa average applied static clamping stress & 250 MPa applied axial fatigue stress for $R=0.5$ was selected, based on the quantity of data and test specimens from prior work. Several destructive and non-destructive characterization methods were chosen to facilitate material evaluation: SEM, residual stress measurement, transmission electron microscopy (TEM), and thermography. Each site at which crack nucleation could occur was inspected in the SEM and was then characterized using surface x-ray diffraction to quantify trends in the residual stresses. Then TEM foils were cut from one area on an as-received specimen with tiny cracks and dislocation densities were observed. A novel technique was used to prepare the TEM foils. A Focused Ion Beam (FIB) was used to cut small pieces from specific sites, identified with *in situ* SEM imaging. These pieces were then placed on a specially designed holder and thinned using the FIB to create sections of suitable thickness. This method permitted TEM samples to be obtained from regions in close proximity on the original specimen, a task that is not possible with conventional TEM preparation.

Comparisons were made between as-received and stress-relief annealed specimens, on which the stress-relief was applied prior to fretting fatigue testing. Comparisons were also made between specimens tested to fracture and specimens tested to 10% of an estimated fatigue life. SEM inspection was useful for qualitative analysis of wear debris and identification of cracks as small as 20 μm , but provided no quantitative data on the level of fretting fatigue damage beyond crack size. Trends were noted in the residual stresses for the stress relief annealed specimens, but the changes in residual stress on the as-received specimens were obscured by the initial residual stress produced by the manufacturing process. Also, no stress peaks were noted in the edge of contact regions, probably due to the small scale of the affected regions on the specimen compared to the 1 mm spot size used in obtaining the residual stress measurements. The dislocation structure decayed rapidly into the specimen thickness, but the cause of the dislocations, machining or EOC stress peaks, could not be determined with only one specimen. Thermography, which can usually identify cracks as small as 25 μm , was unable to identify

cracks on any of the specimens that were inspected with this technique. Although a more rigorous analysis is required to determine the cause of these results conclusively, the fretting debris in the crack mouth is a likely factor in obscuring the fretting fatigue cracks.

1. Introduction

Fretting fatigue is a type of damage that occurs due to the presence of contact between components that undergo concurrent bulk loading and small-scale relative motion. Different contact damage modes have been identified over the years [1-9], characterized mainly by the magnitude of displacement between the components, which is usually identified via experimentation. Fretting fatigue is generally considered to be the most detrimental of the different damage modes (wear from gross sliding, fretting fatigue from localized relative slip, and “no damage” from stick), because it results in cracking that occurs in regions of high stress gradients and localized relative motion that obscures cracks until they reach critical lengths.

Many different techniques have been investigated to detect or measure the level of fretting fatigue damage, including techniques such as surface profilometry, eddy current and ultrasonic crack detection methods. Most of these efforts have met with limited success, if any. Some prior work by one of the authors attempted to correlate surface profilometry measurements with reductions in fatigue strength. Results showed that, for the fretting fatigue conditions investigated, no measurable reductions in fatigue strength occurred unless cracks of measurable size, $\sim 100 \mu\text{m}$ surface length, were present (Fig. 1). The majority of the specimens that were subjected to fretting fatigue cycling during this study did not nucleate cracks, and the specimen design limited accurate fatigue strength reduction assessment to 10% or more. Thus, many samples with like fretting fatigue load history were available, and the onset of cracking was determined to be of great interest.

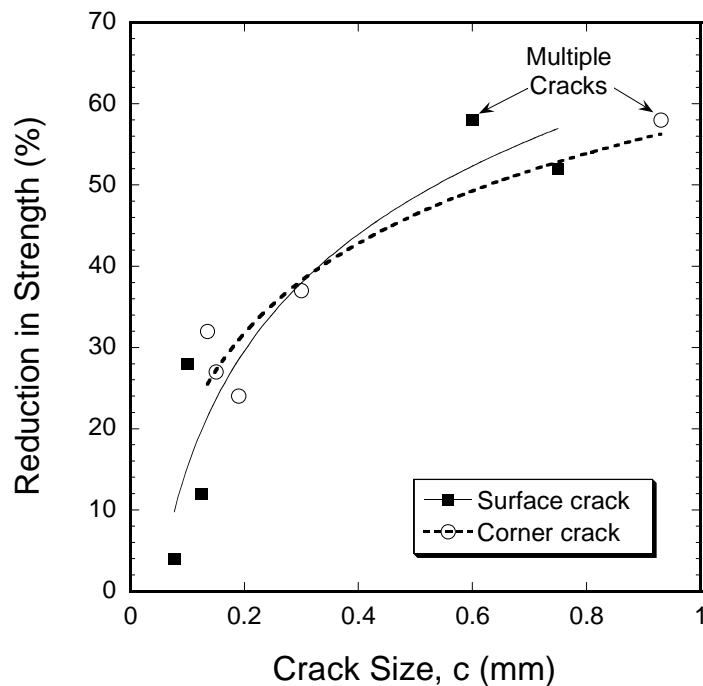


Fig. 1. Crack surface length (corner crack) or surface half-length (surface crack) vs. reduction in fatigue strength.

In an effort to identify the mechanisms that drive fretting fatigue damage propagation, the following research was begun. The objectives of the work were to characterize the non-crack fretting fatigue damage sites on specimens from the earlier study, and investigate various non-destructive inspection (NDI) techniques to determine if any of them were capable of detecting or quantifying the fretting fatigue damage. The methods selected for this work were Scanning Electron Microscopy (SEM), surface residual stress evaluation via x-ray diffraction, Transmission Electron Microscopy (TEM) and thermography. Further tests were conducted on specimens that were stress-relief annealed prior to application of the fretting fatigue damage, for comparison.

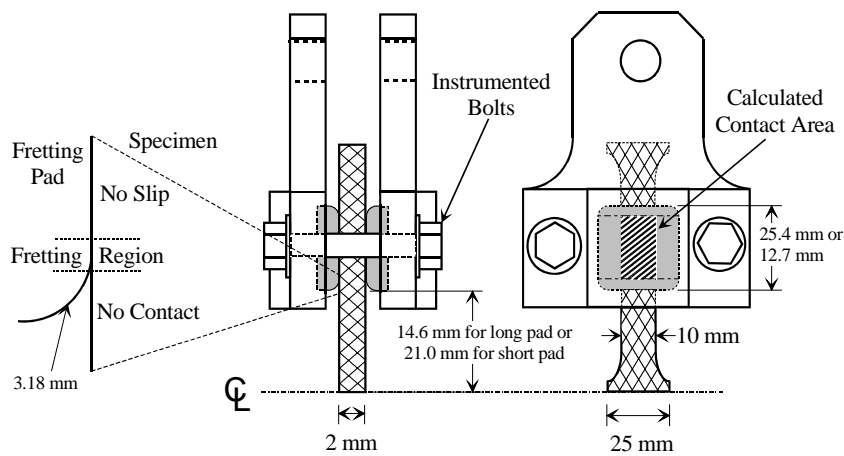


Fig. 3. Test fixture schematic indicating pad lengths, distance from center of specimen to lower edge of pad, and blending radius at edge of contact. [11]

In addition to the specimens obtained from the previous investigation, some stress-relieved specimens were tested to determine the effect of the substantial residual stresses produced during sample fabrication. After application of the fretting fatigue cycles, the specimens were bisected (Note dashed line in Fig. 4), and heat-tinted to mark the crack front of any fretting fatigue-nucleated cracks. Then the damage

characterization was performed.

Characterization of Fretting Fatigue Damage

Fretting fatigue damage was characterized using four independent techniques: Scanning Electron Microscopy (SEM), residual stress measurement via x-ray diffraction, and transmission electron microscopy (TEM). Four fretting regions (two on each side) along the EOC near the free edges of the specimens were selected for characterization based on optical assessments of where the worst fretting damage was located and based on results from previous work [12,13] indicating the edges as the locations most likely to nucleate fretting fatigue cracks. These regions were carefully tracked to provide references for the characterization results. Each specimen was assigned a front-top region at the beginning of the fretting fatigue test. Then, after the specimen was bisected and with the specimen oriented in the assigned configuration, each location of interest was numbered – 1 was assigned to the front, left region, 2 was assigned to the front-right region, 3 to the back-left region, and 4 to the back-right region. Presentation and discussion of the results will use this numbering system as reference.

Characterization in the SEM performed to provide a qualitative analysis of the wear surface, and was conducted using a small bend fixture designed to fit in the SEM chamber. In this fixture, the specimens could be inspected in the SEM while under a small bend load that would open cracks to improve visibility. The minimum detectable crack

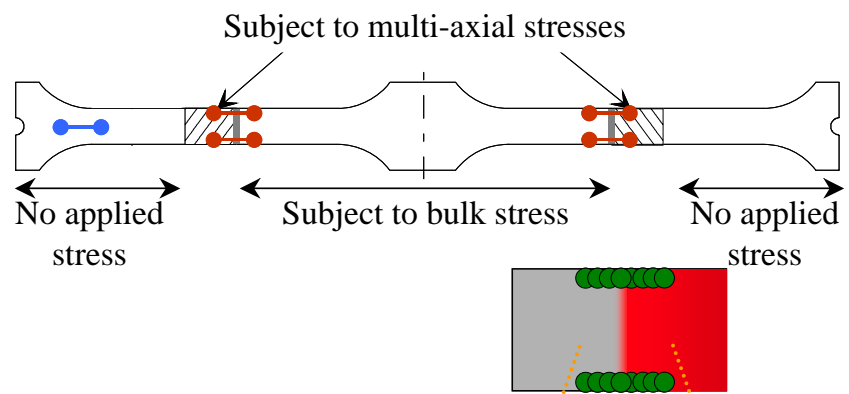


Fig. 4. Schematic of locations where residual stresses were measured on the twin dogbone specimens. Blue line denotes the location of baseline data acquisition. Red lines denote measurements made in the fretting fatigue regions of interest. (Inset: red shaded region denotes contact region, row of green circles corresponds to the red lines in schematic.) The vertical dashed line indicates bisecting location for post-fretting characterization and testing.

size was $\sim 20 \mu\text{m}$ (surface length), so specimens without cracks could be identified with a reasonable level of reliability.

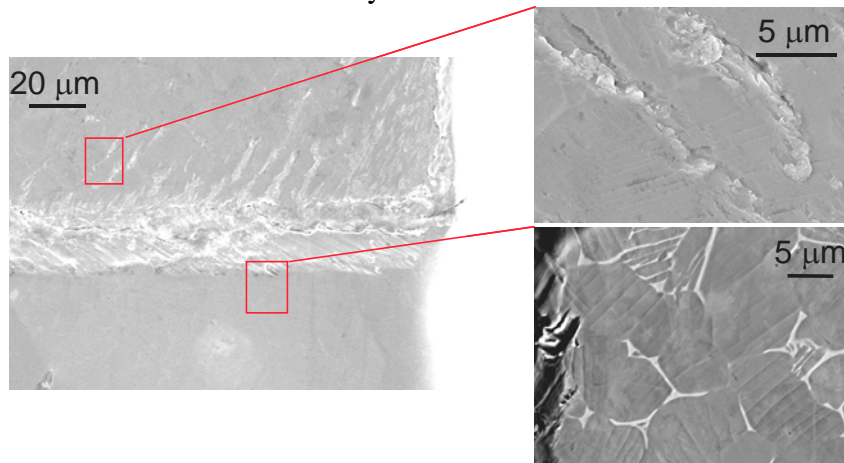


Fig. 5. Overall SEM image of a fretting scar on a highly polished specimen (left), and two regions adjacent to the fretting fatigue crack that show evidence of underlying dislocation structure in the form of persistent slip bands. Note that both magnified views are rotated 90 degrees counter clockwise from their orientation in the left-hand photo. [14]

All of the SEM imaging was conducted using a backscatter emission method that enhances variations in grain structure and elemental content. In the context of this study, the backscatter imaging augmented the wear product imaging to simplify location of the fretting scars and to allow qualitative analysis of wear debris.

The residual stress measurements were performed on the eight regions of interest using x-

ray diffraction, as shown in Fig. 4, corresponding to the red lines on the schematic. Note that the four not shown in this figure are on the back of the specimen. In each of these regions, a series of overlapping surface stress measurements were obtained to identify changes in the residual stresses due to fretting at the edge of contact and due to the overall contact stresses. A 1 mm spot size was used, and residual stresses were measured in each location, beginning 2 mm beyond the trailing edge of contact and moving in 0.5 mm steps along the edge of the specimen, to 2 mm into the contact patch (Note intersecting green circles in the inset of Fig. 4. Residual

stresses were also measured in a region of the specimen that was not subjected to either the contact load or the fatigue load to provide a baseline for comparison of the other data, represented by the blue line in Fig. 4. These data were of particular interest, since the specimens from the original study were known to have rather high initial residual stresses from the fabrication process.

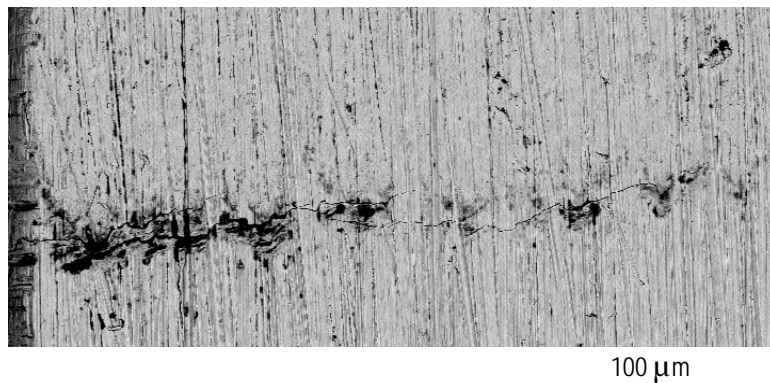


Fig. 6. 750 μm fretting fatigue crack and related wear damage. [11]

A limited TEM analysis

was conducted to investigate trends in dislocation density in and adjacent to the region of crack nucleation. In earlier work, some evidence of this strain accumulation mechanism was identified on a specimen that was highly polished prior to testing (Fig. 5) [14]. The TEM work was intended to confirm the mechanism's role in fretting fatigue damage accumulation by inspecting

foils cut at the edge of contact, in the region of highest visible damage, and some small distance away from the trailing edge of contact, for comparison. A novel technique was used to prepare the TEM foils. Conventional foil preparation techniques cannot be used near edges, and the exact (original) location of such foils is uncertain. The technique used here involved the use of a Focussed Ion Beam milling system incorporated in an SEM to pinpoint the desired locations and extract them from the sample. The

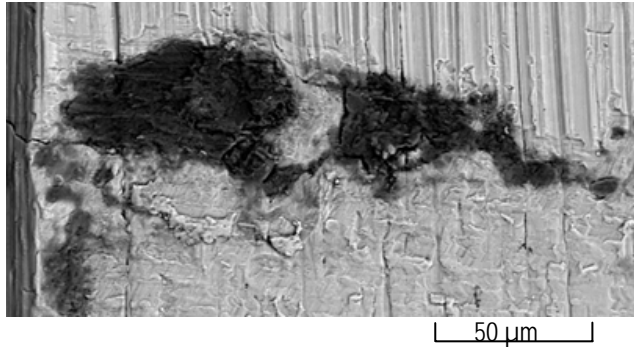


Fig. 7. 150 μm fretting fatigue crack and associated wear damage. Specimen edge is at the left side of the photo. [11]



Fig 8. 50 μm fretting fatigue crack and associated wear damage. Specimen edge is at the left side of the photo. [14]

benefits of this technique include the ability to cut foils from almost any sample of suitable size (must be able to fit into the SEM chamber), to cut multiple samples in close proximity (within tens of microns of each other), and to leave the foil source largely intact. The technique is also much cleaner and faster than conventional TEM foil preparation.

significant, but probably developed during crack propagation. In support of this hypothesis, the wear damage in the region of smaller cracks is shown in Figs. 8 and 9 [14]. Cracks of this size would produce only minimal fatigue strength reductions, if any, and the level of wear damage is notably less than was found adjacent to larger cracks. Of particular note in Fig. 9, the two tiny cracks observed on this sample appeared within the wear scar, but without any wear debris in the immediate vicinity.

3. Results and Discussion

SEM Characterization Results:

Results from the SEM characterization are presented in Figs. 6-13. For comparison, some micrographs of cracked specimens are included from [11 and 14]. The wear damage observed in the presence of sizable cracks (those that will reduce fatigue strength markedly) is shown in Figs. 6 (above) and 7 (below). These cracks were measured at 750 μm and 150 μm , respectively, and have previously been reported in reference [11]. In these photos, the wear damage appears to be

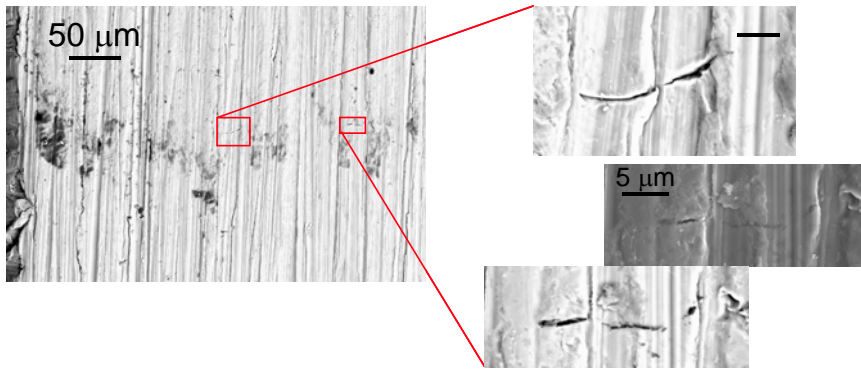


Fig. 9. 10 μm fretting fatigue cracks and adjacent wear damage. Specimen edge is at the left side of the left-hand photo. Red boxes indicate locations of magnified views. The two images in the lower right-hand corner are of the same region, but were taken using different techniques to emphasize the ability of wear debris to obscure small cracks. [14]

Wear is minimized in specimens without cracks, as shown in the examples in Figs. 10 through 13, for both as-received and stress relief annealed specimens. Levels of wear such as this are invisible to the naked eye and most often cannot be seen using any form of optical microscopy. The images in these figures were taken in an SEM, but as shown in the lower-right

inset in Fig. 9, these low levels of wear are difficult to locate with typical SEM imaging. Backscatter emission imaging, a technique that enhances differences in composition, was the method that provided the best images and simplified location of regions, such as those shown in Figs. 10 through 13. These results would seem to indicate that wear levels are not a suitable measure of fretting fatigue damage in this fretting fatigue apparatus, as has been noted in the authors' earlier work [11; 14]. It should also be noted that the level of wear can change markedly with changes in applied loads, number of cycles, material pair, etc [12,15].

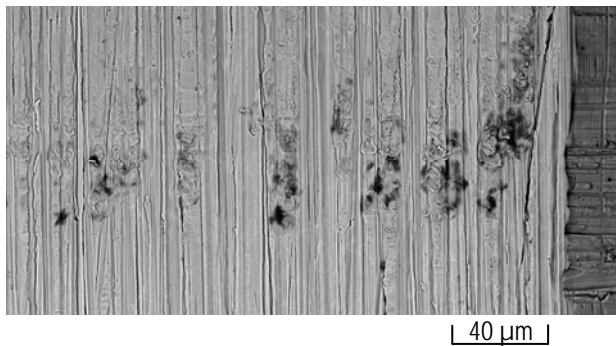


Fig. 10. Wear damage on an as-received specimen without fretting fatigue nucleated cracks.

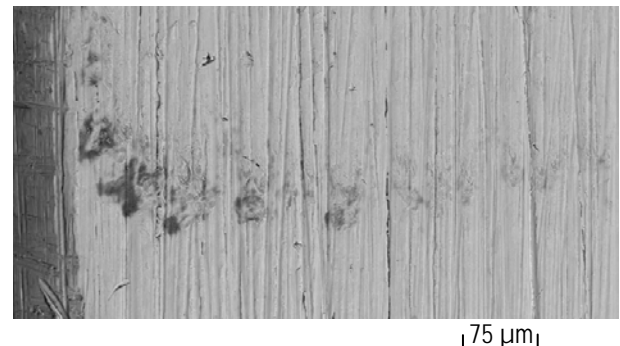


Fig. 11. Wear damage on an as-received specimen without fretting fatigue nucleated cracks.

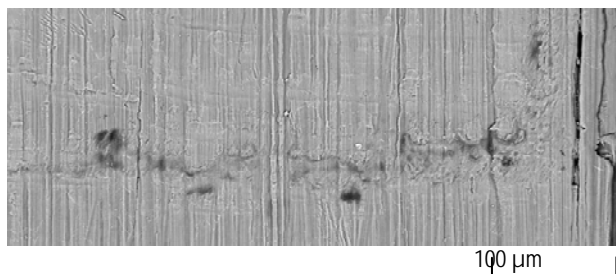


Fig. 12. Wear damage on a stress-relief annealed specimen without fretting fatigue nucleated cracks.

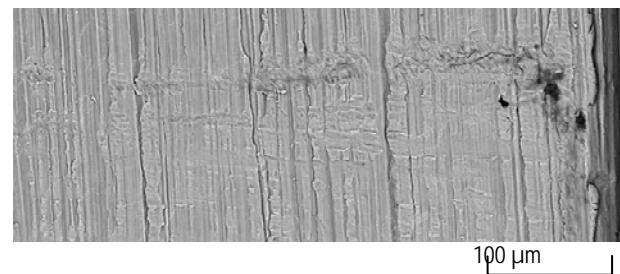


Fig. 13. Wear damage on another stress-relief annealed specimen without fretting fatigue nucleated cracks.

X-ray Diffraction Characterization Results:

The results for the residual stress measurements are shown in Figs. 14 through 17. The four series of overlapping residual stress measurements are shown for a representative as-received specimen in Fig. 14; similar data are shown for a representative stress-relieved specimen in Fig. 15. For each location, 1 through 4, in both figures zero (0.0) corresponds to the fretting edge of contact (EOC). Measurements on the as-received specimens did not reveal any significant trends. Initial residual stress values were quite high, between 200 & 400 MPa compressive. Some trends were observed in the residual stresses measured on the stress-relieved specimens (Fig. 15). Initial values were ~0 (5-15 MPa compressive), but increased in magnitude to ~100 MPa compressive. This change reflects the plasticity induced by the contact loads applied to the specimen.

No peaks in the residual stresses were observed near the edge of contact, perhaps due to the highly localized nature of the damage and surface area represented by each point on the residual stress curves in Figs. 14 and 15. The damage zones observed during SEM characterization were not more than 100 μ m wide (Figs. 10 – 13), which represents only 10% of the spot diameter (1 mm) used in acquiring the residual stress values shown in the plots.

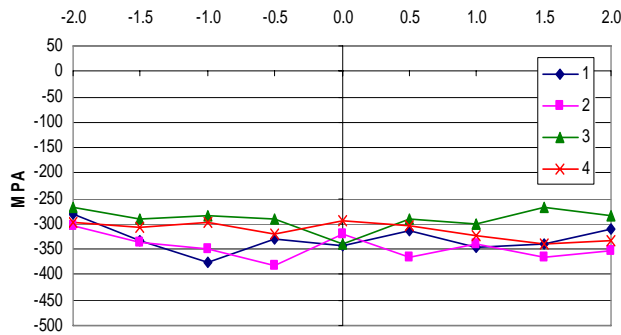


Fig. 14. Residual stresses plotted as a function of location for the as-received specimens.

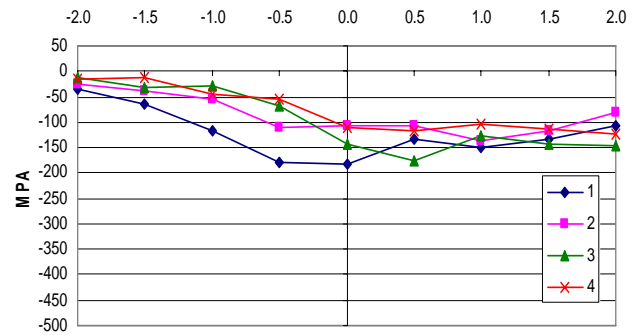


Fig. 15. Residual stresses plotted as a function of location for the stress-relieved specimens.

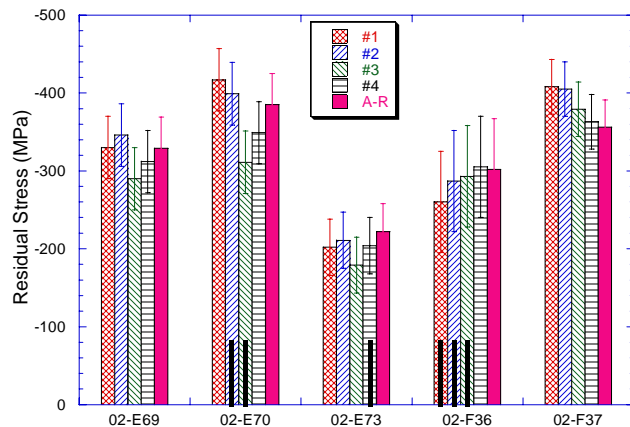


Fig. 16. Average residual stress values for all as-received specimens. Pink bars represent the stresses measured from the untested specimen surface. Black vertical lines on the bars indicate the presence of cracks, 20 μ m or smaller.

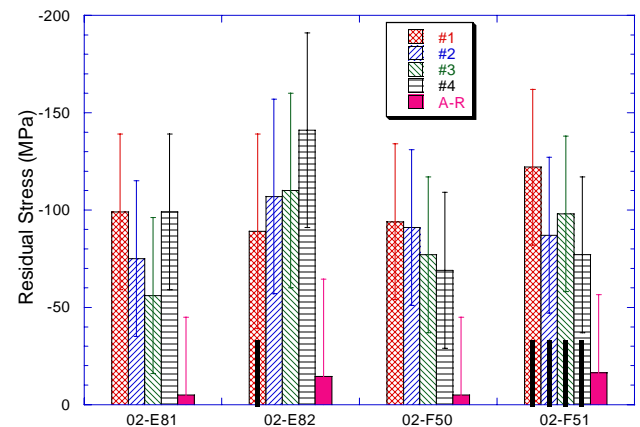


Fig. 17. Average residual stress values for all stress-relieved specimens. Pink bars represent the stresses measured from the untested specimen surface. Black vertical lines on the bars indicate the presence of cracks, 20 μ m or smaller.

The data shown in Figs. 16 and 17 are averages of each series of overlapping measurements from each of the five locations measured on each test specimen, including the baseline measurement. All data from each measurement series is included in each average. When averaged, the series from each of the four locations for the as-received specimens did not differ significantly from the corresponding specimen baseline values. No trend was observed in residual stress averages for the stress-relieved specimens, except that they were much higher than the baseline values (Fig. 17). Also, the presence of small cracks (50 μm or less), represented in both figures by vertical black lines, did not affect residual stress values. In both types of specimens, residual stress averages for the four fretting fatigue locations differed by as much as 100 MPa on a single specimen.

TEM Characterization Results:

Results for the TEM analysis are shown in Figs. 18 through 22. The TEM technique was selected in part, based on earlier observations of persistent slip bands on a specimen that was polished prior to testing (Fig. 5). Observations of suspected strain-based features were found adjacent to a sizeable fretting fatigue crack, both under and adjacent to the contact region. Therefore, three regions were selected for characterization in the current study.

These regions are represented by dashed red rectangles in Fig. 18, and are designated A, B and C. In the figure, location B corresponds to the edge of the contact region, and is nearest to any location that might nucleate fretting fatigue cracks. Location C corresponds to a region in contact with the pad, and location A was adjacent to the pad (not in contact). These regions were purposely selected near the specimen edge (within $\sim 40 \mu\text{m}$), since no fretting fatigue cracks in this test geometry have initiated more than $500 \mu\text{m}$ from the specimen edge, and are usually much closer. The sections represented by the rectangles were cut to $20 \mu\text{m}$ into the specimen

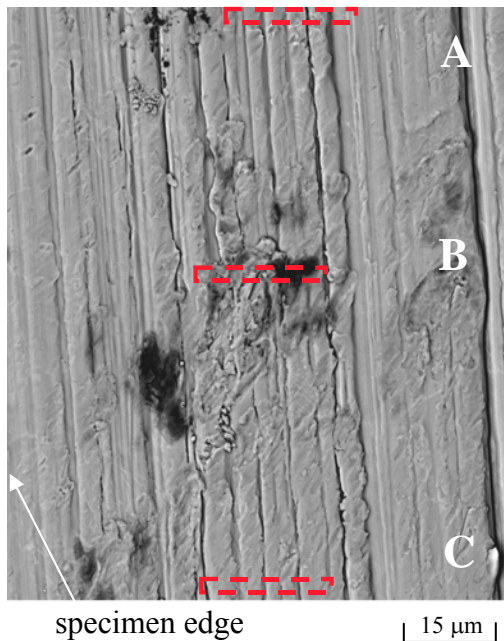


Fig. 18. Region of as-received specimen where TEM foils were taken (red dashed boxes). Region B = edge of contact, C = under the pad and A = adjacent to the pad.

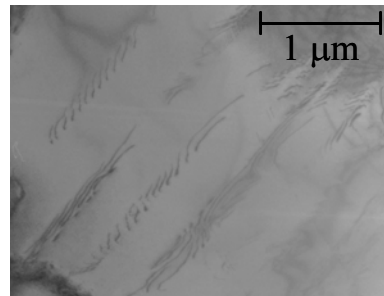


Fig. 19. TEM foil from Location A at a depth of $\sim 5 \mu\text{m}$.

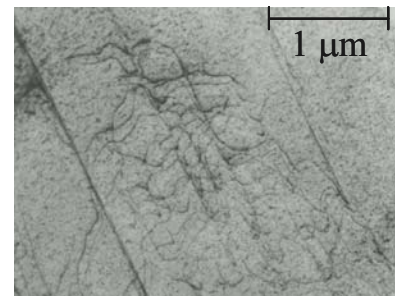


Fig. 20. TEM foil from Location B at a depth of $\sim 5 \mu\text{m}$.

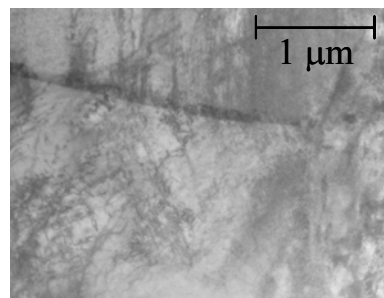


Fig. 21. Dislocation structure from Location B just below the surface.



Fig. 22. Dislocation structure from Location B at a depth of $\sim 10 \mu\text{m}$.

depth to allow an evaluation of the dislocation structure into the specimen thickness.

The photos shown in Figs. 19 through 22 were taken with parameters setting adjusted to maximize the visible dislocation structure. Regions A and B are compared in Figs. 19 and 20, respectively. Clearly, the number of dislocations increases markedly just at the edge of contact.

The change in dislocation structure into the specimen depth is shown by comparing Figs. 20, 21 and 22 for region B. The dislocation structure just below the surface, shown in Fig. 21, is sufficiently complex that single dislocations cannot be differentiated. In Fig. 20, 5 μm below the surface, a complex dislocation structure is still evident, but individual dislocations can be identified. The structure shown at 10 μm below the surface (Fig. 22) reveals no discernable dislocation structure at all. These results seem to support the stress gradient trends inferred from finite element analysis [16], in which the stress peaks that exceed the elastic limit for this material are limited to highly localized regions at the edge of contact, and decay rapidly both along the specimen surface and into the specimen depth.

Preparation of the foil from location C was not completed at the time of this writing, and further inspection of the foils from all three locations is desired. In addition, the mechanisms for the trends in dislocation structure are not clear, since the baseline residual stresses on the as-received specimens were so high. The source of the dislocations may be plasticity from the specimen manufacturing process. Thus, analysis of a stress-relieved specimen is also required, for comparison to the as-received results presented above.

Thermography Characterization Results:

Thermography is a non-destructive inspection technique that is based on acoustic excitation of a sample and detection of heat radiating from damage features such as cracks. It is capable of detecting cracks with surface lengths as small as 25 μm on typical uniaxial fatigue samples with naturally initiated cracks. This NDI technique was used to try to detect small cracks in the specimens from this study; however, no small cracks were detected. Additional samples from other investigations, on which cracks of significant size (500 μm or greater) were confirmed through other techniques, were then subject to the same inspection. Again, no indications of cracking were noted.

The fretting debris common to nearly all damage sites, in which relative motion between contacting components was instrumental in the damage accumulation, limits many surface inspection techniques. Prior investigations of fretting damage of test specimens subject to fretting fatigue has revealed that nearly all cracks identified in post-test SEM inspection had fretting debris in the crack mouths [14]. The presence of fretting debris is a likely cause of the poor thermographic response of the specimens inspected for this investigation.

4. Conclusions

1. Debris volume is a poor indicator of fretting fatigue damage, based on the low observed levels of wear in specimens without cracks compared to those with cracks of increasing size, on which wear appeared to increase with increasing crack length.
2. Surface residual stress values did not reveal any trends in as-received specimens, since the initial values were very high and were varied.
3. Some trends were observed in residual stress values obtained from stress-relief annealed specimens. These trends indicated plasticity produced by clamping stresses, but did not reveal any details about changes on the scale of the observed wear damage.
4. Surface residual stress measurements did not indicate the presence of very small cracks that were identified during SEM inspection.

5. A novel technique was demonstrated for TEM foil preparation that allows characterization of adjacent features, which are usually imaged using TEM techniques. Foils may be cut from regions only tens of microns apart, a task that cannot be achieved using conventional TEM foil preparation techniques.
6. From the TEM characterization it was observed that dislocation density increased where expected stress peaks occur, and decreased away from specimen surface. Further work is planned to further elucidate the source of the plastic deformation.
7. Attempts to identify fretting fatigue cracks of any size using thermography were unsuccessful.

Acknowledgements

This work was performed at Air Force Research Laboratory in the Materials and Manufacturing Directorate (AFRL/MLLMN) under the National Turbine Engine High Cycle Fatigue Program and was funded under contract to the University of Dayton Research Institute, Air Force Contract No. 33615-98-C-5214.

References

1. *Standardization of Fretting Fatigue Test Methods and Equipment, ASTM STP 1159*, M. H. Attia, and R. B. Waterhouse, Eds., American Society for Testing and Materials, Philadelphia (1992) pp. 153-169.
2. Dobromirski, J. M., *Fretting Fatigue, ESIS 18*, R.B. Waterhouse and T.C. Lindley, Eds., Mechanical Engineering Publications, London (1994) pp. 60-66.
3. Bryggman, U. and Söderberg, S., *Wear*, 125 (1988) pp. 39-52.
4. Zhou, Z. R. and Vincent, L., *Wear*, 181-183 (1995) pp. 551-536.
5. Fouvry, S., Kapsa, P. and Vincent, L., *Wear*, Vol. 200 (1996) pp. 186-205.
6. Nix, K. J. and Lindley, T. C., *Fat. Fract. Eng. Mat. Struct.*, 8 (1985) pp. 143-160.
7. Endo, K. and Goto, H., *Wear*, 38 (1976) pp. 311-324.
8. Chan, K. S., Davidson, D. L., Lee, Y-D. and Hudak, S. J., Jr., *Int. J. Fracture*, 112 (2001) pp. 299-330.
9. Hutson, A. L., Nicholas, T., and Goodman, R., *Int. J. Fat.*, 21, (1999) pp. 663 – 670.
10. Haritos, G. K., Nicholas, T. and Lanning, D., *Int. J. Fat.*, 21 (1999) pp. 643 – 652.
11. Hutson, A. L., Neslen, C. and Nicholas, T., *Trib. Int.*, 36 (2003) pp 133-143.
12. Hutson, A. L. and Nicholas, T., *Fretting Fatigue: Current Technologies and Practices, ASTM STP 1367*, D.W. Hoepfner, V. Chandrasekaran, and C.B. Elliot, Eds., American Society for Testing and Materials, West Conshohocken, PA (1999) pp. 308 - 321.
13. Hutson, A. L., Ashbaugh, N. E., and Nicholas, T., *Fretting Fatigue: Experimental and Analytical Results, ASTM STP 1425*, S. E. Kinyon, D. H. Hoepfner and Y. Mutoh, Eds., American Society for Testing and Materials, West Conshohocken, PA (2003) pp. 307-322.
14. Conner, B. P., Hutson, A. L. and Chambon, L., *Wear*, 255 (2003) pp 259-268
15. Hutson, A. L., Niinomi, M., Nicholas, T. and Eylon, D., *Int. J. Fat.*, 24 (2002) pp. 1223-1234.
16. Hutson, A. L., Nicholas, T., Olson, S. E. and Ashbaugh, N. E., *Int. J. Fat.*, 23 (2001) pp. S445-S453.

A Fretting Fatigue Crack Detection Feasibility Study Using Shear Wave NDI

Alisha L. Hutson and David Stubbs

Work Conducted and Supported by Air Force Research Laboratory, Materials and Manufacturing Directorate, Wright-Patterson AFB, OH 45433.

University of Dayton Research Institute, 300 College Park, Dayton, OH 45469-0128

ABSTRACT

A study was conducted to assess the viability of using Ultrasonic Shear Wave Non-Destructive Inspection (NDI) methods to detect fretting fatigue nucleated cracks in Ti-6Al-4V *in situ*. Use of this crack detection technique is hampered by the presence of electronic and acoustic noise in the laboratory environment as well as the presence of the contact pad in the experimental configuration. A previously established fretting fatigue test configuration was selected, in which nominally flat pads are held in contact against a thin, flat specimen and gross sliding of the pad against the specimen is eliminated. Experiments were performed at 300 Hz and $R = 0.5$ for average clamping stresses of 200 and 620 MPa. Applied fatigue stresses for these clamping stresses were 330 MPa and 250 MPa, respectively. The shear wave response was monitored during each test, and the test was interrupted when changes in the waveform were thought to indicate the presence of a crack. Also, the effect of the contact load and the sensitivity of the technique under the fretting fatigue conditions were assessed.

For the lower clamping stress, it was determined that a sizeable portion of life was spent nucleating cracks, and the propagation life was too short to allow interruption of the tests for this condition. At the higher clamping stress, cracks with a surface length of ~ 2.5 mm were detected on 10 mm wide specimens in tests conducted using the shear wave ultrasonic technique. While the presence of the contact produced changes in the ultrasonic waveform, additional changes occurred as the crack propagated that permitted crack detection. A simple waveform correlation was used to quantify the waveform changes, and thereby validate the viability of this NDI method for use in contact regions. In the configuration used for this study, the shear wave crack detection technique was insensitive to small cracks. Some refinements that could dramatically improve crack detection capability were discussed. Feasibility of detecting fretting fatigue cracks using *in situ* a shear wave ultrasonic nondestructive inspection (NDI) technique was demonstrated.

INTRODUCTION

Fretting fatigue, which is a phenomenon caused by localized relative motion between contacting components under vibratory load, has been shown in numerous studies [1-6] to produce early component failure through premature crack initiation. Depending on the test configuration, the type of contact and the loads applied, the portion of life spent nucleating fretting fatigue cracks can vary widely. Also, fretting fatigue damage has been shown to produce different types of cracks, many of which do not result in fracture [4]. Distinguishing which of these cracks will be life limiting for the component is a critical aspect of the fretting fatigue life prediction effort.

Heretofore only destructive analysis methods, such as metallography or post-fracture analysis, have been used to assess such crack damage. The physical constraints inherent in all contact problems have limited the use of most crack detection or *in situ* crack monitoring methods, such as optical-based methods, replication, surface acoustic emission and extensometer-based methods. Techniques that employ electrical resistance measurement may also be difficult to employ because of practical problems with adequate electrical insulation of both the specimen and contact pad.

Subsurface acoustic methods are viable in terms of circumventing the basic geometric challenges, but such efforts have not been applied to contact geometries. Thus, the purpose of the present investigation was to investigate the viability of applying such a technique, specifically, Shear Wave Ultrasonic NDI, in an *in situ* laboratory fretting fatigue environment. The test fixture that was selected has been used in investigating fretting fatigue behavior and results on the effect of several factors critical to the fretting problem have been documented [5,7].

Some specific challenges were present in this effort, since the test environment introduced some features not found in environments where ultrasonic crack detection is typically used. Electro-magnetic interference and acoustical noise produced by the test machine introduced sources of signal noise that could corrupt the signal or obscure crack reflections. Also, cracks were expected to nucleate at the edges of the specimen while the shear wave energy was focused on the center of the specimen. Further, the potential existed for cracks to propagate to critical lengths before waveform changes could be identified and the test stopped. Mechanical tests were designed to address these issues. Two specific loading conditions with a known fretting fatigue life and representing a range of operating conditions were selected. The behavior of the ultrasonic waveforms was compared for varying contact loads with and without applied bulk load. The sensitivity of the technique was also addressed by incorporating small, strategically placed notches for some of the experiments. Finally, the ultrasonic waveforms were monitored during testing to determine if cracks at the edge of contact could be identified.

EXPERIMENTATION

Materials & Machining

Fretting fatigue specimens and fretting pads were machined from forged Ti-6Al-4V with an $\alpha+\beta$ duplex annealed microstructure. The specimens were machined with the fatigue axis oriented in the longitudinal direction. The material yield strength was 930 MPa, the tensile strength was 980 MPa, and the modulus was 120 GPa. Processing and microstructure details are can be found in reference [8]. All specimens and fretting pads were low stress ground to an RMS 8 μ inch surface finish. Based on characterization work from previous investigations, no cracks were expected in the pads, so the orientation with respect to loading for the pads was not specified or identified.

Fretting Fatigue Apparatus and Test Conditions

In the test apparatus used for this investigation, a relatively thin, flat specimen was tested against flat pads with a specified blending radius at both edges of contact (see Figure 1). Unlike many typical fretting fatigue test systems, the entire load applied to the specimen was transferred

to the fretting pads through shear. Thus, gross sliding is eliminated for all valid tests and damage is accumulated, in the form of wear scars and cracks, in a relatively small slip region that occurs at the edge of contact (see magnified view in Figure 1).

Tests performed in this fixture result in four fretting scars per specimen – one per fretting pad, or two on each end of the specimen. When nominally identical contact conditions are applied in each grip, as in the current work, fracture surfaces and non-failure fretting scars are available for post-mortem inspection from each test. Also, any *in situ* inspection methods must be able to simultaneously view four fretting fatigue locations.

For the current experiments, two fretting fatigue conditions were selected, based on earlier work by one of the authors [6]. Nominal fretting pad lengths were 12.7 mm and 25.4 mm. A blending radius of 3.18 mm was used, resulting in undeformed contact lengths of 6.35 mm and 19.05 mm. Static clamping loads were imposed via instrumented bolts to produce constant average clamping stresses of ~200 MPa for the longer contact length, and ~620 MPa for the shorter contact length. In earlier work, the cyclic axial fretting fatigue limit stress for a 10^7 cycle fatigue life was determined to be ~350 MPa for the lower clamping stress and ~250 MPa for the higher clamping stress [6]. These conditions were identified for an applied fatigue stress ratio, R , of 0.5 for tests conducted at 300 Hz under ambient laboratory conditions. Additional details can be found in [5].

Three specimens 10 mm wide by 2 mm thick were tested for each of the two selected fretting fatigue condition to address repeatability of the Shear Wave NDI technique being investigated. In addition, a specimen with four strategically placed EDM notches of varying size and location along the fretting scar, was tested at the higher clamping stress condition, to help establish the sensitivity of the technique. Two notches (250 μm and 500 μm surface length) were placed on the midline of the specimen on the front face. Two additional 500 μm notches were placed on the back, ~0.7 mm from the specimen midline on the top fretting location, and ~2.1 mm from the midline on the bottom location. Each specimen was fatigued at constant maximum stress until cracks were detected using the shear wave crack detection technique described below, or until the specimen fractured. Mechanical load and frequency control were maintained using in-house software specifically designed for high frequency testing. Details of the test system can be found in [5].

Crack Detection Apparatus

In situ detection of fretting fatigue cracks was attempted using ultrasonic shear wave NDI. Shear wave is a common NDI technique often used to inspect components with inaccessible surfaces, such as the contact region of the fretting fatigue specimens in this investigation. Ultrasonic shear waves are directed into the region where cracks may exist in the component and then the shear wave energy that reflects from cracks is detected. The propagated or “incident” shear waves are usually created by mode conversion of longitudinal waves (emitted by an ultrasonic transducer) through coupling wedges on the surface of the component (see Figure 2.) When directed at appropriate angles the incident shear waves propagate through the component through multiple internal reflections, as shown in Figure 2. In general, cracks with cross-sectional dimensions equal to or larger than the ultrasonic wavelength reflect and/or scatter enough ultrasonic energy to be detected. A portion of the reflected shear wave energy propagated back through the component is converted into longitudinal energy in the coupling wedge and detected by the transducer.

For this work it was desired to detect fatigue cracks on the order of 0.25 mm in a Ti-6Al-4V alloy for which the shear wave velocity is 3.29 mm/ μ s [9]. The frequency needed to generate ultrasonic shear waves in Ti-6Al-4V with 0.25 mm wavelengths is \sim 13 MHz. Ultrasonic transducers¹ with a center frequency of 10 MHz and -6 dB bandwidth greater than 10 MHz were selected. The transducers screwed into polymer coupling wedges designed to produce 45° shear waves in steel. Since the shear wave velocities of Ti-6Al-4V and many steels are nearly identical, the coupling wedges would produce 45° shear waves in the Ti-6Al-4V fretting fatigue specimens. Two commercial ultrasonic pulser-receivers² with variable excitation energies, adjustable gains, variable damping, and high/low pass filters were used to excite the ultrasonic transducers and receive signals from them. The received ultrasonic signals were digitized by a commercial analog-to-digital converter³ with a 100 MHz sampling rate and 8-bits of amplitude resolution. The digitized ultrasonic signals were stored in a standard PC and were available for viewing during the fatigue tests.

The fretting fatigue specimen and pad configuration was not changed when using the ultrasonic transducers. Two transducer-coupling wedge assemblies were attached to the fretting fatigue specimen using a fast curing epoxy after the specimen was installed in the test fixture. The transducers were attached on opposite sides of the specimens and directed the ultrasound in opposing directions (Figure 1). This configuration directed the shear waves into the region beneath the fretting pads where fatigue cracks were expected to occur.

Both transducers propagated ultrasonic energy into the specimen at a repetition rate of approximately 1 kHz during the mechanical fatigue testing. In the region where the fretting pads were in contact with the specimen, some of the shear wave energy was reflected back to the transducers (see Figure 1). As the fretting tests progressed, and as cracks initiated and grew, the signature of the reflected ultrasonic energy in the time window preceding the pad reflections changed. This time window corresponded to the region of the test specimen directly beneath the fretting pad edge of contact. Cracks were detected by comparing successive ultrasonic signals acquired at 500,000 mechanical fatigue cycle intervals.

Throughout each test the analog ultrasound waveform was monitored by watching for changes in the amplitude and shape of the various peaks. When changes in the waveform suggested the presence of a crack, the specimen was removed to optically verify the crack. If no crack could be identified under 100X magnification, the specimen was replaced in the test frame in the original position and the test was continued. If a crack was found, the damage at all potential crack sites was documented in the scanning electron microscope (SEM) and the specimen was heat treated to mark the crack size on the fracture surface. Then, the specimen was replaced against the same set of pads and cycled to fracture to provide data on fatigue crack propagation life for the complex loading condition.

After each test was completed, the ultrasonic data were processed to allow verification of observations made during the test. The data processing was conducted to slightly shift each waveform forward or backward in time so that the arrival time of the largest pad reflection was set to a selected value. This process was required because the mechanical strains induced during

¹ Model V5020, Panametrics, Inc., 221 Crescent St., Waltham, MA 02154

² Model 5072, Panametrics, Inc., 221 Crescent St., Waltham, MA 02154 Model PR35, JSR Ultrasonics, Inc., 3800 Monroe Ave., Pittsford, NY 14534

³Model DASP100A, Signatec, Incl, 355 N. Sheridan Street, Corona, CA 91720

mechanical testing changed the time-of-arrival of the ultrasonic reflections between successive data acquisitions. Although the time changes were small, approximately 0.06 μs , alignment in time of all of the ultrasonic signals improved the analysis for crack detection.

The interface between the test specimen and the fretting pad reflected the ultrasonic shear waves and typically produced a series of peaks separated by approximately one microsecond. The multiple reflections at $\sim 1 \mu\text{s}$ intervals occur because of the width of the ultrasonic beam, the thickness of the test specimen, and the length of the specimen / pad interface. For the *in situ* tests reported in this paper, the ultrasonic waveforms typically had three dominant peaks characteristic of the specimen / pad interface.

EXPERIMENTAL RESULTS

High Clamping Stress

Of the four experiments performed at the 620 MPa clamping stress (including one with EDM notches – 97H04), three resulted in successful crack detection, 99B60, 99B61 and 97H04. In each case the detected cracks were fairly large, even when considering that the cracks were expected to be shallow. However, changes in the waveforms that were thought to indicate the presence of a crack were observed for those tests in sufficient time for the test to be interrupted and the sample inspected.

Some fluctuations in the waveform peak amplitudes occurred throughout the tests that were not thought to be due to crack nucleation. Figure 3 shows, for example, ultrasonic waveforms acquired for 99B61 between 2,500,000 and 4,500,000 cycles along with an average of those five waveforms. (These waveforms are presented as they were acquired, i.e., no signal processing has been done. The waveforms have been aligned in time to account for very small timing errors - less than 0.06 microseconds). The deviation from the average is remarkably small in the region of interest immediately preceding the two strong reflection peaks from the fretting pad (at ~ 33 and $34 \mu\text{s}$).

In contrast, Figure 4 shows waveforms taken at 6,000,000 and 6,100,000 cycles along with the average waveform shown in Figure 3. Deviations from the average are noticeable at many points in time before the fretting pad reflections, between 25 and $\sim 33 \mu\text{s}$ in time, some of which are identified with arrows on the figure. These deviations were noticeable when looking at the oscilloscope screen showing the ultrasonic signals during testing, on which an “average” waveform – observed in the early portion of the test – was traced on a transparent overlay for comparison. The deviations in the ultrasonic waveforms noticed at 6,000,000 and 6,100,000 cycles occurred just prior to failure at 6,227,000 cycles, but were sufficiently large to be noticed in time to stop the test (at 6,125,000 cycles) for specimen evaluation before failure. Obviously, the time to propagate the detected cracks to failure was very small compared to the total specimen life, as may be concluded from the fracture surface shown in Figure 5. In this image, the dark region of the fracture surface indicates the crack depth at the time the test was interrupted.

Figure 6 shows ultrasonic waveform results for specimen 99B60. Included are waveforms taken between 5,100,000 and 7,000,000 cycles and an average curve obtained from waveforms taken between fatigue cycles 2,100,000 and 4,545,000. Deviation from the average was very small throughout the first 5,000,000 cycles (not shown), as was seen for similar waveforms taken on specimen 99B61 early in the fatigue testing (see Figure 3). For data

obtained after 5,000,000 cycles, several significant deviations from the average waveform are marked by arrows in the figure. Careful examination of the waveforms shows changes in the waveforms beginning with the data taken at 6,550,000 cycles. The waveform taken at 7,000,000 cycles prompted stopping the fatigue testing for specimen evaluation. Failure occurred at 7,350,000 cycles. The corresponding fracture surface is shown in Figure 7 in which three gray regions can be observed. The lightest gray is the fast-fracture region, the intermediate gray is a region of crack propagation, and the dark gray is the region that was cracked at the time the test was interrupted.

A simple numerical analysis was performed on this data to quantify the results observed on the plots in Figures 3, 4 and 6. For the waveforms of interest, the difference between the waveform of interest and the average waveform for that specimen was evaluated for each point between 25 and 40 μ s. Then the absolute value of those differences were added together for the given time window, and the sum from each waveform was compared with the other sums from the same specimen. The results from this analysis for 99B60, 99B61 and 97H04 are shown in Figure 8. The crack signature is clearly indicated by a sharp increase (double or more) in the value of the sum for each specimen for the two data sets taken prior to the interruption of each test. For 99B61 and 97H04, the sums increased from \sim 5,000 (approximate average of the data for waveforms b06 through b12) to 14,000 for b13 and to \sim 18,500 for b14. Similarly for 99B60, the sums increased from \sim 6,000 for waveforms b06 through b13 to 14,000 for b14 and b15. These results indicate that the fluctuations in the waveform that were thought to indicate a crack are quantifiable and could potentially be used to automate crack detection using this technique.

Low Clamping Stress

Three tests were conducted at the 200 MPa clamping stress, however, none of the attempts to detect cracks on specimens subjected to the lower clamping stress using the shear wave NDI technique were successful. Throughout each test no shear wave signal changes indicative of crack nucleation could be verified over the life of the specimen. While some variations in the signals over time were noted, those changes were limited to variations in the amplitude of existing peaks. Almost no “new peaks”, indicative of a new source of reflected ultrasound (crack) were observed. One test was stopped at 10.9 million cycles and inspected in the SEM, but no cracks were observed on this specimen (99B57). Also, unfractured ends of the fractured specimens were characterized in the SEM. No cracks were found on any of the non-fracture locations either. These observations led the authors to conclude that changes in the amplitude of the waveform peaks were not representative of crack nucleation, but of other phenomena, such as random electronic noise and changes in the coupling of ultrasonic energy from the refraction wedges into the specimen.

The data for 99B57 was reduced using the analysis described above; the results are shown in Figure 9. The sums shown here are \sim 3,500, except for waveform b15. Although the sum at b15 is nearly double the other values, it was not repeated in b16, and observations of the *in situ* signal did not give any reason to interrupt the test. Inspection of waveform b15 indicated high levels of electronic noise corrupting the signal and so, the data for b15 are considered invalid.

In related work, fretting fatigue experiments were performed at nominally identical loading conditions to those for the current work, but the tests were interrupted at an estimated 10% life of anticipated life [10]. When these 10%-of-life specimens were inspected, cracks of

up to 1 mm surface length were observed in many of the specimens subjected to the higher clamping stress, but no cracks of any size were found in the specimens subjected to the lower clamping stress. Further, a Finite Element Analysis of the test fixture performed to evaluate stress fields in the test specimens under these same conditions indicated stress peaks for the higher clamping stress condition that were of the order of the yield stress for the Ti-6Al-4V used for the specimens [6]. FEA results for the lower clamping stress indicated much lower stress peaks. These experimental and FEA results, taken together, suggest that cracks nucleate later in life for the lower clamping stress condition, a hypothesis supported by the SEM inspection results from 99B57. Since the tests were performed at 300 Hz, the ability to detect those cracks is severely limited.

Sensitivity Evaluation

Some additional data were taken for 97H04, on which EDM notches had been machined, to help explore the sensitivity of the Shear Wave crack detection method. Specifically, the effects of notch size and location, coupling method and clamping load on the shear wave signal were interrogated. The results of these efforts are discussed here in brief, to aid future efforts to apply shear wave crack detection to similar problems.

Notches of varying size and location were inspected using the shear wave technique. With traditional ultrasonic coupling gel, both center notches were detected. The off-center notches could only be detected if the wedge/transducer assembly was directed toward the notch. None of the notches were visible when the fast-curing epoxy was used in place of the traditional couplant. The loss of sensitivity is due to the thicker coupling layer produced with the epoxy [11]. No attempt was made to reduce or quantify the thickness of the epoxy layer during these experiments.

The effect of clamping load on the ultrasonic signal was investigated using zero clamping load as the baseline, and comparing the response signals obtained with clamping loads at 50% and 100% of the that used during the fatigue tests (20 and 40 kN, respectively, for the ~620 MPa clamping stress). The reflections from the edge of contact increased in magnitude with increasing clamping load, but otherwise the signal remained stable. For the current series of experiments, the signal increase is trivial. Once the clamping load is applied in the test apparatus used here, it remains constant throughout the remainder of the test. However, complications in using this crack detection method will occur with contact conditions that do not maintain a constant pressure on the contact, since significant changes in the signal will occur that are an effect of the changing load. It should also be noted that the ultrasonic response signal changed again, with a further increase in the edge of contact pad reflections, as the bulk load was applied. Thus, effective application of this method must avoid comparing signals that were obtained under different loading situations.

DISCUSSION / CONCLUSIONS

The results from the tests of specimens 99B61, 99B60 and 97H04 demonstrated the feasibility of using the shear wave crack detection technique *in situ* in the high frequency contact laboratory environment of this study. Feasibility of using the shear wave ultrasonic technique was demonstrated despite the considerable acoustic and electro-magnetic noise generated by the high frequency mechanical fatigue apparatus. Coupling of the pad and specimen introduced

changes that were observed as fluctuations in peak amplitudes for all of the specimens, but the presence of a crack was still identifiable in some of the specimens through observations of new peaks in the ultrasonic waveforms. These observations have been shown here to be quantifiable with the use of a simple difference calculation.

The cracks detected in these experiments were relatively large for either laboratory or service hardware inspections, but certain refinements could provide sufficient improvement in the crack detection resolution to make this method a viable one for use in crack detection in contact situations. First, efforts to minimize the thickness of the couplant layer would be of considerable benefit. In addition, the transducer/wedge assemblies used were designed to focus the ultrasonic signal down the center of the specimen while crack nucleation occurred near the specimen edges. Wedges designed to focus the ultrasonic signal in the area of interest would allow for detection of much smaller cracks. Finally, the use of software designed to compare each ultrasonic signal to previous signals would allow for automation of the technique. If such automation had been used in these experiments, the tests could have been interrupted earlier by as much as 500,000 cycles, thereby enhancing the crack detection sensitivity.

ACKNOWLEDGMENTS

This research was conducted at the Air Force Research Laboratory, Materials and Manufacturing Directorate (AFRL/MLLMN), Wright-Patterson Air Force Base, OH, USA. A. Hutson and D. Stubbs were supported under on-site contract number F33615-98-C-5214.

REFERENCES

1. *Fretting Fatigue, ESIS 18*, R.B. Waterhouse and T.C. Lindley, Eds., Mechanical Engineering Publications, London, 1994.
2. *Standardization of Fretting Fatigue Test Methods and Equipment, ASTM STP 1159*, M. Helmi Attia, and R. B. Waterhouse, Eds., American Society for Testing and Materials, Philadelphia, 1992.
3. Ruiz, C., Boddington, P. H. B., and Chen, K. C., "An Investigation of Fatigue and Fretting in a Dovetail Joint," *Experimental Mechanics*, Vol. 24, 1984, pp. 208-217.
4. Dubourg, M.-C. and Lamacq, V., "Stage II crack propagation direction determination under fretting fatigue loading: a new approach with experimental observations," *Fretting Fatigue: Current Technology and Practices, ASTM STP 1367*, D.W. Hoepfner, V. Chandrasekaran, and C.B. Elliot, Eds., American Society for Testing and Materials, West Conshohocken, PA, 2000, pp. 436-450.
5. Hutson, A., Nicholas, T., and Goodman, R., "Fretting Fatigue of Ti-6Al-4V Under Flat-on-Flat Contact", *International Journal of Fatigue*, Vol. 21, No 7, 1999, pp. 663 – 670.
6. Hutson, A. L., "Fretting Fatigue of Ti-6Al-4V under a Flat-on-Flat Contact with Blending Radii," *Masters Thesis*, University of Dayton, Dayton, OH, August 2000.
7. Hutson, A. and Nicholas, T., "Fretting Fatigue Behavior of Ti-6Al-4V against Ti-6Al-4V under Flat-on-Flat Contact with Blending Radii," *Fretting Fatigue: Current Technologies and Practices, ASTM STP 1367*, D.W. Hoepfner, V. Chandrasekaran, and C.B. Elliot, Eds., American Society for Testing and Materials, West Conshohocken, PA, 2000, pp. 308 - 321.

8. Haritos, G.K., Nicholas, T. and Lanning, D., "Notch Size Effects in HCF Behavior of Ti-6Al-4V," *International Journal of Fatigue*, Vol. 21, No 7, 1999, pp. 643 – 652.
9. U.S. Air Force Technical Report #AFML-TR-79-4214, Materials Engineering Materials Selector 1990, 1100 Superior Ave., Cleveland, Ohio 44114-2543.
10. Hutson, A.L., Nelsen, C. and Nicholas, T., "Characterization of Fretting Fatigue Crack Initiation Processes in Ti-6Al-4V," *Tribology International*, vol. 36, 2003, pp.133-143.
11. Stubbs, D., private communication, University of Dayton Research Institute, Dayton, OH, USA.

FIGURES

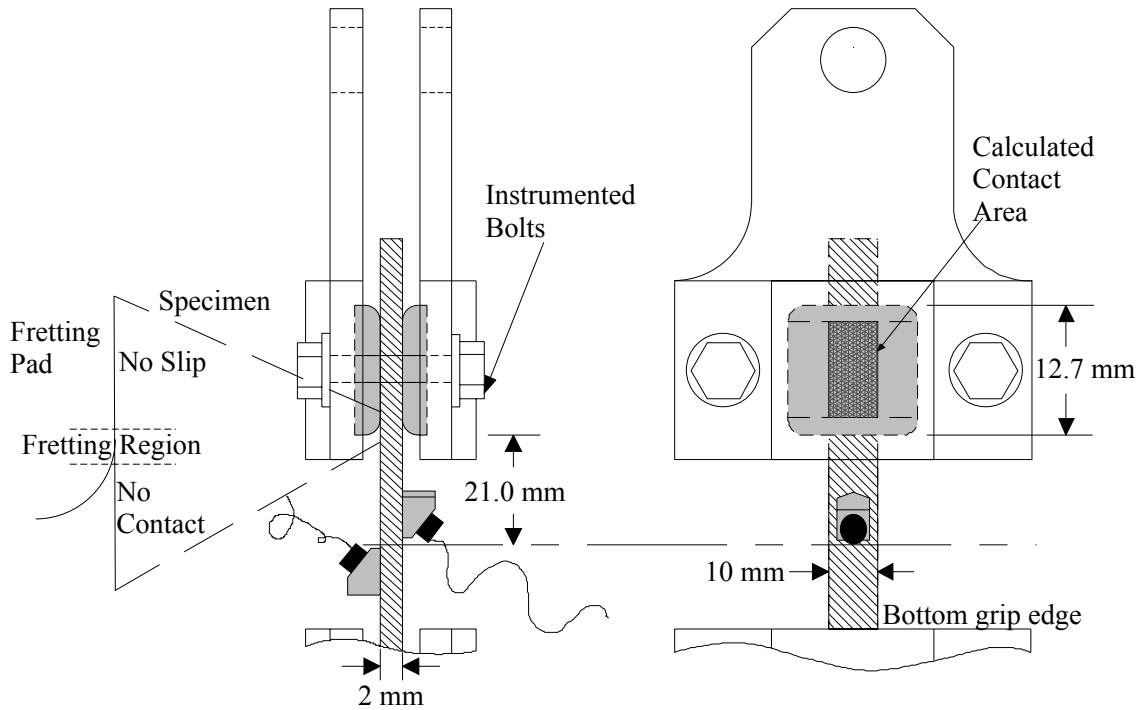


Figure 1. Schematic showing the fretting fatigue gripping system and the ultrasonic transducer placement.

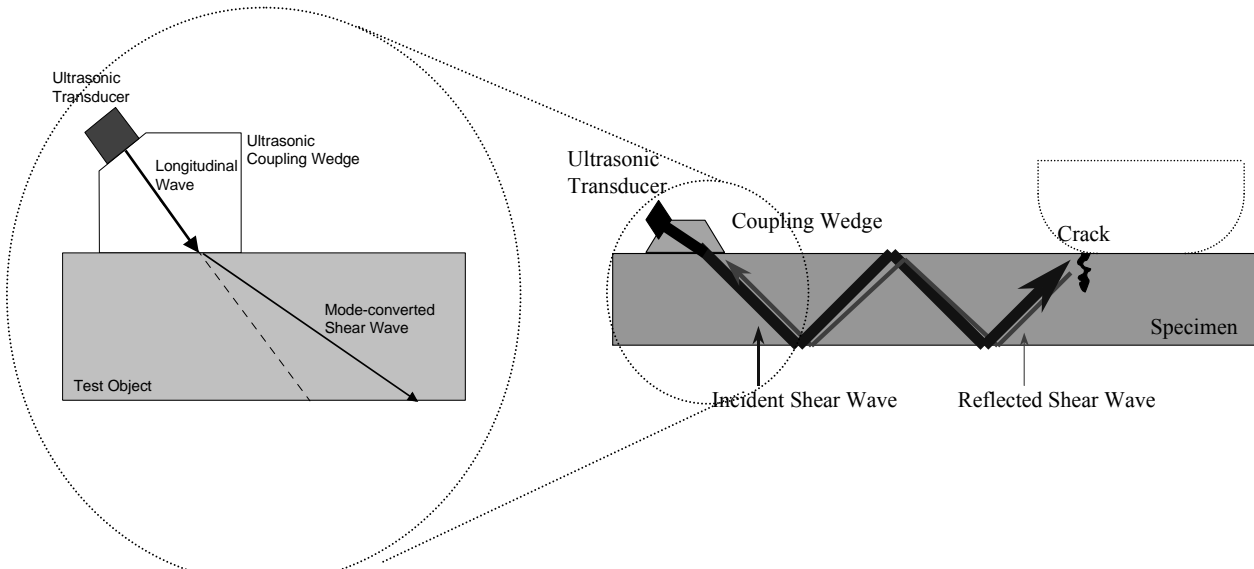


Figure 2. Coupling wedges were used to convert ultrasonic energy from longitudinal to shear wave modes. Internal reflections of the shear waves allowed ultrasonic energy to propagate through the specimen to the location underneath the fretting pads where fatigue crack initiated.

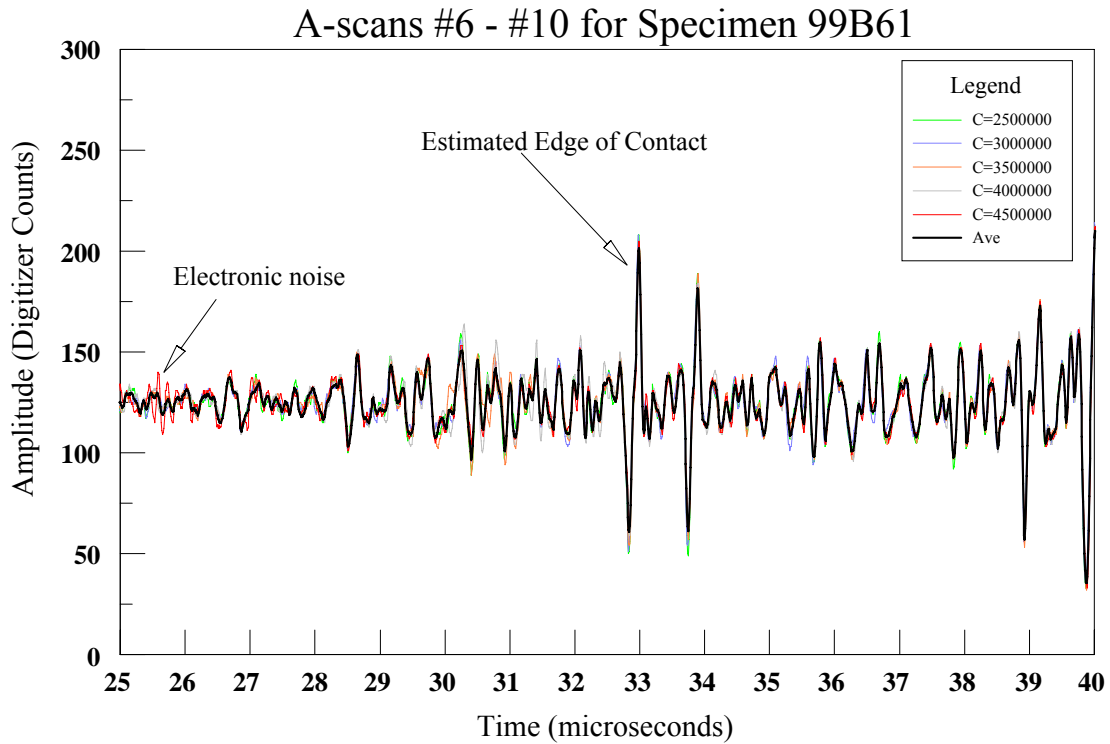


Figure 3. Ultrasonic waveforms from the early part of experiment 99B61 plotted as waveform amplitude versus time in μs .

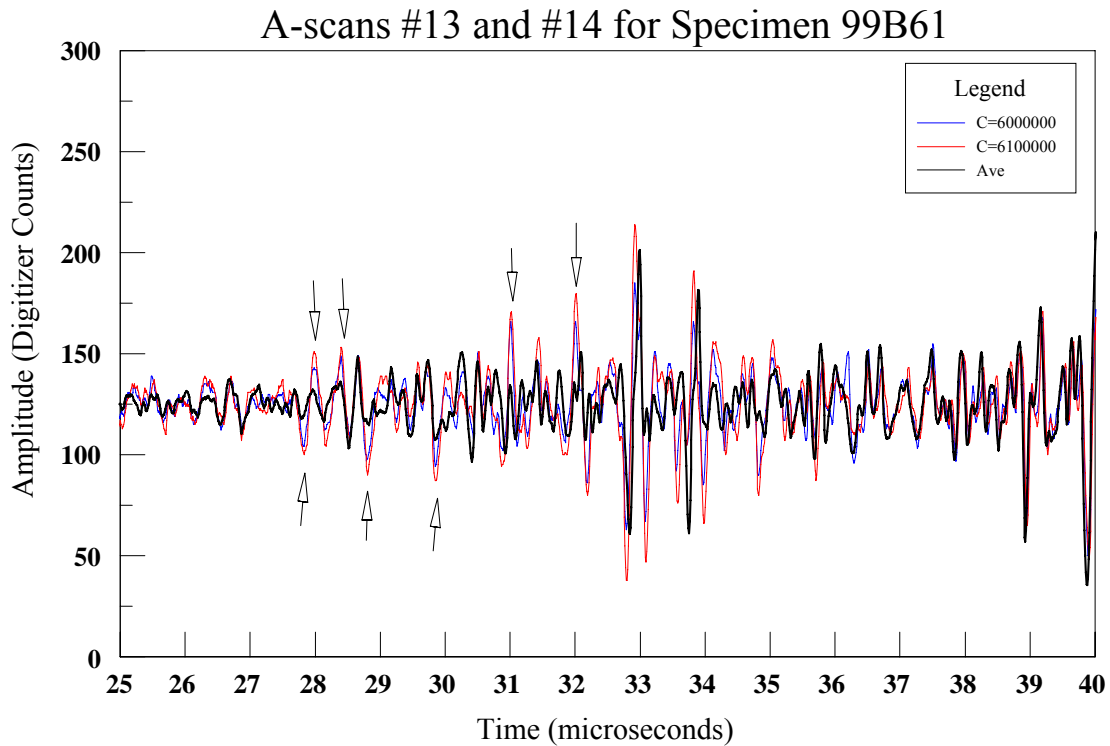


Figure 4. Ultrasonic waveforms from later in 99B61 compared with the average shown in figure 3. Changes indicative of fretting nucleated cracks are indicated with arrows.

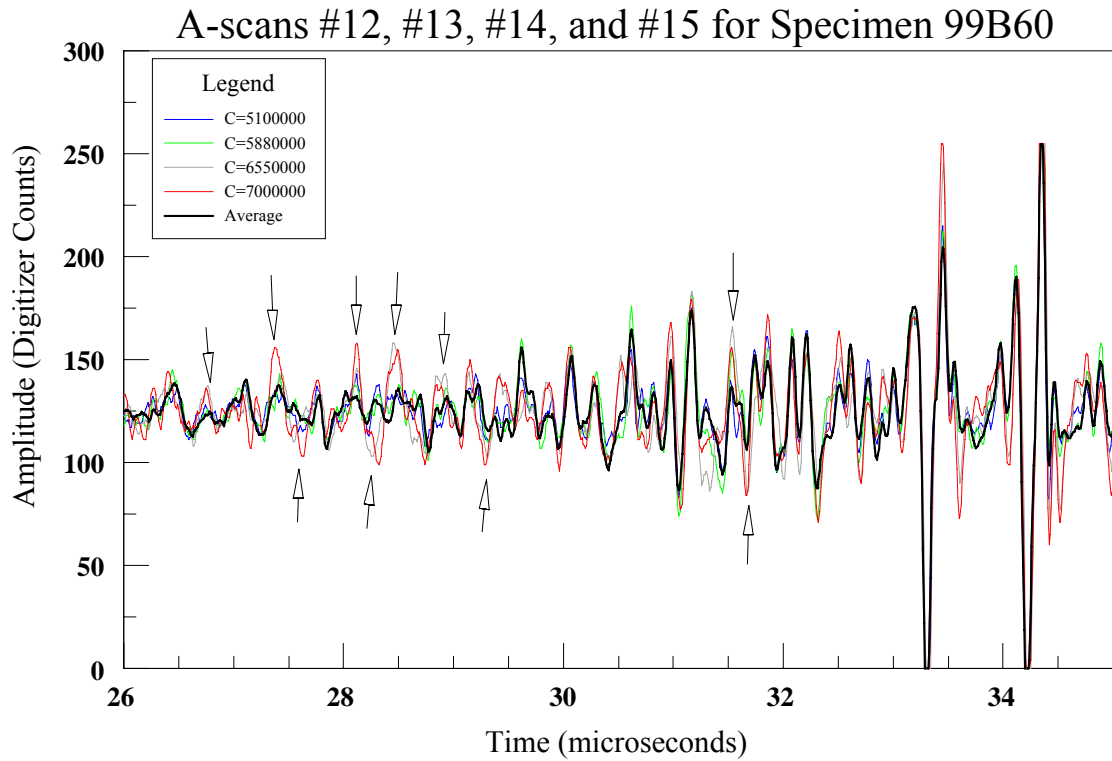


Figure 6. Ultrasonic waveforms from the latter part of experiment 99B60 compared with an average of waveforms obtained early in the experiment. Changes indicative of fretting nucleated cracks are indicated with arrows. (Note: time scale is expanded to enhance waveform details.)

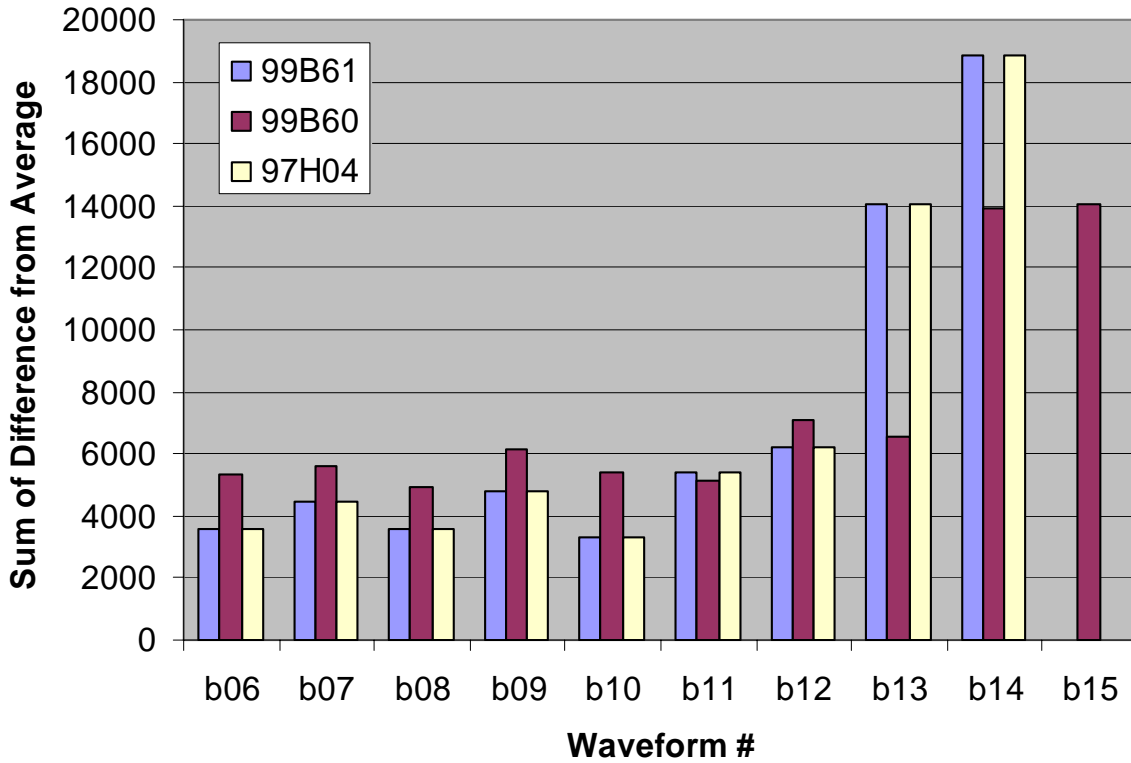


Figure 8. Sum of difference between average waveform and individual waveforms for time = 25 to 40 μ s (high clamping stress tests).

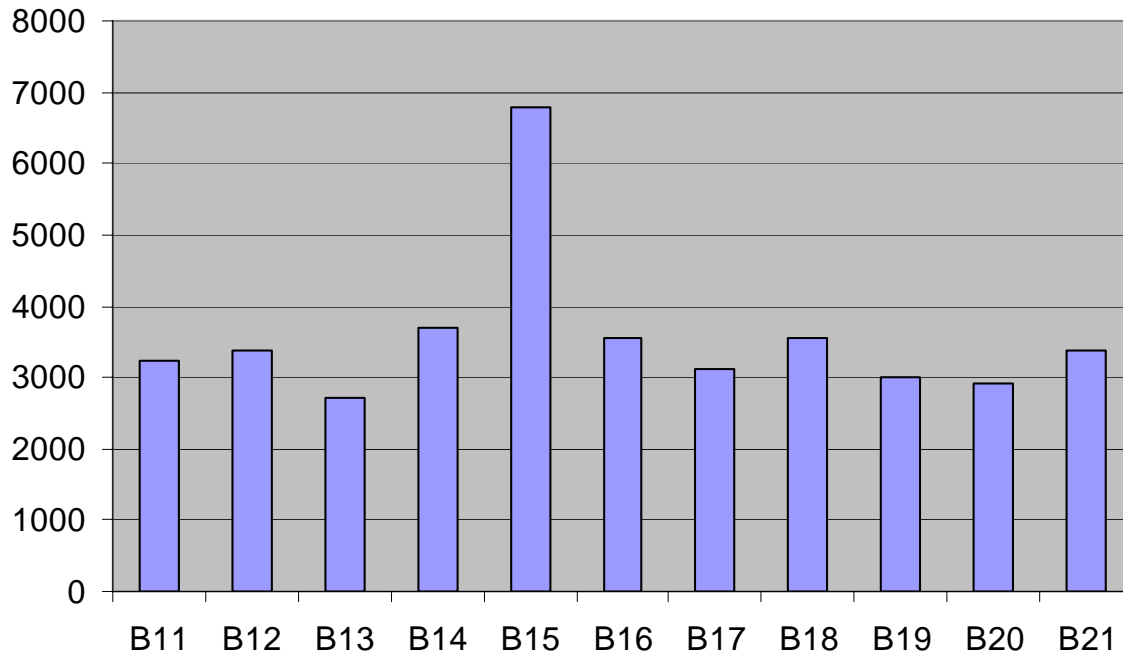


Figure 9. Sum of difference between average waveform and individual waveforms for time = 25 to 40 μ s for 99B57, on which no cracks were identified after 10.9 million cycles (low clamping stress).

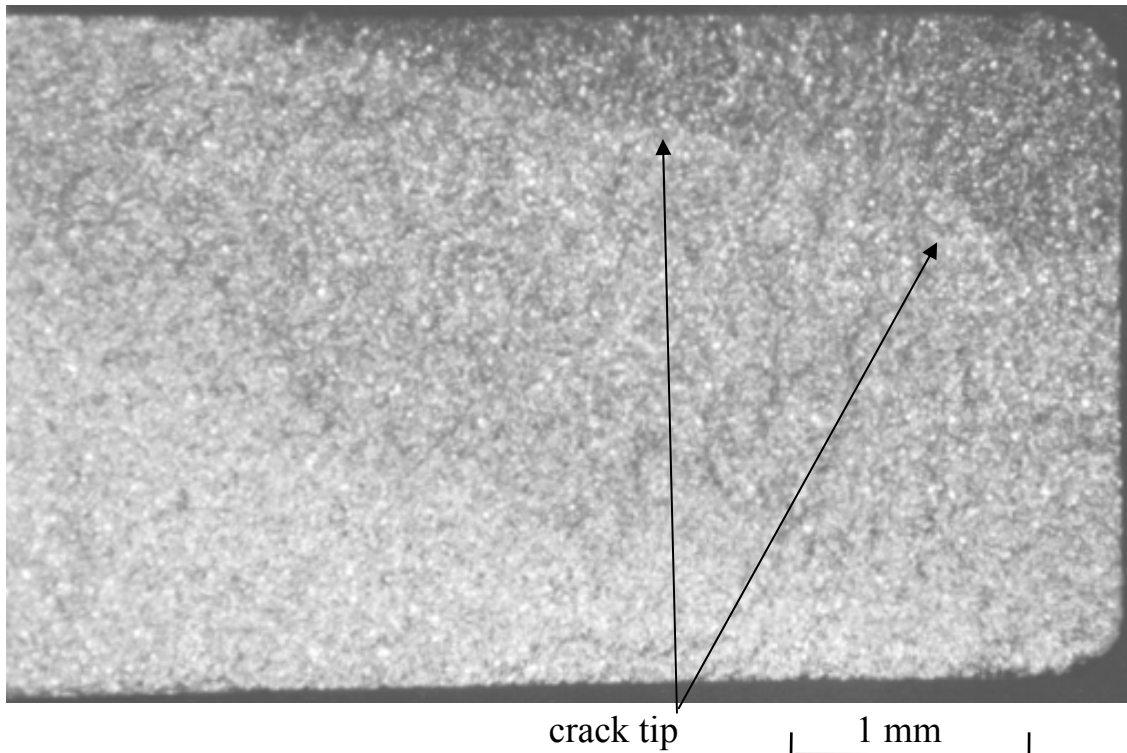


Figure 7. Fracture surface of specimen with successful shear wave crack detection ($N = 7,020,000$ cycles – 99B60). Arrows indicate crack tip position at time of crack detection.

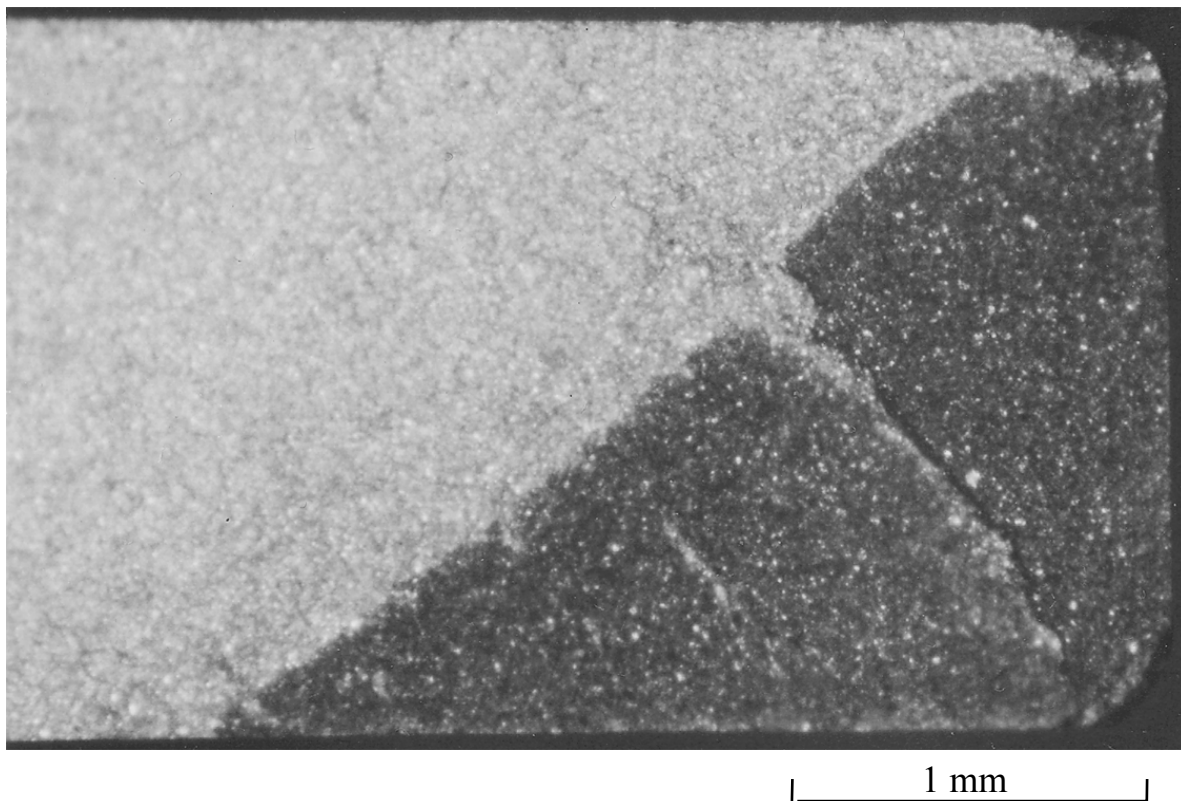


Figure 5. Fracture surface of specimen with successful shear wave crack detection ($N = 6,125,000$ cycles – 99B61).

Off-axis Creep Behavior of Oxide/Oxide Nextel™720/AS-0

Dennis J. Buchanan*, Reji John and Larry P. Zawada

Materials and Manufacturing Directorate, Air Force Research Laboratory (AFRL/MLLMN),
Wright-Patterson Air Force Base, OH 45433-7817

*University of Dayton Research Institute, Dayton, OH 45469-0128

Abstract

Oxide/Oxide Ceramic Matrix Composites (CMC) are currently being demonstrated in high-temperature aerospace applications where their beneficial resistance to oxidation are critical to a successful design. Many applications are engine components that are axisymmetric in shape and subjected to axisymmetric thermal and mechanical loadings. However, traditional woven CMC materials used in these components are typically made from 0°/90° fiber architectures. In many cases the highest stresses are not always coincident with the orientation of the reinforcing fibers. Therefore, these components may experience stress states that approach the off-axis tensile and creep strengths. The oxide/oxide CMC investigated in this study was Nextel™720/AS. Nextel™720/AS is composed of an Alumina-Silica matrix reinforced with an eight-harness satin weave (8HSW) of Nextel™720 fibers. Tensile and creeps tests at 1100°C on ±45° Nextel™720/AS were performed to characterize the off-axis material behavior. The ±45° orientation had approximately two thirds the ultimate tensile strength of the 0°/90° orientation. However, the tensile toughness of the ±45° orientation was higher than the 0°/90° orientation by a factor of 2X. The creep rupture strength at 100 hrs for the ±45° orientation was approximately one third that of the 0°/90° orientation.

Introduction

Damage tolerant ceramic matrix composites (CMC) that exhibit relatively little degradation in mechanical properties at elevated temperature are being evaluated for high temperature aerospace applications. Advances in CMC processing have enabled lower-cost fabrication techniques that provide the capability to produce complex shaped components. Many of these complex shapes have fillets, corners, holes and other structural features that develop multi-axial stress states under thermal and mechanical loading.

Typically, characterization of a new material tends to focus on properties aligned with the direction of the reinforcing fiber such as strength, moduli and ductility. This may satisfy a particular design or material requirement but it is not sufficient, in general, for a structural material. Although a good understanding of the stresses and temperatures in the engine may be known it is often difficult to precisely know the extremes and the perturbations that a particular component or feature may experience. Therefore it is desirable to have a structural material that is damage tolerance, stable at elevated temperatures and quasi-isotropic with respect to pertinent material properties.

Often the engine applications require that material properties be maintained at elevated temperature and under combustion environment conditions for long durations. Oxide/oxide CMC have an inherent resistance to oxidation and therefore exhibit little or no degradation in

mechanical properties at expected service temperatures. Several authors [1-7] have reported that oxide/oxide CMC exhibit excellent tensile, fatigue and creep properties at room and elevated temperatures. Monotonic tensile behavior at room and elevated temperature (1100°C) on $\pm 45^\circ$ Nextel™720/AS [10,11] have shown that the ultimate strength and strain to failure are a function of test temperature. This is in contrast to the $0^\circ/90^\circ$ behavior. This investigation focuses on the sustained load (creep) behavior of the $\pm 45^\circ$ orientation at 1100°C. This paper will characterize the differences in the material behavior of the $0^\circ/90^\circ$ and $\pm 45^\circ$ orientations. Further, based on these experimental results, we conclude that a Cartesian fiber architecture is not well suited for the design of axisymmetric components.

Material

The Nextel™720/AS oxide/oxide CMC was manufactured by ATK COI Ceramics, Inc, of San Diego, CA. The Nextel™720 fibers, which are produced by the 3M Company of St. Paul, MN [15], are $\approx 12 \mu\text{m}$ in diameter and have a nominal composition of 85% Al_2O_3 and 15% SiO_2 . The addition of Mullite ($3 \text{Al}_2\text{O}_3 \cdot 2 \text{SiO}_2$) to the Nextel™720 fiber provides improved creep resistance over the Nextel™610 fiber that is a single-phase composition of $\alpha\text{-Al}_2\text{O}_3$. The Nextel™720 fibers have an elastic modulus of 260 GPa and a tensile strength of 2100 MPa for a 25 mm gage length [Wilson]. Approximately 400 fibers were bundled together into a tow. Multiple tows are woven together into a balanced eight-harness-satin weave (8HSW) cloth.

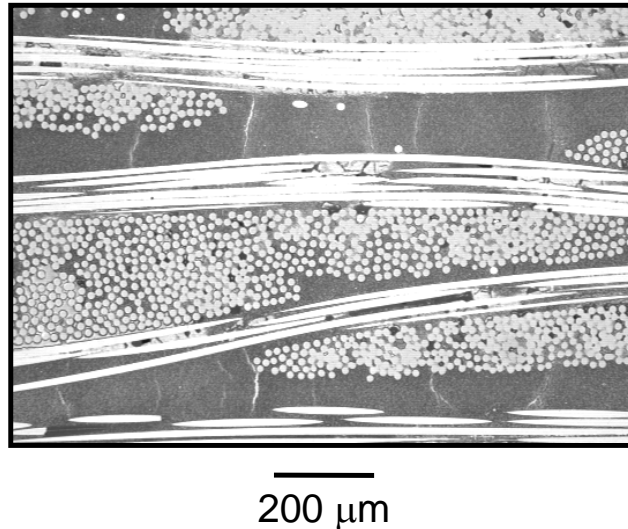


Figure 1. Microstructure of ($0^\circ/90^\circ$) 8HSW Nextel™720/AS-0 microstructure highlighting the matrix cracks due to processing.

The porous alumina-silica (AS) matrix forms a weak bond to the fibers without an engineered interphase. This provides the CMC with damage tolerance behavior. The weak bond between the fiber and matrix allows relative movement between the fiber and matrix that enables crack deflection and hence toughness. The porous matrix contains approximately 87 wt% single crystal submicron alumina suspended in 13 wt% silica. The nested plies were warp aligned during lay-

up with alternating plies rotated about the warp direction so that fill fibers were matched with fill fibers and warp fibers matched with warp fibers. This lay-up technique matches fabric texture on neighboring plies and minimizes panel warpage. The 2D Nextel™720 fabric was prepregged with alumina powder and a silica forming polymer before stacking. The laminate was then warm molded to produce the green state ceramic tile. Sintering the green tile in air at 1000°C removed the organic binders and produced a porous alumina-silica matrix. Section samples of panels used in this study showed that the fiber volume fraction range was 42 - 50%. Figure 1 shows microcracks distributed throughout the matrix rich regions of the composite as a result of panel shrinkage that occurred during processing. The panels used for this study were 300 mm x 300 mm and composed of 12 plies.

Experimental Procedure

The dogbone specimen geometry, shown in Fig. 2, was used for unnotched tensile and creep tests in this study. The overall dimensions of the specimens were, thickness \approx 2.5 mm, length \approx 150 mm and grip width \approx 16 mm. The gage section width of 10 mm provides a 37.5% reduction in area to promote gage section failure. This width is also greater than the repeating cell size of the 8HSW cloth, which is approximately 9 mm. The 18 mm uniform width gage length permits placement of a conventional elevated-temperature extensometer and provides a volume averaging of fiber and matrix properties that will be used for development of a macroscopic material model. All specimen dimensions were measured prior to testing.

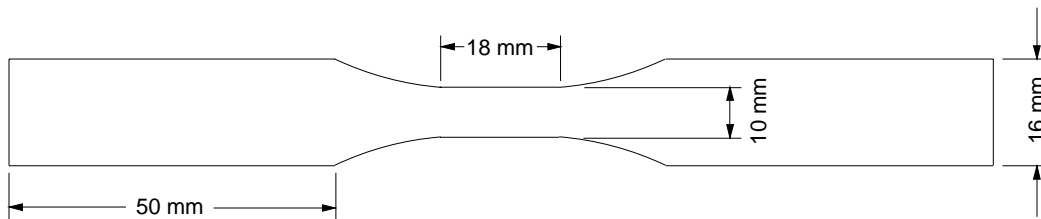


Figure 2. Dogbone specimen test geometry.

The specimen ends were tabbed with fiberglass tabs to provide a flat uniform surface for the grip surfaces and to minimize the possibility of grip failure. The specimens were mounted in a precisely aligned, rigid grip system that minimized specimen bending and rotation [16]. A clamshell furnace with silicon-carbide heating elements and four-zone control were used for the elevated temperature tests. Four S-type thermocouples were used to measure and control the temperature in the gage section of the test specimen. Two thermocouples were on the top surface and two were on the bottom surface. Four-zone temperature control provided the capability of reducing the temperature gradients through the specimen thickness and along the loading axis of the specimen. Thermal profile maps on the specimen showed that the specimen was uniformly heated, \pm 5°C, over the entire gage section of the specimen.

All tensile tests were performed in displacement control at a rate of 0.05 mm/s generated by a 16-bit D/A function generator. The tensile test duration was typically less than 10 seconds and therefore time dependent creep behavior did not contribute to the measured deformation. Creep

tests were performed in load control at a loading rate of 20 MPa/s up to the hold stress for all creep tests. Extensometry measurements were made on both sides of the test specimen to verify that specimen bending and hence stress gradients induced in the gage section were negligible. Also, prior to starting any test, room temperature and elevated temperature modulus measurements were made by loading the sample in stress control to approximately 20 MPa, well below the proportional limit. Tensile and creep tests were started only if the room temperature and elevated temperature modulus values agreed with expected results and the modulus values from the two opposing extensometers were in agreement with each other, hence no bending in gage section. Applied load, temperature and extensometry data were collected during all tensile and creep tests. All tests were conducted in laboratory air using a computer controlled servo-hydraulic horizontal test system [16, 17].

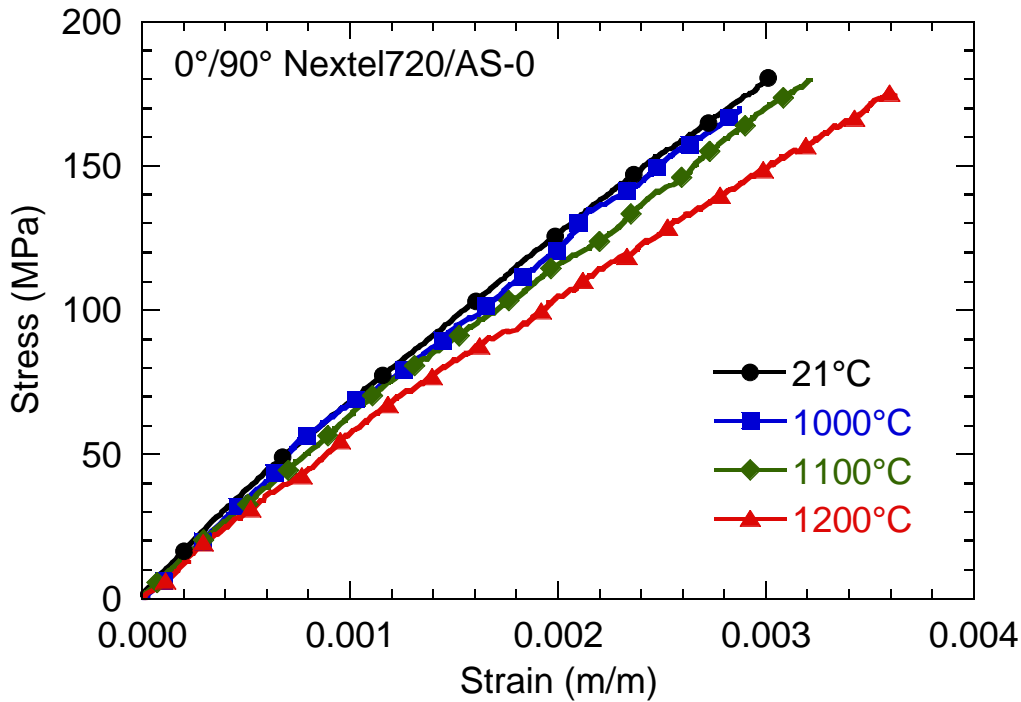


Figure 3. Stress versus strain for Nextel™720/AS-0 oriented in the 0°/90° RT-1200°C.

Experimental Results – Monotonic Tensile Behavior

Monotonic tensile tests at room and elevated temperatures on specimens with woven fiber aligned in 0°/90° orientation are shown in Fig. 3. At temperatures up to and including 1100°C there was no degradation in the elastic modulus or ultimate strength of the 0°/90° orientation. These modulus values are consistent with data reported on similar oxide/oxide systems [Zok, 1, 11, 14] at room and elevated temperature. The 1200°C tensile data show that ultimate strength was preserved while initial elastic modulus slightly decreased and total deformation to failure increased. Tensile strengths of Nextel™720 fibers measured by Wilson et al. [8] show approximately a 20% decrease in strength at 1200°C compared to 1100°C and below. The

decrease in fiber strength and retained composite tensile strength at 1200°C suggests the existence of residual stresses between the fiber and the matrix. This is also supported by the decrease in elastic modulus of the composite which is unaffected by the presence of the residual stress between the fibers and the matrix. Zawada et al. [18] reported tensile residual stresses in the fibers on the order of 200 MPa for a similar oxide/oxide CMC at room temperature.

Monotonic tensile tests were also conducted on dogbone specimens with woven fibers mats aligned in $\pm 45^\circ$ orientations. The axial stress versus axial strain response for the $\pm 45^\circ$ orientation at room and elevated temperatures are shown in Fig. 4. Tensile data collect by Antti & Lara-Curzio [10] on the same oxide/oxide CMC are shown for room temperature and 1000°C. In contrast to the $0^\circ/90^\circ$ data from Fig. 3, the $\pm 45^\circ$ orientation exhibited a strong temperature dependent deformation response. Although the initial elastic modulus remained the same for this range of temperatures, the ultimate tensile strength and strain to failure increased with increasing temperature.

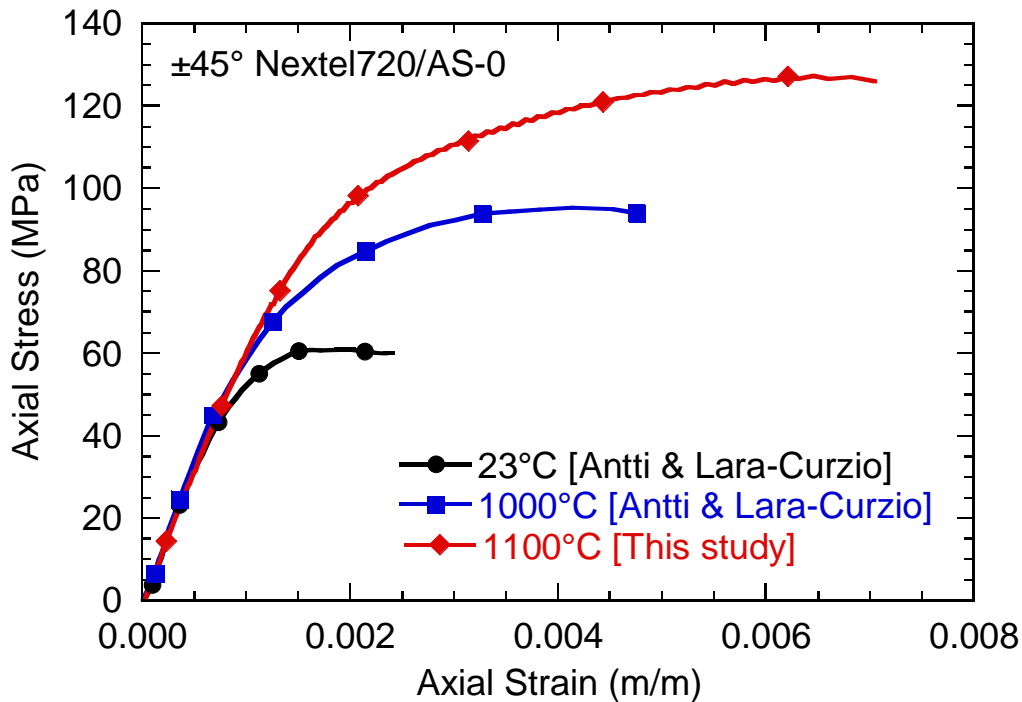


Figure 4. Stress versus strain for Nextel™720/AS-0 oriented in the $\pm 45^\circ$ RT-1100°C.

The increase in ultimate tensile strength with temperature also supports the argument for the existence of residual stresses being present in the CMC at room temperature. Since the fibers in the $\pm 45^\circ$ orientation are not continuous from one end of the specimen to the other, composite deformation behavior was not limited by the ductility of the Nextel720 fibers. However, at room temperature failure strain of the $\pm 45^\circ$ orientation was slightly less than that of the $0^\circ/90^\circ$ orientation as observed in Fig. 3. This also supports the argument that residual stresses between the fiber and matrix exist in the CMC at room temperature. As the temperature increased above room temperature the residual stress in the fiber decreased as a result of the CTE mismatch between the fiber and the matrix. The reduced residual stress at elevated temperature enables the fibers to carry higher loads and therefore enables the composite to achieve an increase in failure

strength in the $\pm 45^\circ$ orientation. The reduced residual stresses at elevated temperature also provide relative slip between fiber and matrix. This allows for greater failure strain to be achieved at elevated temperature.

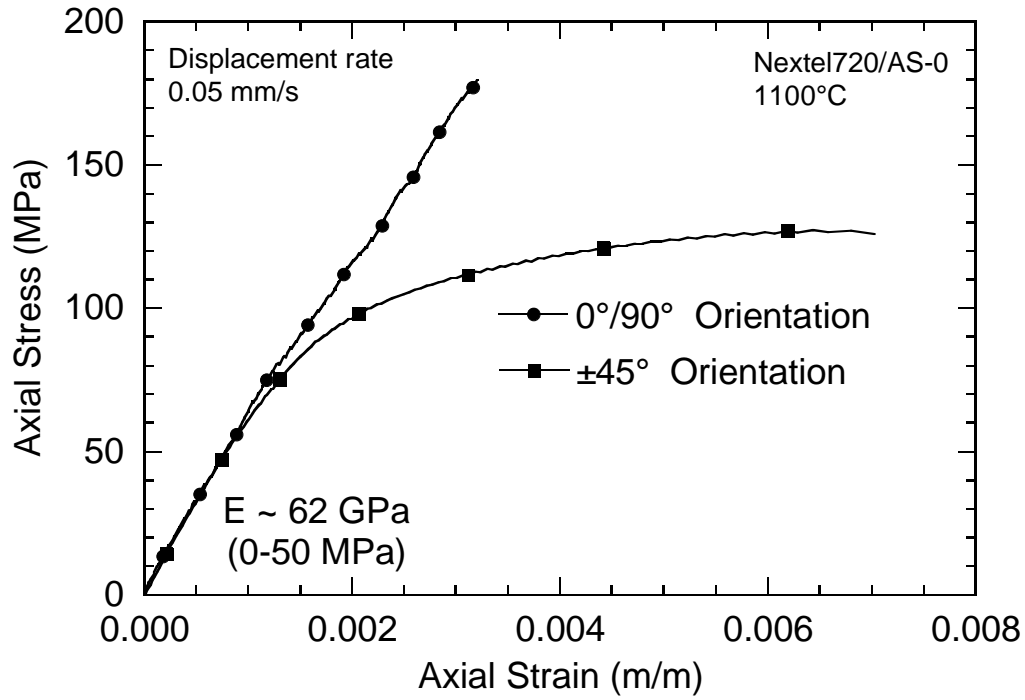


Figure 5. Stress versus strain for Nextel™720/AS-0 oriented in the $0^\circ/90^\circ$ and $\pm 45^\circ$ at 1100°C .

The axial stress versus axial strain for the $0^\circ/90^\circ$ and $\pm 45^\circ$ orientations at 1100°C are shown together in Fig. 5. As expected, the $0^\circ/90^\circ$ orientation, which has continuously reinforced fibers between the grips has a higher ultimate tensile strength and lower strain to failure than the $\pm 45^\circ$ orientation. The mechanical behavior of the CMC is driven primarily by the high strength, high modulus and low ductility fibers. However, the initial elastic modulus, measured up to 50 MPa, show that the two orientations have similar elastic moduli, approximately 62 GPa. This is in contrast to the modulus results reported by Levi et al. [6] on Nextel™610 oxide/oxide CMC where the elastic modulus was strongly orientation dependent. The difference between the different CMC is that the Nextel™610 fiber has a much higher modulus than the Nextel™720 fiber, 380 and 260 GPa, respectively. Zuiker [20] and Tandon et al. [19] have predicted oxide matrix modulus values of approximately 60 GPa and less. The higher modulus Nextel™610 fiber will produce a more pronounced orientation dependent elastic modulus in the CMC. When stresses are above ≈ 50 MPa, the $\pm 45^\circ$ orientation exhibits a large decrease in stiffness while the $0^\circ/90^\circ$ orientation maintains initial stiffness to failure.

The fracture surfaces for the $0^\circ/90^\circ$ and $\pm 45^\circ$ tensile specimens at 1100°C are shown in Figs. 6a and 6b, respectively. The fracture surface profiles for the two orientations are coincident with the fiber weave orientations. For the $0^\circ/90^\circ$ orientation the fracture plane is normal to the applied

load which is typical for a brittle material. In contrast, the $\pm 45^\circ$ orientation fracture plane was at a 45° angle with respect to the applied load which is typical for a ductile material when the ultimate shear stress is reached. Since the reinforcing fibers in the gage section of the $\pm 45^\circ$ sample are not attached to either gripped end of the specimen it is relatively easy for the fiber tows to slip past one another at the 45° angle and fail the matrix. The area under the entire engineering stress-strain curve of Fig. 5, the tensile toughness, is a measure of the damage accumulation in the material. For the two stress-strain curves in Fig. 5 the tensile toughness of the $0^\circ/90^\circ$ and $\pm 45^\circ$ orientations were 0.30 and 0.71 MJ/m^3 , respectively. Although the $\pm 45^\circ$ orientation had a lower ultimate strength than the $0^\circ/90^\circ$ orientation it required more than 2X inelastic work to fail the specimen. This was primarily due to the fact that the damage occurred over a larger volume of material.

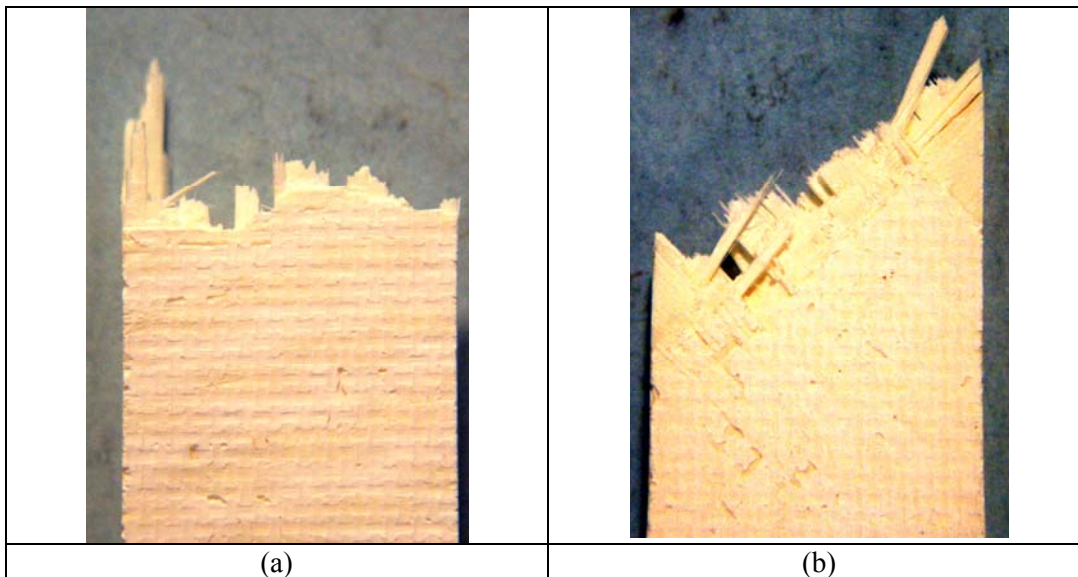


Figure 6. Fracture surface of tensile tested Nextel™720/AS-0 at 1100°C (a) $0^\circ/90^\circ$, (b) $\pm 45^\circ$.

Experimental Results – Sustained Load (Creep) Behavior

Based on the monotonic tensile results of the previous section shown in Figs. 3-6, and the authors previous work [1, 12, 13] on oxide/oxide CMC, the sustained load (creep) behavior of the material in the $\pm 45^\circ$ orientation was investigated. The total strain versus time of the $\pm 45^\circ$ Nextel720/AS material subjected to sustained load (creep) at 1100°C are shown for four stress levels (50, 60, 70, 80 MPa) in Fig. 7. The deformation behavior show a strong influence of applied stress on the time to failure. The total strain to failure does not appear to be well correlated with the applied stress. These results are for a stress range that corresponds to 40 - 65% of the $\pm 45^\circ$ ultimate tensile strength. Previous creep studies [1] on the $0^\circ/90^\circ$ orientation exhibited very little creep deformation at 1100°C . Only when the applied stress was at greater than 80% of the $0^\circ/90^\circ$ ultimate tensile strength was there any measurable time dependent deformation. Clearly the time dependent behavior of the $\pm 45^\circ$ orientation was activated at lower stresses and probably lower temperatures than the $0^\circ/90^\circ$ orientation.

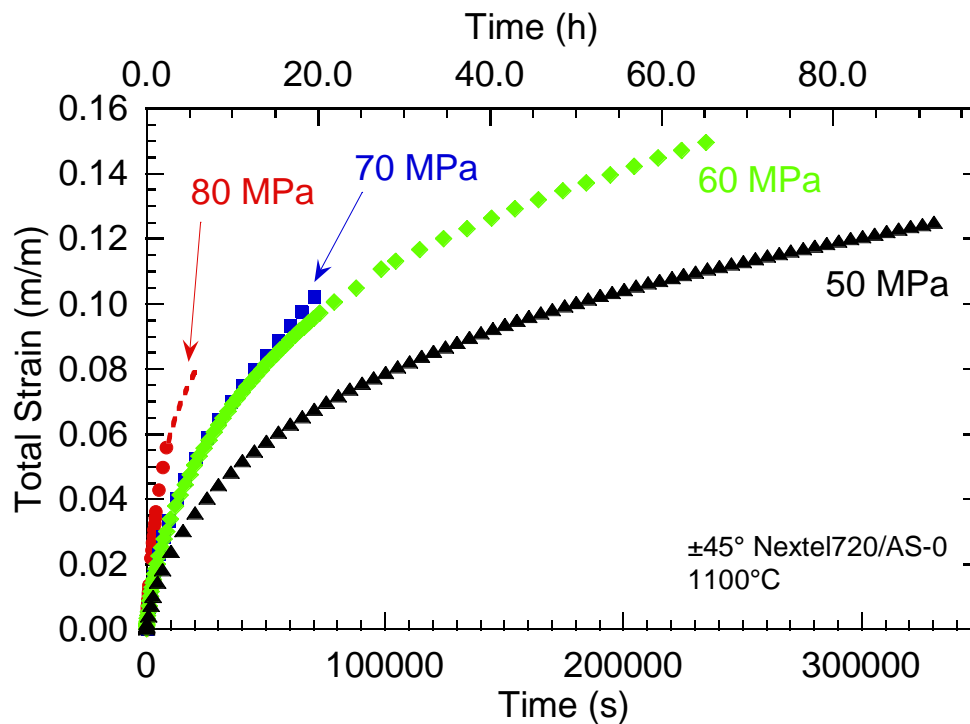


Figure 7. Total strain versus time for $\pm 45^\circ$ Nextel720/AS-0 at 1100°C .

The NextelTM720 fibers exhibit stable deformation behavior up to approximately 1100°C for extended periods of time [8]. Carelli et al. [21] have demonstrated that the usage temperature of this CMC is ultimately limited by the alumina-silica matrix properties. Long-term exposure at 1100°C sinters the matrix and causes the matrix to bond to the fibers. This negates the intentional weak interface that was designed for damage tolerance by deflecting matrix cracks. Hence, the maximum usage temperature for long-term exposure of this composite material is probably less than 1100°C .

Naturally the question arises as to what temperature will the matrix and hence the $\pm 45^\circ$ orientation exhibit stable deformation behavior? Consequently, the creep behavior as a function of temperature was investigated by conducting sustained load (creep) tests at constant stress with stepped increases in temperature. A minimum starting temperature of 900°C was chosen with temperature steps of 50°C taken up to a maximum of 1100°C . The temperature was held constant until it appeared that the material had achieved a stable constant creep rate. After achieving a constant creep rate the temperature was rapidly increased to the next higher temperature and the process repeated until failure or the test temperature of 1100°C was reached. Figure 8 shows the total strain versus time for a stepped temperature test that was conducted at an applied stress of 70 MPa. The total strain to failure from the stepped temperature test at 70 MPa was similar to the 70 MPa isothermal test in Fig.7. The time to rupture was clearly affected by the prior lower temperature strain history. The extended time at lower temperature contributed to the overall increase in rupture time and approximately 40% of the total deformation. As expected, the slopes of the strain versus time curves, i.e., the creep rate, increased with each increase in temperature.

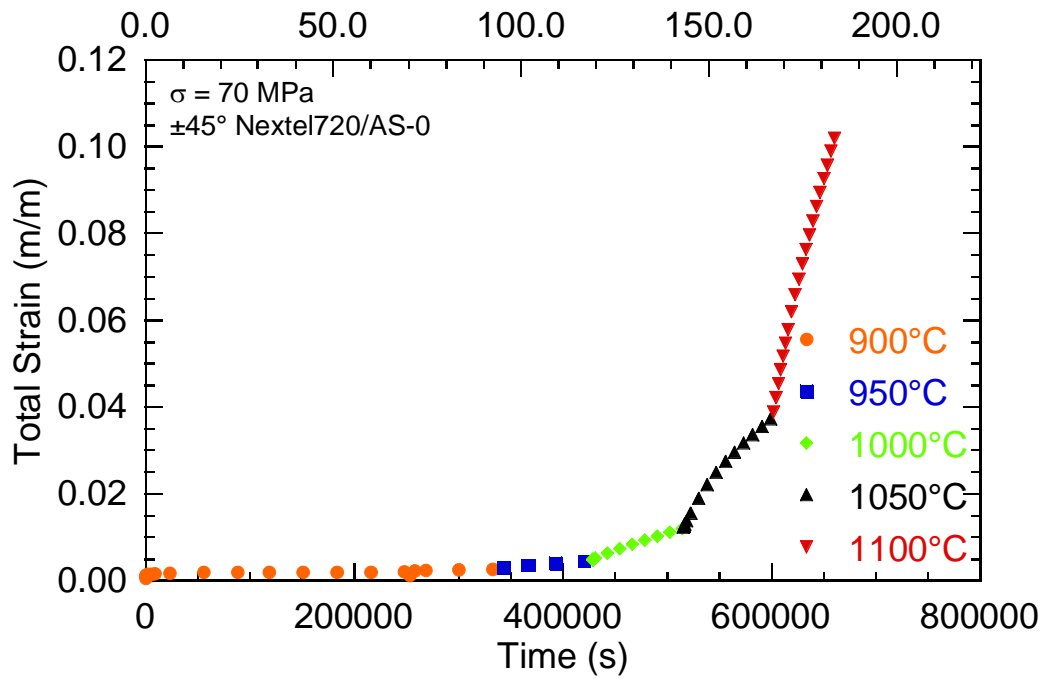


Figure 8. Total strain versus time for $\pm 45^\circ$ Nextel720/AS-0 for stepped temperature (900-1100°C) creep test at 70MPa.

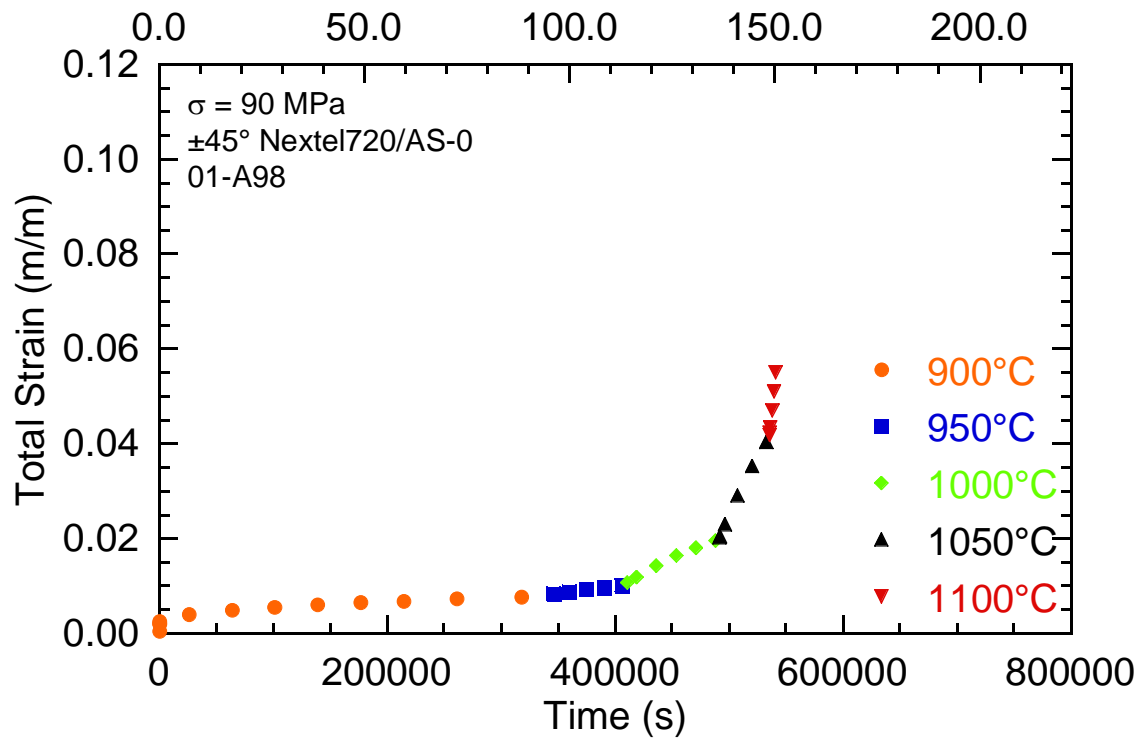


Figure 9. Total strain versus time for $\pm 45^\circ$ Nextel720/AS-0 for stepped temperature (900-1100°C) creep test at 90MPa.

The 900 and 950°C portions have a relatively flat deformation response whereas the 1050 and 1100°C portions show strain rates comparable to the creep rates at 60 and 70MPa at 1100°C of Fig. 6. A similar stepped temperature test was conducted at 90MPa with the results shown in Fig. 9. As expected the time to failure for the 90MPa test was shorter than the 70MPa test for similar time and temperature exposures. Also consistent with the higher stress, shorter life test was a decrease in total strain to failure, approximately 40% compared to the 70MPa stepped temperature test. At every temperature the steady state strain rate was higher for the 90MPa test than the 70MPa test.

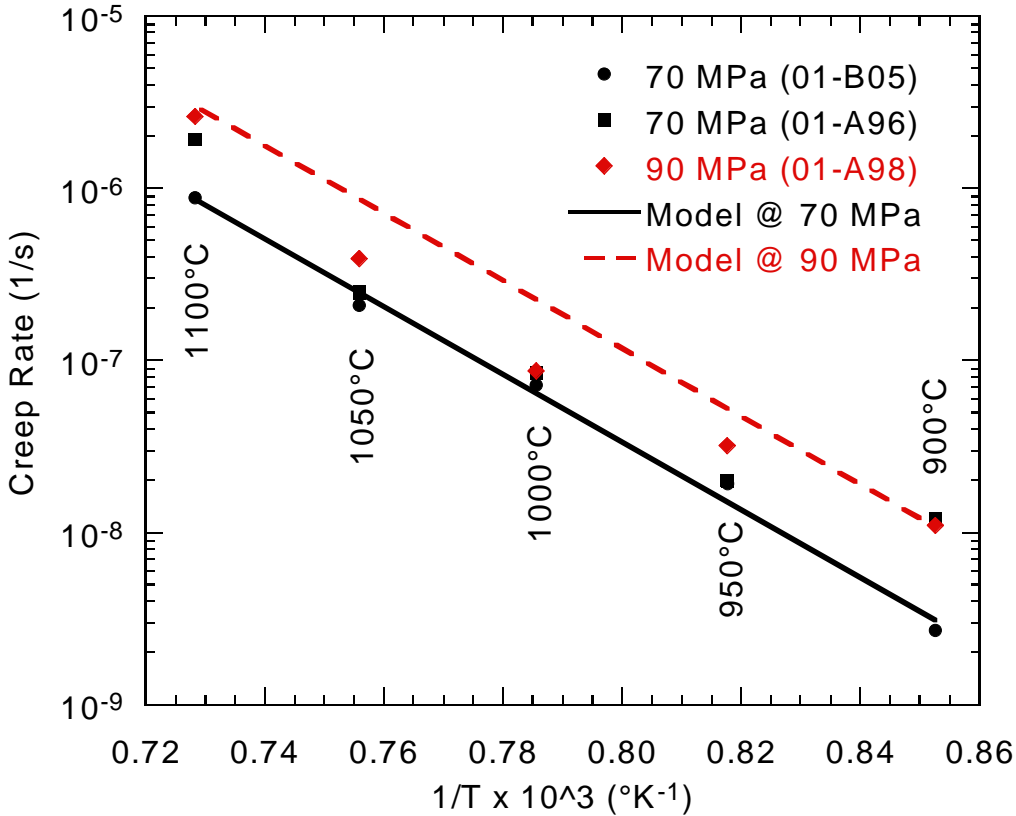


Figure 10. Strain rate versus $1/T$ for creep of $\pm 45^\circ$ Nextel720/AS-0.

Strain rate dependence on stress is often described by a simple power law model. The strain rate dependence on temperature is best modeled using the Arrhenius rate equation. Combining the power law equation and Arrhenius equation results in the creep rate equation shown below where (A , n , ΔH_A) are material parameters, (R) is the universal gas constant, (T) is temperature in Kelvin and (σ) is stress in MPa.

$$\dot{\epsilon}_c = \frac{A}{kT} \sigma^n \exp\left(\frac{-\Delta H_A}{RT}\right)$$

The activation energy (ΔH_A) was determined from the change in stable strain rates for a stepped increase in temperature as shown by the equation below. Parameters A and n were determined from a least squares fit to the experimentally measured creep strain rate data.

$$\Delta H_A = \frac{R \ln \left(\frac{\dot{\epsilon}_1}{\dot{\epsilon}_2} \right)}{\frac{1}{T_2} - \frac{1}{T_1}}$$

Using these equations a comparison between the measured steady state creep rates and model are shown in Table 1. Figure 10 shows the minimum creep rate versus the inverse of the test temperature for all the $\pm 45^\circ$ orientation stepped temperature creep data. The symbols are the measured creep rates and the lines are the calculated creep rates based on the power law model. The linearity of the data suggests that a single mechanism is responsible for the deformation behavior for this range of temperatures and stresses.

Table 1. Comparison of Creep Rate and Model of $\pm 45^\circ$ Nextel720/AS-0 at 900 - 1100°C.

Stress (MPa)	70				
Temperature (°C)	900	950	1000	1050	1100
Temperature (°K)	1173	1223	1273	1323	1373
Measured Creep Rate (m/m/s)	2.70E-09	1.92E-08	7.23E-08	2.07E-07	8.83E-07
	1.20E-08	2.00E-08	8.50E-08	2.50E-07	2.09E-06
Modeled Creep Rate (m/m/s)	3.10E-09	1.51E-08	6.48E-08	2.49E-07	8.65E-07

Stress (MPa)	90				
Temperature (°C)	900	950	1000	1050	1100
Temperature (°K)	1173	1223	1273	1323	1373
Measured Creep Rate (m/m/s)	1.09E-08	3.16E-08	8.67E-08	3.86E-07	2.61E-06
Modeled Creep Rate (m/m/s)	1.08E-08	5.26E-08	2.26E-07	8.68E-07	3.02E-06

Figure 11 is a comparison of strain rate versus applied stress for the $0^\circ/90^\circ$ and $\pm 45^\circ$ orientations. Creep results from Zawada et al. [1] and Lara-Curzio and More [14] on $0^\circ/90^\circ$ NextelTM720/AS-0 at 1100°C and 1200°C, respectively, show a much lower strain rate compared to the $\pm 45^\circ$ data at 1100°C. For a creep stress, $\sigma \approx 90$ MPa, the $0^\circ/90^\circ$ strain rate is over 5000X slower than $\pm 45^\circ$ at 1100°C. Even at 1200°C, which is above the usage temperature for the NextelTM720/AS-0, the $0^\circ/90^\circ$ strain rate is two orders of magnitude lower than the $\pm 45^\circ$ orientation at 1100°C. The strain rate is clearly dependent on the orientation of the reinforcing fibers.

Figure 12 shows the applied net section stress versus creep rupture time for unnotched and double edge notch $0^\circ/90^\circ$ and unnotched $\pm 45^\circ$ Nextel720/AS-0 at 1100°C. Previous studies [13,14] on the $0^\circ/90^\circ$ orientation have shown the double notched geometry shows a reduction in creep rupture life when compared to the unnotched geometry. The unnotched $\pm 45^\circ$ orientation data in Fig. 12 show a further

reduction in creep rupture life from the notched $0^\circ/90^\circ$ data. To achieve a rupture life of 100 hours at 1100°C the net section stress for the unnotched $0^\circ/90^\circ$, notched $0^\circ/90^\circ$ and unnotched $\pm 45^\circ$ should be less than 155, 95 and 55 MPa, respectively. Clearly, this knockdown in the rupture life of the $\pm 45^\circ$ compared to the $0^\circ/90^\circ$ orientation at 1100°C limits the applicability of this material for components subjected to multiaxial states of stress.

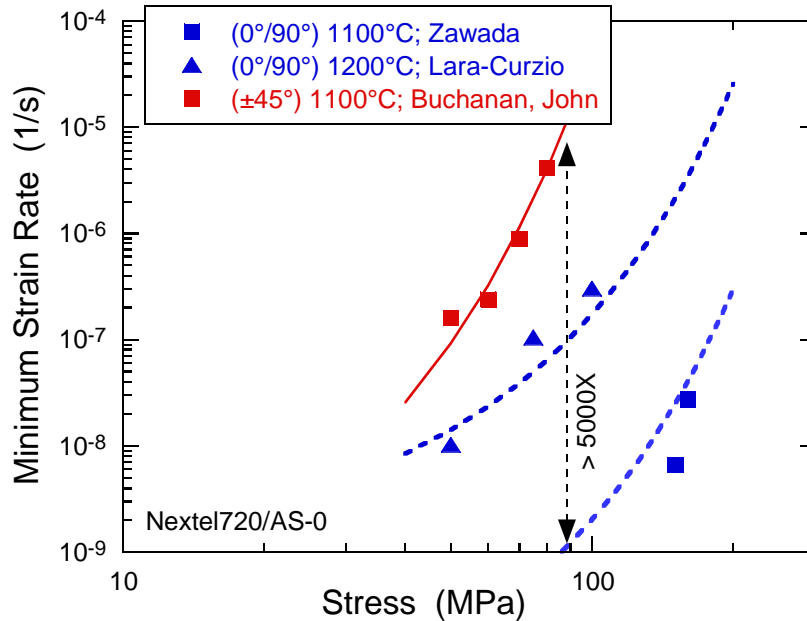


Figure 11. Minimum strain rate versus stress for creep of $0^\circ/90^\circ$ and $\pm 45^\circ$ Nextel720/AS-0.

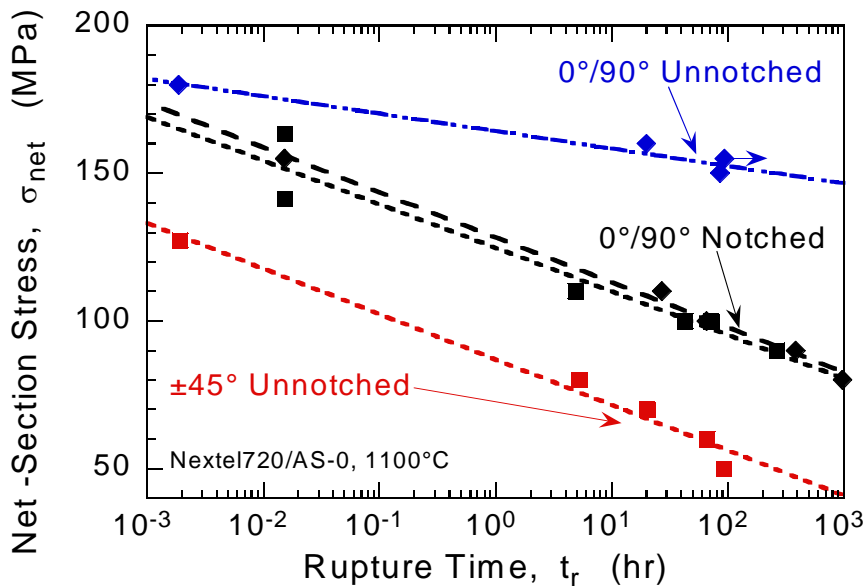


Figure 12. Creep rupture behavior of $0^\circ/90^\circ$ and $\pm 45^\circ$ Nextel720/AS-0 at 1100°C .

It is also clear that a Cartesian fiber architecture such as a $0^\circ/90^\circ$ is not well suited for construction of axisymmetric components where the principal stress axes are not coincident with the orientation of the

reinforcing fiber weave. The fracture surfaces for the $0^\circ/90^\circ$ and $\pm 45^\circ$ creep tests at 1100°C with similar rupture lives, approximately 20 hours, are shown in Figs. 13a and 13b, respectively. The stress levels were 160 and 70 MPa, for the $0^\circ/90^\circ$ and $\pm 45^\circ$ orientations, respectively. The fracture surface profiles for both orientations are normal to the applied stress. For the $0^\circ/90^\circ$ orientation the fracture plane for the monotonic tensile test and the creep test were the same. In contrast, the $\pm 45^\circ$ orientation fracture plane was at a 45° angle for the monotonic tensile test while the creep test fracture plane was normal to the applied stress. It has been shown that long term thermal exposure sinters the matrix and the fiber and matrix become bonded together. It appears that the bonding of the matrix to the fiber has changed the fracture behavior of the $\pm 45^\circ$ orientation. The volume of damaged material in the creep test is less than was observed in the monotonic tensile test. Therefore long term exposure to elevated temperature reduces the damage tolerance of the $\pm 45^\circ$ orientation.

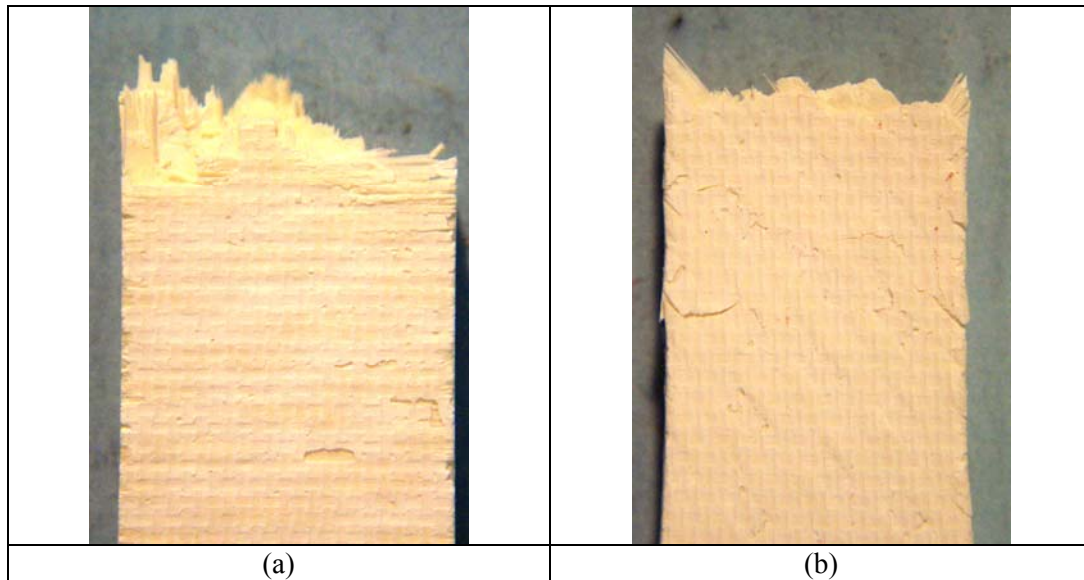


Figure 13. Fracture surface of sustained load (creep) tested Nextel™720/AS-0 at 1100°C (a) $0^\circ/90^\circ$, $\sigma = 160\text{ MPa}$, $Tr = 20\text{ hrs}$, (b) $\pm 45^\circ$, $\sigma = 70\text{ MPa}$, $Tr = 20\text{ hrs}$.

Summary

The creep rupture behavior of oxide/oxide Nextel™720/AS CMC with 2D fiber mat orientations $0^\circ/90^\circ$ and $\pm 45^\circ$ were investigated. Tensile tests on $0^\circ/90^\circ$ and $\pm 45^\circ$ orientations at 1100°C show similar elastic moduli, however they have different ultimate strengths and failure strains. Results of creep tests show that the secondary creep strain rate of the $\pm 45^\circ$ orientation can be as high as 5000X that of the $0^\circ/90^\circ$ orientation at 1100°C . The ratio of the creep rupture strength at 100 hours and 1100°C of $\pm 45^\circ$ to $0^\circ/90^\circ$ is 0.3 for unnotched specimens. Stable creep behavior and possibly the maximum usage temperature of the $\pm 45^\circ$ orientation is less than 1050°C .

Acknowledgments

This research was conducted at the Materials and Manufacturing Directorate, Air Force Research Laboratory (AFRL/MLLN), Wright-Patterson Air Force Base, OH 45433-7817. Mr. Dennis Buchanan was supported under an onsite contract number F33615-98-C-5214. The authors gratefully acknowledge the assistance of Mrs. Patricia Youngerman and Mr. Mark Ruddell in conducting the experiments.

References

- [1] Zawada, L. P. and Lee, S. S., "Mechanical Behavior of CMCs For Flaps and Seals," Proceedings of Advanced Research Projects Agency (ARPA) Advanced Ceramics Technology Insertion Program (ACTIP) Annual Review, W.S. Coblenz, Ed., Washington, DC, August 1995.
- [2] Zawada, L. P. and Lee, S. S., "Evaluation of Four CMCs For Aerospace Turbine Engine Divergent Flaps and Seals," Ceramic Engineering and Science Proceedings, Vol. 16, No. 4, 1995, pp. 337-339.
- [3] Mouchon, E. and Colombari, Ph., "Oxide Ceramic Matrix/Oxide Fiber Woven Fabric Composites Exhibiting Dissipative Fracture Behavior," Composites, Vol. 26, 1995, pp. 175-182.
- [4] Lange, F. F., Tu, W. C., and Evans, A. G., "Processing of Damage-Tolerant, Oxidation- Resistant Ceramic Matrix Composites by a Precursor Infiltration and Pyrolysis Method," Materials Science and Engineering, Vol. A195, 1995, pp. 145-150.
- [5] Zawada, L. P., Hay, R. S., Lee, S. S., and Staehler, J., "Characterization and High Temperature Mechanical Behavior of an Oxide/Oxide Composite," Journal of the American Ceramic Society, Submitted for publication, January 2001.
- [6] Levi, C. G., Yang, J. Y., Dalglish, B. J., Zok, F. W. and Evans, A. G., "Processing and Performance of an All-Oxide Ceramic Composite," Journal of the American Ceramic Society, Vol. 81, No. 8, 1998, pp. 2077-2086.
- [7] Heathcote, J. A., Gong, X. -Y., Yang, J., Ramamurty, U., and Zok, F. W., "In-Plane Mechanical Properties of an All-Oxide Ceramic Composite," Journal of the American Ceramic Society, Vol. 82, No. 10, 1999, pp. 2721-2730.
- [8] Wilson, D. M., Lieder, S. L., and Lueneburg, D.C., "Microstructure and High Temperature Properties of Nextel 720 Fibers," Ceramic Engineering Science Proceedings, Vol. 16, No. 5, 1995, pp. 1005-1014.
- [9] Yun, H. M. and DiCarlo, J. A., "Time/Temperature Dependent Tensile Strength of SiC and Al₂O₃-Based Fibers," NASA Technical Memorandum 107370, NASA Glenn Research Center, Cleveland, OH, USA, 1996.
- [10] Antti, M-L., and Lara-Curzio, E., "Effect of Notches, Specimen Size, and Fiber Orientation on the Monotonic Tensile Behavior of Composites at Ambient and Elevated Temperatures," The 25th Annual Cocoa Beach Conference and Exposition, The American Ceramic Society, January 2001.
- [11] Krumb, V. A., "Notched fracture behavior of an oxide/oxide ceramic matrix composite," Ph.D. Thesis, University of Dayton, Department of Materials Engineering, 1999.
- [12] Buchanan, D. J., John, R., and Zawada, L. P., "Notched Fracture Behavior of Oxide/Oxide Nextel 720/AS Composite," The 24th Annual Cocoa Beach Conference and Exposition, The American Ceramic Society, January 2000.
- [13] John, R., Buchanan, D. J. and Zawada, L. P., "Creep Deformation and Rupture Behavior of a Notched Oxide/Oxide Nextel 720/AS Composite," The 24th Annual Cocoa Beach Conference and Exposition, The American Ceramic Society, January 2000.
- [14] Lara-Curzio, E., and More, K. L., "Stress-Rupture Behavior of Nextel 720/AS fiber-reinforced Aluminosilicate CFCCs at 1200°C," The 24th Annual Cocoa Beach Conference and Exposition, The American Ceramic Society, January 2000.

- [15] 3M Company Product Data Sheet, 3M Ceramic Fiber Products, 3M Center-Building 207-1W-11, St. Paul, MN 55144-1000.
- [16] Hartman, G. A., and Buchanan, D. J., "Methodologies for thermal and mechanical testing of TMC materials," Characterization of fibre reinforced titanium matrix composites. 77th Meeting of the AGARD Structures and Materials Panel, AGARD Report 796, Bordeaux, France, 27-28 September 1993.
- [17] Hartman, G. A., Ashbaugh, N. E., and Buchanan, D. J., "A sampling of mechanical test automation methodologies used in a basic research laboratory," Automation in fatigue and fracture: testing and analysis, ASTM STP 1231, Ed. C. Amzallag, American Society for Testing and Materials, Philadelphia, PA, 1994, pp. 36-50.
- [18] Zawada, L. P., Hay, R. S., Lee, S. S., and Staehler, J., "Characterization and High-Temperature Mechanical Behavior of an Oxide/Oxide Composite," Journal of the American Ceramic Society, Vol 86, No. 6, 2003, pp. 981-990.
- [19] Tandon, G. P., Buchanan, D. J., Pagano, N. J., and John, R., "Effective Elastic and Thermal Properties of a Damaged Woven Oxide/Oxide Composite," submitted to Journal of the American Ceramic Society.
- [20] Zuiker, J. R., "A Model for the Creep Response of Oxide-Oxide Ceramic Matrix Composites," Thermal and Mechanical Test Methods and Behavior of Continuous-Fiber Ceramic Composites, ASTM STP 1309, Ed. Michael G. Jenkins et al., American Society for Testing and Materials, Philadelphia, PA, 1997, pp. 250-263.
- [21] Carelli, E. A. V., Fujita, H., Yang, J. Y., and Zok, F. W., "Effects of Thermal Aging on the Mechanical Properties of a Porous-Matrix Ceramic Composite," Journal of the American Ceramic Society, Vol 85, No. 3, March 2002, pp. 595-602.

LIST OF SYMBOLS, ABBREVIATIONS, AND ACRONYMS

<u>ABBREVIATION</u>	<u>DEFINITION</u>
3-D	three-dimensional
3-DFE	three-dimensional FE
8HSW	eight harness satin weave
γ -TiAl	Gamma titanium aluminide
A/D	analog-to-digital
AFIT	Air Force Institute of Technology
BMF	brittle micro fracture
BRS	bulk residual stress
CAD	computer-aided design
CD	compact disc
CDF	cumulative distribution function
CFCDE	crack front cyclic diffusion embrittlement
CMC	ceramic matrix composites
CMM	coordinate measuring machine
CVI	chemical vapor infiltrated/infiltration
DCPD	Direct current potential difference
DEN(T)	double edge notch tension specimen
DVD	digital video disc
EDM	electric discharge machining
EOC	edge of contact
ERLE	engine rotor life extension
FCG	fatigue crack growth
FE	finite element
FEA	finite element analysis
FEM	finite element model
FIB	focused ion beams
FOD	foreign object damage
GE	General Electric
GEAE	GE Aircraft Engines
GMT	general monotonic testing
GPM	gallons per minute
HCF	high cycle fatigue
HIP	hot isostatically pressed
IDDS	IR Damage Detection System
IHPTET	Integrated High Performance Turbine Engine Technology
LCF	low cycle fatigue
MI	melt infiltrated/infiltration
MLLM	Metals Branch
MLLMN	Behavior/Life Prediction Section
MLOC	Government Computer Support
NDE	nondestructive evaluation
NDI	nondestructive inspection
NMI	nonmetallic inclusion
NMOD	notch mouth opening displacement
NTED	National Turbine Engine Durability
OIM	orientation imaging microscopy

PIN	physically isolated networks
PM	powder metal
P/M	powder metallurgy
PSI	pressure per square inch
PST	polysynthetically twinned
RG	Research Group
SAE	Society of Automotive Engineers
SBIR	Small Business Innovation Research
SEM	scanning electron microscopy
Ti	titanium
TEM	transmission electron microscopy
UDRI	University of Dayton Research Institute
USAF	United States Air Force
WPAFB	Wright-Patterson Air Force Base
XRD	X-ray diffraction